Gondwana Research 128 (2024) 14–54

Contents lists available at ScienceDirect

Gondwana Research

journal homepage: www.elsevier.com/locate/gr

GR Focus Review

Interactions of magmas and highly reduced fluids during intraplate volcanism, Mt Carmel, Israel: Implications for mantle redox states and global carbon cycles

W.L. Griffin [a,*], L. Bindi [b], F. Cámara [c], C. Ma [d], S.E.M. Gain [a,e], M. Saunders [f], O. Alard [a,g], J.-X. Huang [a], J. Shaw [f], C. Meredith [h], V. Toledo [i], S.Y. O'Reilly [a]

[a] ARC Centre of Excellence for Core to Crust Fluid Systems (CCFS) and GEMOC, School of Natural Sciences, Macquarie University, NSW 2109, Australia
[b] Dipartimento di Scienze della Terra, Università di Firenze, I-50121 Florence, Italy
[c] Dipartimento di Scienze della Terra 'A. Desio', Università degli Studi di Milano, I-20133 Milano, Italy
[d] Division of Geological and Planetary Sciences, California Institute of Technology, Pasadena, CA 91125, USA
[e] Fortescue Metals Group, Perth, WA 6004, Australia
[f] Centre for Microscopy, Characterisation and Analysis, The University of Western Australia, WA 6009, Australia
[g] Research School of Earth Sciences, Australian National University, Canberra, A.C.T 2600, Australia
[h] Dept. of Materials Science and Engineering, The Pennsylvania State University, University Park, PA 16802, USA
[i] Shefa Gems, Netanyzna 4210602, Israel

ARTICLE INFO

Article history:
Received 1 July 2023
Revised 27 October 2023
Accepted 28 October 2023
Available online 10 November 2023
Handling Editor: M. Santosh

Keywords:
Methane-magma reaction
Super-reduced minerals
Oxygen fugacity
Mantle-crust carbon transfer
Mt Carmel
Ophiolites

ABSTRACT

Oxygen fugacity (fO_2) controls the speciation of COH fluids in Earth's mantle; a major question is whether the sublithospheric mantle is metal-saturated, maintaining fO_2 near the Iron-Wüstite (IW) buffer reaction. If so, then COH fluids from this source will be dominated by $CH_4 + H_2$, rather than the more oxidized CO_2-H_2O fluids commonly considered in petrological studies. A key to this question is found in rare but widespread examples of natural mineral assemblages that require unusually low fO_2. We summarize an investigation of super-reduced mineral assemblages in corundum xenocrysts from Late Cretaceous alkali-basalt volcanoes on Mt Carmel, northern Israel and related Plio-Pleistocene alluvial deposits. *P-T* estimates indicate that the corundum xenocrysts crystallized in the uppermost mantle. The well-documented geological controls on the origin of these deposits, and radiometric dating of the super-reduced phases, ensure the "naturalness" of the controversial assemblages and make these mineral parageneses a benchmark for evaluation of related occurrences worldwide.

The tuffs contain a "basalt-megacryst" mineral suite (zircon, sapphire, ilmenite, spinel). The megacryst chemistry and the geochronology of the zircons indicate that the megacrysts crystallized from broadly syenitic melts that differentiated at subcrustal levels (*P ca* 1 GPa) within a thick gabbroic underplate built up from Permian through Pliocene time and perhaps into the Pleistocene. Reaction of mantle-derived CH_4-H_2 fluids with these syenitic melts led to the separation of immiscible Fe^0 and Fe-Ti oxide melts near fO_2 = IW. Trace-element distributions suggest the syenitic melts then separated into immiscible Si-Al-Na-K-rich and FeO-rich oxide melts; the latter were enriched in HFSE, REE, P and Zr as in other natural and synthetic examples of melt-melt immiscibility.

In a model magma chamber the FeO-rich melts would sink, leaving the Si-Al-Na-K melts in an upper zone, both still fluxed by CH_4-H_2 fluids. At fO_2 of ΔIW-6 to -7 the removal of immiscible Fe-Ti-Si-C silicide melts from the FeO-rich melt would leave a desilicated Ca-Al-Si oxide melt that crystallized high-Ti corundum hibonite cumulates with inclusions requiring fO_2 from ΔIW + 2 to ΔIW-9, while the less-reduced conjugate silicate melts in the upper levels crystallized low-Ti corundum. Aggregates of skeletal, strongly Ti-zoned corundum crystals. reflect rapid crystallization from very reduced melt-fluid mixtures, probably in fluid-escape channels. Explosive eruptions sampled individual magma chambers at different depths and with different initial compositions, fluid mixtures and fluid dynamics to produce Mt Carmel's mineralogical diversity.

A review of similar occurrences worldwide suggests that the Mt Carmel assemblages reflect a fundamental process – the rise of CH_4-H_2 fluids into the upper mantle -- that accompanies mantle-derived magmatism in many tectonic settings. The interaction of these fluids with lithospheric mantle rocks

* Corresponding author.
E-mail addresses: bill.griffin@mq.edu.au (W.L. Griffin), vered.toledo1@gmail.com (V. Toledo).

https://doi.org/10.1016/j.gr.2023.10.013

and melts can lead to extreme fractionation via the separation of immiscible Fe-Ti-Si-C melts and residual desilicated melts. The oxidation of CH_4-H_2 fluids in the lithospheric mantle may be the ultimate source of metasomatic fluids dominated by CO_2 + H_2O, and of many diamonds. More attention should be paid to the role of methane and other reduced fluids in mantle petrology, and their relevance to metasomatic processes and global carbon cycles.

Contents

1. Introduction

Ongoing controversy surrounds the nature and origin of carbon-bearing fluids in Earth's upper mantle. For example: are diamonds formed in the cratonic lithospheric mantle by oxidation of reduced fluids, by reduction of oxidized fluids, or both? How are metasomatic fluids generated in the lithospheric mantle? What is the redox state of the sublithospheric mantle? Are fluid fluxes analyzed at the surface representative of mantle outgassing? Such uncertainty ultimately affects our ideas about the nature of metasomatic processes and melting relationships in the mantle, and the processes that drive volcanism and move elements of economic interest from mantle to crust. Some of the controversy reflects the difficulty of interpreting mineralogical and isotopic signatures in terms of their causative agents, and the ambiguity of most types of evidence.

Experimentally calibrated oxythermobarometers indicate that the upper mantle and its shallow melting products such as basalts are relatively oxidized, providing little evidence for reducing fluids in the upper mantle. On the other hand, several studies have concluded that much of the sublithospheric mantle is saturated in metal (Fe,Ni) alloys, in which case coexisting COH fluids would be dominated by methane and hydrogen (e.g. Frost et al., 2004; Rohrbach et al., 2007; Frost and McCammon, 2008; Stagno et al., 2013). The discovery that large sublithospheric diamonds grew in metal-saturated environments and contain inclusions of CH_4 + H_2 (Smith et al., 2016, 2018) also argues for the presence of reducing fluids at least in the deeper parts of the upper mantle. If such fluids do rise from the asthenosphere, evidence of their passage might not be expected to survive in a more oxidized upper mantle. However, peridotites in depleted cratonic lithosphere, at least, have little buffering capacity (Luth and Stachel, 2014) and many deep-seated xenoliths record oxygen fugacities (fO_2) approaching the iron-wüstite (IW) buffer (Woodland and Koch, 2003; Yaxley et al., 2012). Furthermore, the presence of phases such as moissanite (SiC) as inclusions in diamonds and in mineral separates from kimberlites and other deep-seated rocks (Shiryaev et al., 2011; Griffin et al., 2018c) requires that domains with $fO_2 \ll$ IW must exist at least locally within the upper mantle.

This review first explores the composition and formation of xenolithic material from nine small late-Cretaceous volcanoes, erupted over *ca* 10–15 Ma and an area of *ca* 150 km^2 on Mt Carmel, northern Israel (Fig. 1), and from related alluvial deposits in the adjacent Yizre'el valley (Supplementary Material, Fig. S-1). These were targeted by a successful 14-year exploration program by Shefa Yamim Ltd (now Shefa Gems Ltd), aimed at the discovery of placer gem deposits in the Plio-Pleistocene sediments of the proto-Kishon River, which ran along the northern escarpment of Mt Carmel. Extensive heavy-mineral sampling of modern drainages and weathering profiles was used to identify possible primary sources. More than 1400 individual samples from the volcanic centres, the Plio-Pleistocene placers and modern drainages, ranging from a few kg to > 600 tonnes, were processed (Supplementary Material II; Hattingh, 2019).

Heavy-mineral concentrates from these samples typically contain a "basalt-megacryst" suite (zircon, sapphire, clinopyroxene, ilmenite, spinel), minerals derived from disaggregated mantle rocks (olivine, clinopyroxene, garnet, spinel) and a suite of minerals that require fO_2 ranging from ΔIW + 2 to ΔIW-9. Individual eruptions appear to have sampled a range of broadly similar magmatic systems at different stages of their parallel evolution. We propose that this evolution reflects interaction between highly reduced mantle-derived fluids and pre-existing melts in a differentiated basaltic underplate near the crust-mantle boundary.

We have previously documented several aspects of these remarkable deposits (Griffin et al., 2016a, 2018a-c, 2019a,b, 2020a,b, 2021a,b, 2022; Huang, 2020; Oliveira, 2021; Xiong et al., 2017). Here we synthesise that information and integrate it with a range of new observations and analytical data, including radiometric dating of SUR phases. Our aim is to provide a benchmark for understanding the sources and effects of highly reduced fluids in the mantle and lower crust.

This review of the mineralogy and geochemistry of the Mt Carmel assemblages allows the evaluation of other reported super-reduced (SUR) mineral associations, such as those from Tethyan ophiolites, kimberlitic rocks and the Kamchatka volcanoes, and supports their natural origins. We conclude that these processes are global in distribution; similar mineral assemblages are associated with cratonic roots, continental-collision zones and explosive volcanism in subduction zones and volcanic arcs, as well as in intraplate settings such as Mt Carmel. They imply an important role for mantle-derived methane-hydrogen fluids in magmatic and metasomatic processes in a variety of geological settings, with implications for global carbon cycles.

2. Geological setting and provenance of samples

The material described here is derived from intraplate Cretaceous volcanic centres and related Plio-Pleistocene alluvial (placer) deposits in the Mt Carmel-Yizre'el Valley area of Galilee, northern Israel (Fig. 1b; Supplementary Material, Fig. S-1). The geological setting and field appearance of the volcanics and the placer deposits have been described previously (Griffin et al., 2018a, 2021b) and are briefly summarized here.

The area lies within a complex system of minor rifts and other faults related to the nearby Africa-Arabia plate boundary, which later developed into the Dead Sea Transform, with *ca* 105km of left-lateral offset since movement began in Miocene time (Weinstein, 2012). The NW-SE Carmel Fault that bounds Mount Carmel on the east (Fig. 1b; Supplementary Material, Fig. S-1) is part of a belt of faulting 10–20 km wide that runs through the Yisre'el Valley and may extend NW across the continental margin (Segev and Rybakov, 2011). The unexposed basement rocks probably formed in Pan-African (Cadomian) time (>620 Ma; Stein and Goldstein, 1996).

This region experienced mafic and felsic volcanism during and after the Permo-Triassic Palmyra rifting related to the breakup of Gondwana and the opening of the Neo-Tethys ocean. An Early Jurassic (197–193 Ma) event erupted alkali-olivine basalts and pyroclastics with OIB-intraplate geochemical signatures (Dvorkin and Kohn, 1989). The sparse Early Cretaceous magmatism (C1, 137–139 Ma; Segev, 2005; references therein) comprises subalkaline to alkaline basalts, nephelinites and basanites with hotspot/mantle-plume geochemical and isotopic signatures (Garfunkel, 1989; Stein and Hofmann, 1992, 1994; Laws and Wilson, 1997). This magmatism continued until *ca* 125 Ma in Lebanon and possibly extended into northern Israel (C2; Segev, 2005).

The Late Cretaceous (98–94 Ma, Turonian-Cenomanian) volcanism in the Mount Carmel-Umm El Fahm area (Supplementary Material, Fig. S-1) has been described by Sass (1980). The dominant volcanic rocks are mafic to ultramafic pyroclastics with few lava flows, erupted in a shallow marine environment with carbonate sediments. The eruptive vents contain relatively fresh massive "black pyroclastics" (Sass, 1980; Griffin et al., 2021b); more strongly layered water-laid "variegated pyroclastics" of variable thickness are locally interbedded with carbonates, reflecting the construction and levelling of small seamounts (Sass, 1980). The few spatially associated basalt flows are porphyritic alkali-olivine

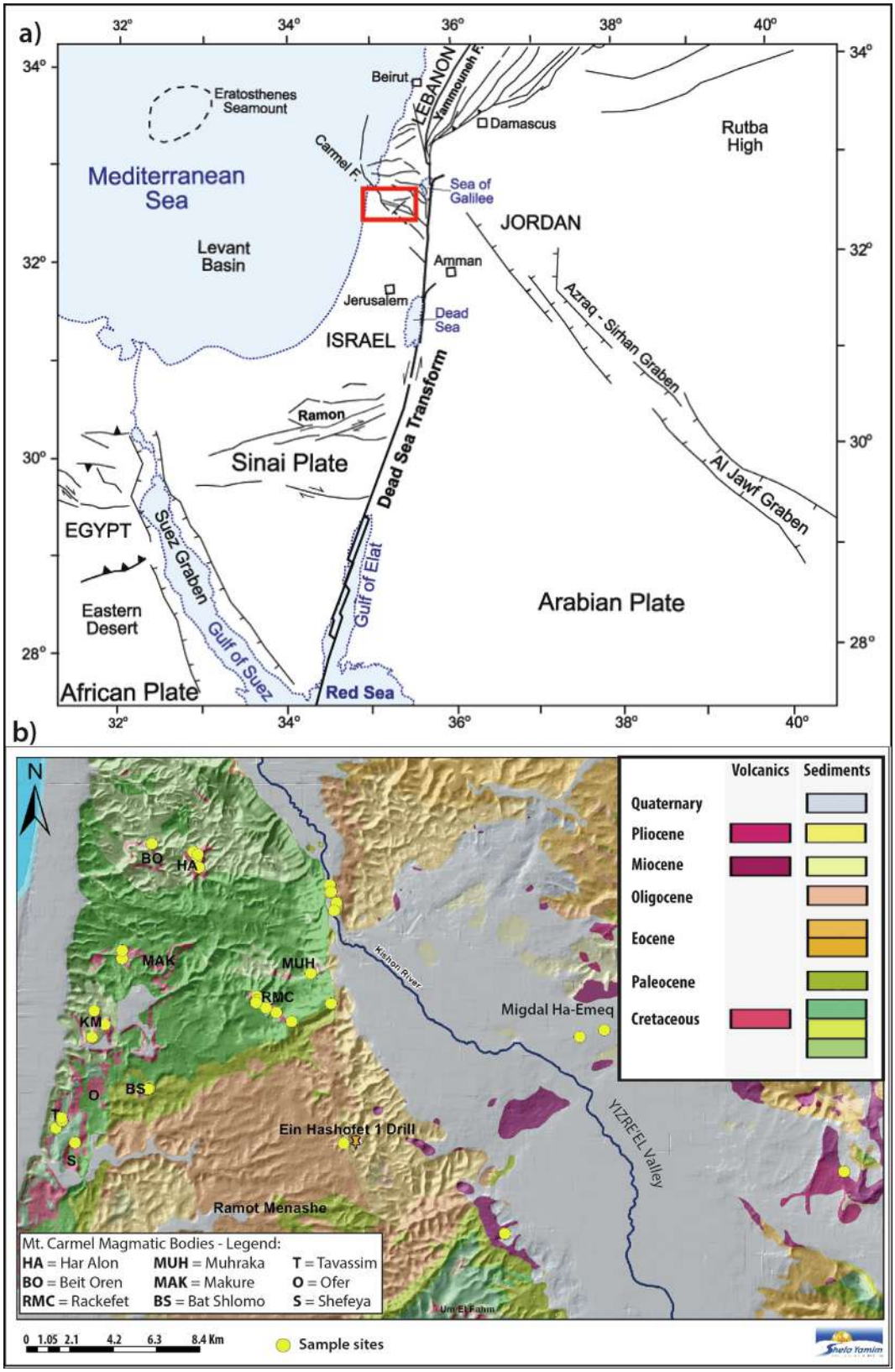

Fig. 1. a, Regional map showing location of major fault systems and the Mt Carmel area. Red frame marks location of b, a map of the Mt Carmel area showing simplified geology and locations of Cretaceous volcanic centres.

basalts with OIB-like trace-element signatures (Kaminchik et al., 2014); their relationship to the explosive magmatism is unclear (Sass, 1980). This volcanism continued to at least 76 Ma in areas NE of Mt Carmel (Ilani et al., 2005).

Following the Eocene recession of the Mediterranean Sea the area was eroded to a broad, flat coastal plain during the Oligocene. The present geomorphology (Fig. S-1) reflects the early Miocene to Pliocene development of a half-graben structure along the

N-dipping Carmel Fault, related to movement on the Dead Sea Transform (Kafri, 2002; Matmon et al., 2003). Prior to this, the Mt Carmel block was covered by late Eocene, Oligocene and probably early Miocene sediments and volcanic rocks; Miocene erosional surfaces are found on the Mt Carmel plateau (Steinberg et al., 2010). Isostatic uplift of the Mt Carmel block involved 400–500 m displacement and continues today (Matmon et al., 2003; Steinberg et al., 2010). The Lower Basalt (17–10 Ma; Rozenbaum et al., 2016) and the upper Miocene-Pliocene Cover Basalts (*ca* 5 Ma to < 3 Ma) include alkaline to tholeiitic flows and pyroclastic deposits with OIB geochemical signatures (Weinstein, 2000; Weinstein et al., 2006). The bulk of these basalts is buried beneath sediments, but large outcrops occur in the eastern and northern parts of the Yizre'el Valley (Fig. 1b; Supplementary Material, Fig. S-1).

The gem placers discussed here are concentrated in the "Kishon Gap" (Supplementary Material, Fig. S-1) where the valley narrows next to the Mt Carmel escarpment and the river entrains coarser material coming down in alluvial fans. Extensive drainage sampling and dating of "basaltic" zircons across the Yizre'el Valley indicates that both the Miocene-Pliocene volcanics and the Cretaceous volcanic centres have contributed heavy minerals to the alluvial deposits (Griffin et al., 2018). It is important to note that the placers sampled in this work do not come from the current bed of the Kishon River; they are paleoplacers developed at the base of Plio-Pleistocene terraces that now lie *ca* 10 m above the modern drainage. The paleoplacers occur in unlithified and uncemented coarse gravels that directly overlie bedrock at depths of 4–10 m and are overlain in turn by undisturbed finer-grained sediments (Griffin et al., 2021a).

Most of the known volcanic centers, as well as the paleoplacers, have been bulk-sampled (See Supplementary Material II) to determine their contents of gem minerals. These procedures capture heavy minerals down to 0.5 mm, a meticulous sampling regime rarely used in studies of basaltic complexes. This sampling has established that the Cretaceous volcanic centers, which lie 50–350 m above the Kishon river (Supplementary Material; Fig. S-1), collectively contain all of the minerals found in the alluvial deposits, in particular moissanite, ruby and corundum aggregates (Griffin et al., 2018a).

Corundum and moissanite (up to 4.1 mm), along with the peridotite-pyroxenite suite of minerals, also are found in surficial sediments and modern streams across the drainage basin of the Kishon River. This distribution in part reflects a shallow Miocene marine incursion that resulted in locally preserved carbonate-cemented, quartz-rich beach placers with garnet, diopside, spinel and moissanite (Roup et al., 2009; Supplementary Material, Fig. SD-3), which have been recycled into the Pliocene and Pleistocene-recent drainages. However, detailed surface sampling indicates that some of the placer materials, including sapphire, corundum aggregates and moissanite also may be derived directly from Tertiary volcanics exposed (presently or previously) in the area (Wald and Toledo, 2016). Geochronological data (see below) and our analysis of the distribution of different corundum parageneses (see below) strongly support this inference.

The occurrence of the corundum-moissanite SUR suite in the primary volcanic centres, in deeply buried Plio-Pleistocene placers and in lithified Miocene beach deposits (Griffin et al., 2019b, 2021b) and Mesozoic-Cenozoic U-Pb-Th ages on SUR minerals in the corundum aggregates (see below) demonstrate that the Mt Carmel SUR phases were formed and deposited long before humans walked on Earth. This clearly makes arguments for industrial contamination (Ballhaus, 2021; Galuskin and Galuskina, 2023a,b; Griffin, 2019a; Litasov et al., 2019b; Griffin et al., 2019b; Litasov et al., 2019a) untenable. Other evidence for the "naturalness" of the material studied here is summarized in Supplementary Material I.

3. Methods

Sampling and mineral separation procedures are described in detail by Griffin et al., (2021b) and in Supplementary Material II; they are based on diamond-industry practices designed to prevent anthropogenic contamination. Analytical procedures are described in Supplementary Material III. Methods used in this work include reflected- and transmitted-light petrography, electron probe microanalysis (EPMA) for analysis of major and minor elements and Th-U-Pb dating of minerals, scanning electron microscopy (SEM) with back-scattered electron (BSE) and cathodoluminescence (CL) imaging, energy-dispersive elemental analysis (EDS) and electron-backscatter diffraction (EBSD), Raman spectroscopy, transmission electron microscopy (TEM), electron energy-loss spectrometry (EELS), 3D X-ray μCT imaging, single-crystal X-ray diffraction, analysis of trapped gasses, analysis of oxygen and carbon isotopes by secondary-ion mass spectrometry (SIMS), and laser-ablation inductively-coupled plasma mass spectrometry (LA-ICPMS) for *in situ* analysis of trace-element abundances, $^{87}Sr/^{86}Sr$ in carbonates and U-Pb dating of carmeltazite.

4. Results

We describe in turn the geological and mineralogical features relevant to understanding the origin of the SUR mineral assemblages. To avoid repetition and simplify description we have combined petrographic and geochemical data for each aspect and integrated these in the Discussion.

4.1. Mt Carmel Cretaceous volcanics

The ejecta from the Cretaceous volcanoes are dominated by "ash… made up of microvesicular glass in various degrees of preservation [and] lapilli and volcanic bombs [of] vitrophyric basalt, rich in vesicles and consisting of black glass (sideromelane), altered olivine phenocrysts and microlites of augite and plagioclase" (Sass, 1980). Most of the tuffs are water-laid (Yudalevich, 2007); many primary minerals are altered, and the matrix commonly contains secondary carbonates. The freshest lapilli (1–2 cm in diameter) typically comprise smaller individual lapilli, many of which are themselves composites, cemented by fine-grained material altered to various degrees (Supplementary Material, Fig. S-2). Tuff lapilli from the main vent of the Rakefet Magmatic Complex consist largely of petrographically isotropic but devitrified and hydrated glasses; basaltic lapilli are clinopyroxene-phyric with apparently fresh groundmass plagioclase while more mafic minerals are altered to cryptocrystalline material. Grain size and the degree of crystallinity vary widely, and large zoned phenocrysts of clinopyroxene are abundant. Petrographic and geochemical studies (DeBeers Africa Exploration, internal document, 2005) concluded that the primary magma was an olivine monchiquite/basaltic lamprophyre.

The largest homogeneous parts of individual basaltic clasts were analysed using SEM-EDS areal analysis. Analytical sums typically are <90 %, suggesting a large "loss on ignition"; analyses in Supplementary Material, Table S-1 are normalized to a volatile-free basis. Despite the textural variation, the suite is relatively homogeneous in composition; differences between clasts mainly reflect variations in the proportions of clinopyroxene *vs* olivine + orthopyroxene. Positive correlations of Fe and Mg suggest minimal fractional crystallization. The mean composition of the clasts (n = 50) is olivine-orthopyroxene normative; its low SiO_2

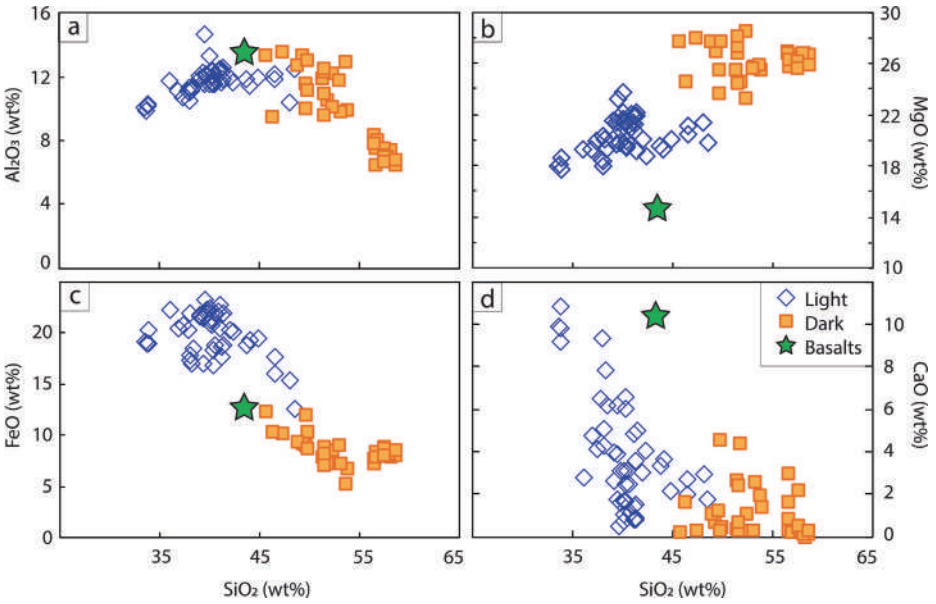

Fig. 2. Major-element plots for glasses in tuffs of the Rakefet Magmatic Complex; green star shows mean composition of Cretaceous basalts from Mt Carmel.

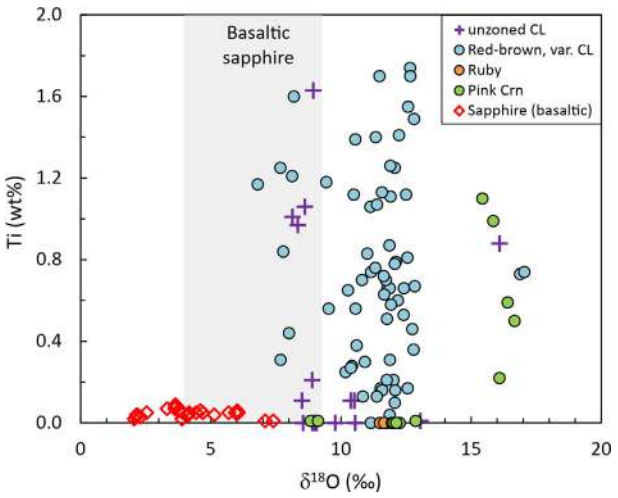

Fig. 3. Oxygen-isotope analyses of corundums from Mt Carmel. Grains with "unzoned CL" may be either *Crn-B* (high-Ti) or *Crn-C* (low-Ti); others are strongly zoned *Crn-A*. Data from Supplementary Material Table S-3.

(43.5 wt%) and $Na_2O + K_2O$ (<1 wt%) classify it as a tholeiitic picrite, although the mean P_2O_5 content is high (1.2 %). The alkali elements and SiO_2 may have been modified by alteration, but the compositional similarity between the least cpx-phyric varieties (with the highest proportion of easily altered groundmass) and the microgabbros makes this seem unlikely. Furthermore, Sass (1980) has noted that the most common type of alteration is spilitization, which would add Na.

Dark lapilli from the "black pyroclastic" vent facies (Sass, 1980) of the Rakefet Magmatic Complex comprise irregular fragments of devitrified felsic and mafic glass. The mafic glass ("LOI" from EPMA analyses = 10–20 %; light in BSE images; Supplementary Material, Fig. S-2) sits in a fine-grained felsic matrix, isotropic under crossed polars and darker in petrographic and BSE images. The felsic glass typically contains fragments of mafic glass, cpx and feldspar and many shards have a rim of the mafic glass. The felsic glass also occurs as round to irregular inclusions within shards of the mafic glass; some shards have a foliation suggesting the mingling of two distinct melts. Subangular to rounded bodies of carbonate occur mainly in the mafic glass; some may be vesicle fillings, but others may be balls of carbonate melts. Many vesicles contain apatite with 2–3 wt% SO_2.

Large-area EDS analyses show that both mafic and felsic glasses have high MgO contents, but the high-SiO_2 glass has the higher Mg# (85 *vs* 65; Supplementary Material, Table S-1); neither type contains measurable Na or K. The low-SiO_2 glass is olivine-opx normative, while the high-SiO_2 glass contains only normative opx. In the low-SiO_2 glasses MgO and Al_2O_3 are positively correlated with SiO_2 (Fig. 2), while FeO and CaO are negatively correlated. In the high-SiO_2 glasses, the only clear correlations are decreases in Al_2O_3 and FeO with increasing SiO_2. The compositional gap between the two populations of glass, combined with the petrographic observations, suggests that the tuffs from the RMC sampled at least two immiscible magmas. The mafic component was especially volatile-rich, leading to the production of highly vesicular fragments. In most of these plots the crystalline basalts lie outside the trends defined by the two types of "glass". The low-SiO_2 glasses are compositionally similar to some meimichites; the high-SiO_2 glasses resemble some boninites but have higher MgO than most.

Basalts from flows intercalated with tuffs and limestones on Mt Carmel have higher average contents of SiO_2, Al_2O_3, Na_2O and K_2O, but much lower MgO contents than the lapilli in the tuffs and classify as alkaline to subalkaline basalts (Kaminchik et al., 2014; Supplementary Material, Table S-1). They also have significantly lower Mg# than the analyzed lapilli or glasses and are more evolved than the magmas that accompanied the explosive eruptions. This evolution probably involved the fractional crystallization of olivine and cpx, the major phenocrysts in the lavas (Kaminchik et al., 2014). However, modelling using the MELTS software indicates that the basaltic lapilli in the tuffs do not represent parental melts to the Cretaceous basalts.

4.2. Basalt-megacryst suite

This suite includes several minerals that are found as coarse-grained xenocrysts in many alkali basalts worldwide; they are commonly linked to the crystallization of differentiated mafic magmas in the deep crust or uppermost mantle.

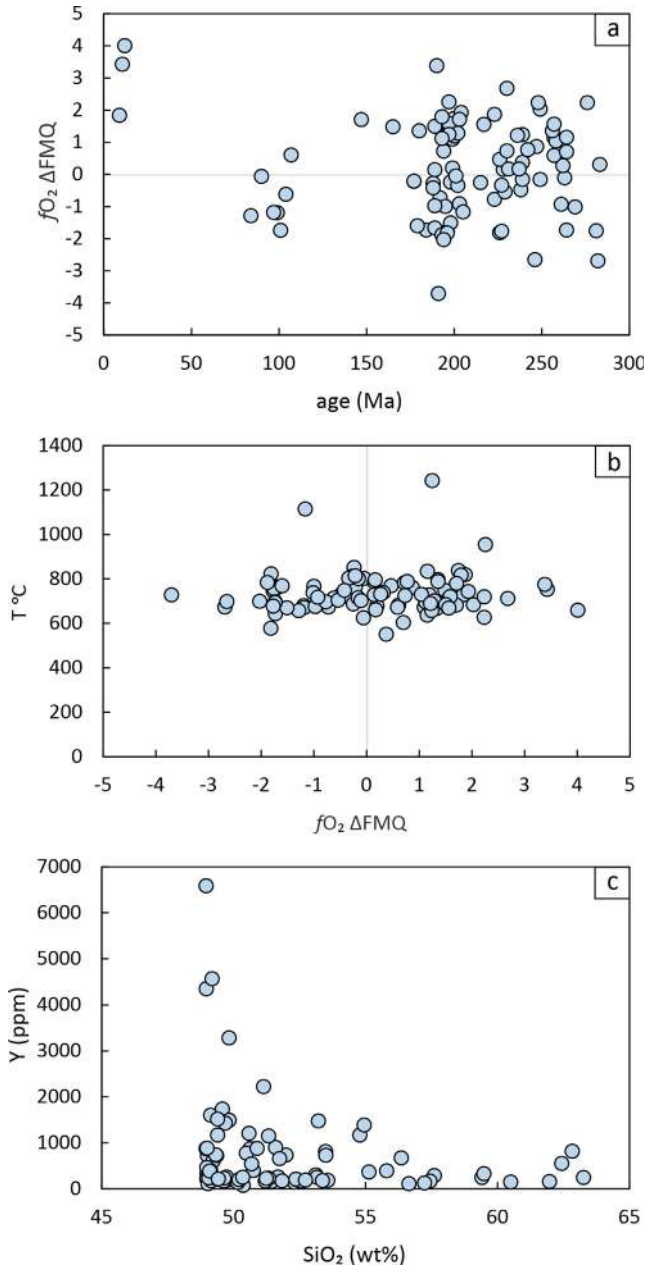

Fig. 4. Synthesis of data on zircons from Mt Carmel vents. (a) fO_2 of host melts (Loucks et al., 2020) *vs* age (Griffin et al., 2018a); (b) Ti-in zircon T (Fu et al., 2009) *vs* fO_2; Y content *vs* calculated SiO_2 of host melts (Turner et al., 2020).

4.2.1. Corundum

Monocrystalline grains of corundum up to > 2 cm across are found in all of the primary centres and the gem placers; most are anhedral fragments, but some retain crystal shapes or euhedral colour zoning. They can be divided into red–purple varieties (ruby) and sapphires, which range from colourless or pale pink to yellow and dark blue. Rubies are much rarer than sapphires, typically much smaller (<2mm) and have been recovered from the Rakefet, Har Alon and Beit Oren vents (Fig. S-1), as well as the placer deposits. Monocrystalline rubies and sapphires typically show little or no cathodoluminescence (CL). One monazite inclusion and one Na-K feldspar inclusion have been seen in the blue sapphires.

Trace-element contents of representative samples are given in Supplementary Material, Table S-2. The blue sapphires tend to have lower Fe, higher Mg, Ti, V and Cr, and significantly lower Ga/Mg than the paler varieties. The rubies contain 0.3–2 wt% Cr and have very low contents of Mg, Fe and Ti. A high-Ga/Mg group has much lower contents of Mg, Ti and Fe than the low-Ga/Mg group, but higher Zn and Ga.

Oxygen-isotope analyses of 13 blue to green sapphires range in $\delta^{18}O$ from 2 to 7.5 ‰, with a mean and median of 4 ‰ (Fig. 3; Supplementary Material, Table S-3); these values are typical for basalt-borne sapphires and are considered indicative of a mantle derivation (Sutherland et al. 2009; Graham et al., 2019). The $\delta^{18}O$ data for the rubies link them to the SUR mineral suite and are discussed below.

4.2.2. Zircon

Zircon "megacrysts" are typically several mm long, with euhedral to highly irregular external forms (Griffin et al., 2018b). CL images reveal complex histories involving magmatic crystallization, brecciation, recrystallization and overgrowth. The age spectrum of zircons from the Cretaceous volcanics shows semicontinuous magmatism from *ca* 300 Ma to 100 Ma, with peaks around 275 Ma, 240 Ma, 190 Ma and 100 Ma. Zircon populations from the Plio-Pleistocene placers have additional peaks at 80–90, 28, 10–14 and 3–5 Ma. Core-rim microstructures are common: Permian cores in Triassic zircons; Permian or Triassic cores in Jurassic zircons. Observed inclusions are pyrite, apatite, clinopyroxene and K-feldspar. Most grains have $\varepsilon Hf_{(t)}$ of + 5 to + 10; the scatter of data between the Hf-isotope evolution lines for the DM and CHUR "reservoirs" is similar to that observed in zircon megacrysts from kimberlites worldwide (Griffin et al., 2000; Woodhead et al., 2017). $\delta^{18}O$ values range from 3.7 to 5.9 ‰, (mean 5.1 ‰); most are within the accepted "mantle range" of 5.6 ± 0.6 ‰ but lighter values are found in grains that show late brecciation and recrystallization. In the CART classification (Belousova et al., 2002) 47 % of the zircons classify as syenitic, 33 % as monzonitic and 11 % as carbonatitic. This pattern is typical of mantle-derived zircons in continental settings, which usually are interpreted as forming in late differentiates of mafic magmas.

SiO_2 contents of the parental melts, estimated from Th/Y systematics (Turner et al., 2020) are 52 ± 4 wt% for zircons with both syenitic and monzonitic signatures, and the mean SiO_2 contents of the melts increase with decreasing age and Y contents (Fig. 4). Zircons from higher-SiO_2 melts are generally more enriched in incompatible elements. The Ce-U/Ti oxybarometer of Loucks et al. (2020) gives fO_2 values of ΔQFM = 2 ± 2 for most Permo-Triassic zircons, but nearly half of the Jurassic and Cretaceous zircons record fO_2 < QFM (Fig. 4). This may suggest that the reducing conditions seen in the Cretaceous Mt Carmel material studied here also were experienced during earlier magmatic episodes.

4.2.3. Mg-Ilmenite

Ilmenite grains are up to centimetric in size; some are subhedral to euhedral but most are fragments. There is a wide but coherent range in composition within several of the smaller primary volcanic centres, and in ilmenites from the paleoplacer deposits (Fig. 5). MgO contents range from 1.8 to 7.8 wt% (6.7–28.5 % (mean 14.7 %) of the geikilite component and are positively correlated with TiO_2 contents (Supplementary Material, Table S-4). Some higher-MgO grains resemble megacrysts from kimberlites in this regard (Fig. 5a). However, unlike most kimberlitic ilmenites, calculated Fe^{3+} contents are high (mean $Ilm_{64.2}Hem_{20.5}Geik_{14.7}Pyro_{0.6}$; Fig. 5b). Contents of Cr_2O_3 in this dataset are < 0.07 wt% (mean 0.03 wt%).

A large ilmenite dataset from the tuffs of the Rakefet Magmatic Complex (Fig. 1b; Fig. 5c) shows a wider range of both MgO and Cr_2O_3, up to 16 wt% and 1.2 wt%, respectively. High values of Cr_2O_3 are not confined to high-MgO grains, but in grains with >10 wt% MgO, MgO and Cr_2O_3 are positively correlated, while

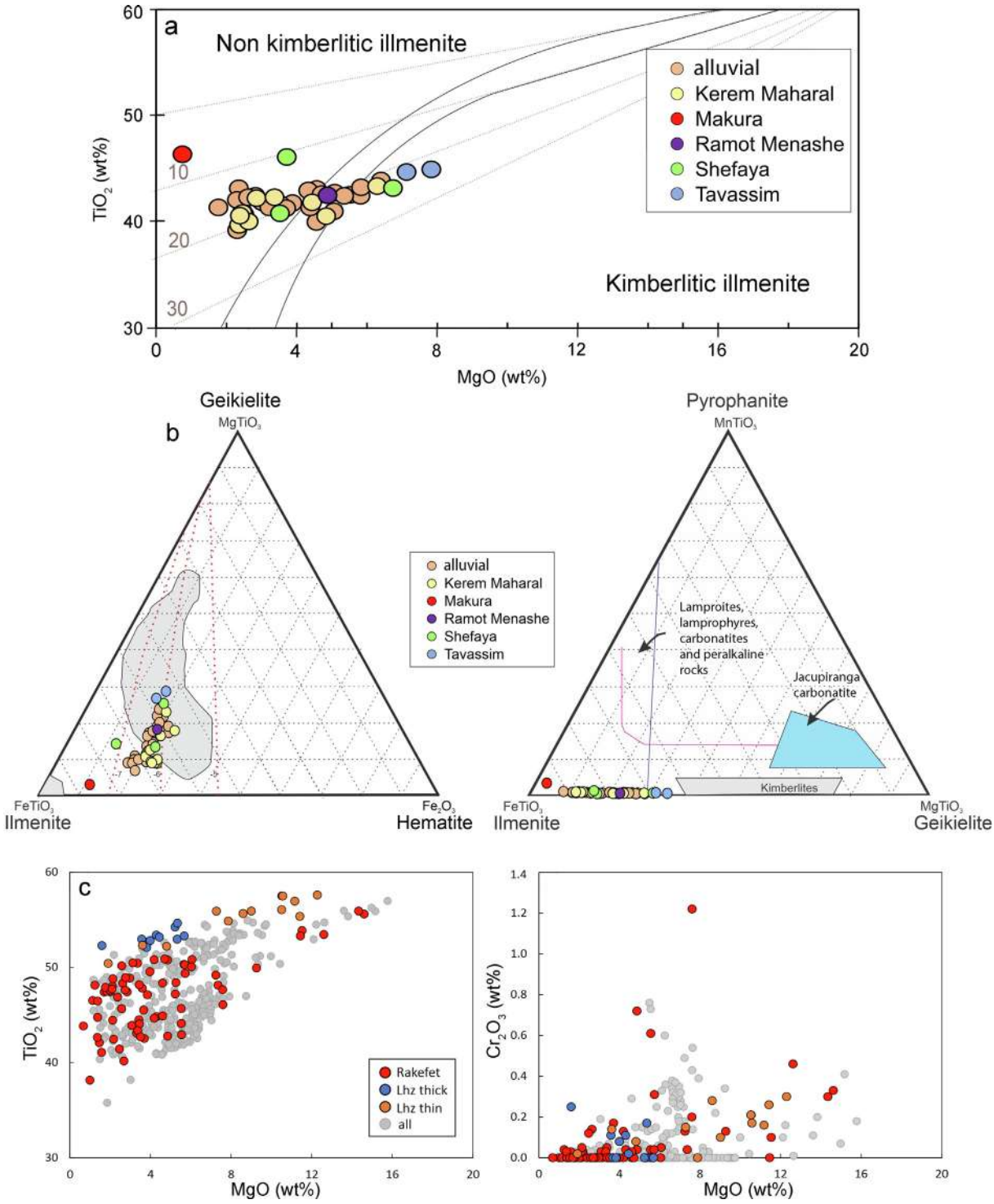

Fig. 5. Chemistry of ilmenite "megacrysts" from Mt Carmel volcanic vents. (a) Plot of MgO *vs* TiO_2 for kimberlitic and non-kimberlitic rocks. Contours of % Fe_2O_3 are shown as dashed light-grey lines. The black curve at lower MgO represents the boundary of the non-kimberlitic ilmenite field. The black line at higher MgO represents the boundary of kimberlitic ilmenite compositions from localities in South Africa and Namibia. After Wyatt et al. (2004). (b) Grey fields, ilmenite megacrysts in South African kimberlites (Wyatt et al., 2004). (c) Comparison of ilmenites from Mt Carmel with ilmenites in pyroxenite veins (thick *vs* thin) in peridotites of the Lherz massif (Lorand and Gregoire, 2010).

MgO and Fe^{3+} are negatively correlated. Most of this high-MgO, high-Cr_2O_3 population has ≤5 % Hem and is similar to kimberlitic ilmenite megacrysts (Wyatt et al., 2004).

The main population of low-Cr ilmenites can be matched with grains in low-MgO garnet pyroxenite xenoliths from the Mt Carmel volcanics (Lu et al., 2022). No xenolith analogue has been found for the higher-Cr, less-oxidized ilmenites. However, they resemble ilmenites in amphibole-rich high-pressure (1.2–1.5 GPa) veins that crosscut the Lherz (France) orogenic lherzolite massif (Lorand and Gregoire, 2010; Fig. 5c).

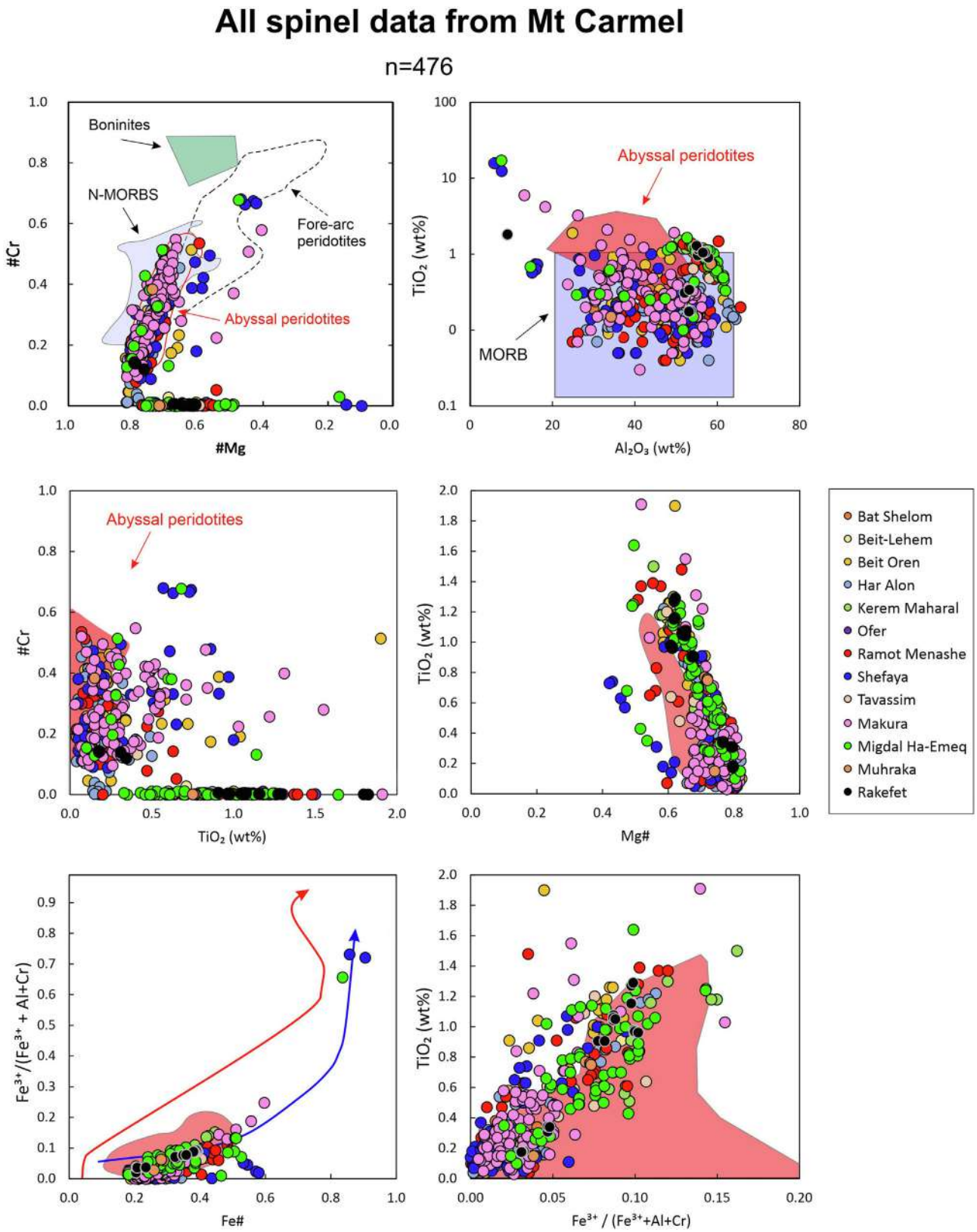

Fig. 6. Analyses of spinels from Mt Carmel vents. Red field, spinels from abyssal peridotites. Red line in (e) encloses 50% of spinels from Large Igneous Provinces; blue line in (e) is the Fe-Al magmatic trend (basalts and gabbros; Barnes and Roedder, 2001).

4.2.4. Clinopyroxene

Clinopyroxene megacrysts can be > 1 cm long; they typically are anhedral fragments but some retain crystal shapes. The main population (n = 170) shows little variation in composition (Supplementary Material, Table S-4); they are augites rich in Ca-Tschermak's molecule. One minor group has higher FeO and SiO_2 but lower Al_2O_3, MgO and CaO. Observed inclusions are Fe-Mg-Al spinel with relatively high Fe^{3+} (see below) and quandilite ((Mg,

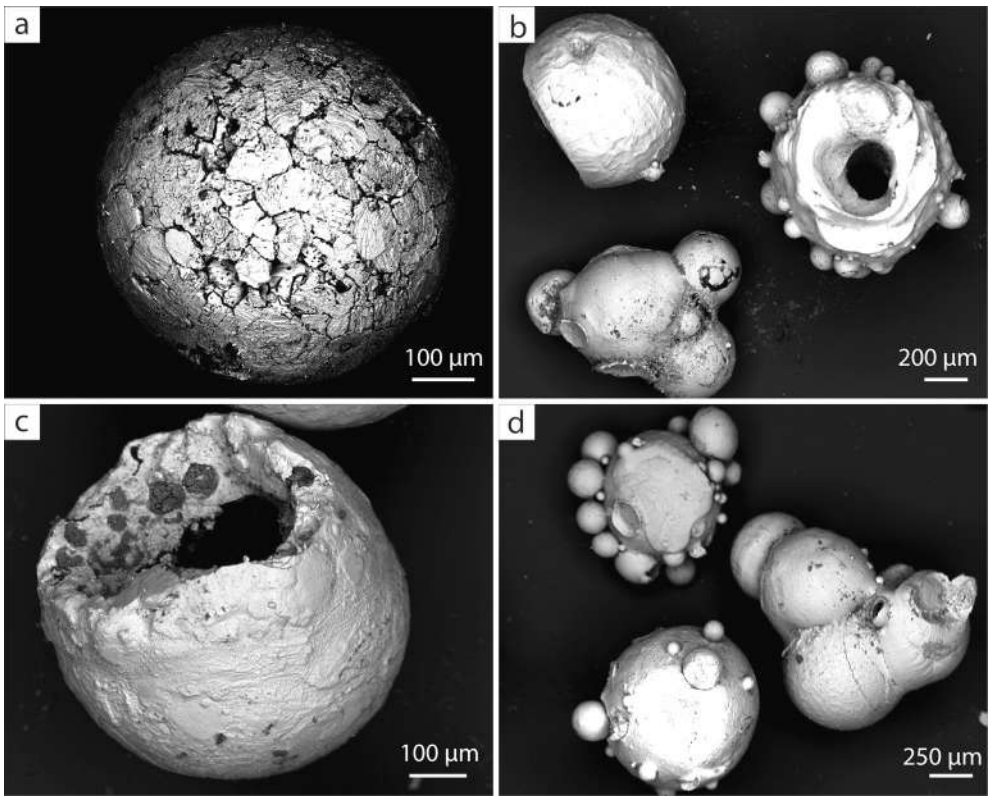

Fig. 7. BSE images of Fe-oxide balls from Mt Carmel tuffs; some show central voids. Crystals on the surface of (a) are FeO; (b-d) are microcrystalline but close to FeO in composition.

Fe^{3+})$_2$(Ti,Al, Fe^{3+})O_4, an ulvøspinel phase). The main population is identical to cpx in low-Mg garnet pyroxenite xenoliths from Mt Carmel (Table S-4; Lu et al., 2022). The cpx megacrysts probably represent material from disaggregated coarse-grained pyroxenites, crystallized from mafic melts and recrystallized during cooling at P = 20–25 kb, in the deeper part of the lithospheric mantle beneath the area (Lu et al., 2022).

4.2.5. Spinel

Spinel is abundant in heavy-mineral concentrates from both the vents and the alluvial deposits. Most grains are millimetric, but some are up to cm size, red and transparent. Analyses (Fig. 6; Table S-4) show two distinct populations: a Cr-series with Cr# (Cr/(Cr + Al) of 0.1 to 0.7, and an Al-series with little Cr but high Ti, Fe and Fe^{3+}. The Cr-spinels commonly have "holly-leaf" morphology and a wide range in Cr# over a narrow range of Mg# (Mg/(Fe + Mg)); they are typical of spinels from xenoliths of spinel-facies peridotites. Within this group there are two broad clusters, with Cr# = 0.1 to 0.3, and 0.4 to 0.55, respectively. Comparison with data on xenoliths from continental margins (Davis et al., 2007) suggests that the higher-Cr subset represents fragments of mantle peridotites, while the lower-Cr subset may be derived from cumulate gabbros and troctolites.

The Al-series spinels show more variable morphology, including octahedral grains. They appear to have crystallized from Cr-poor, Fe-Ti-rich melts; TiO_2 contents reach 1.5–2 wt%. Fe^{3+} increases together with Fe# and TiO_2, a typical magmatic trend (Fig. 6e). They are similar to Ti-rich spinels from seamount xenoliths (Davis et al., 2007) and to spinels from basalts in large igneous provinces.

4.3. Carbonates

Carbonate fragments derived from subjacent limestones are abundant in the tuffs. However, carbonates also comprise aggregates of 20–100 µm euhedral to subhedral crystals of high-Mg dolomite (molar Mg/Mg + Ca up to 0.54, FeO to 3 wt%; Supplementary Material, Table S-4; Fig. S-4), commonly enclosed by a euhedral rim which may be overgrown in turn by high-Mg calcite. The aggregates typically are outlined by tiny grains of unidentified Ti-oxides and sulfides. The highest Mg/Mg + Ca values are found in crystal cores, or in late overgrowths. LA-ICPMS analyses of cores also typically contain 0.3–0.7 wt% S, probably in sulfide microinclusions (Table S-4). These carbonates are interpreted as magmatic; the highest Mg/Mg + Ca values correspond to temperatures of > 1000 °C on the dolomite-magnesite solvus at P = 0.2–1.5 GPa (Goldsmith and Heard, 1961; Anovitz and Essene, 1987).

LA-ICPMS Rb-Sr analysis (Supplementary Material, Table S-5) shows that the cores have a mean $^{87}Sr/^{86}Sr$ = 0.7060 ± 0.0008 (2σ), while the rims have higher values (0.7088 ± 0.0005), as well as higher mean Sr contents. Analyses of isolated grains in the tuff matrix have $^{87}Sr/^{86}Sr$ identical to the rims; this is slightly higher than mean Cretaceous seawater (0.7075; Veizer, 1989).

4.4. Other mantle-derived phases

Olivine (Fo_{89-90}) is rare in the Cretaceous pyroclastic deposits due to alteration, but common in sediments derived from the Miocene-Pliocene basalts of the Yizre'el valley. Opx occurs rarely as large single crystals; its chemistry is consistent with derivation from spinel lherzolites. Cr-diopside is abundant and similar to cpx from spinel lherzolites. Abundant garnet in heavy-mineral concentrates is derived mainly from garnet pyroxenites but some low-Cr pyropes are similar to those in fertile garnet-spinel lherzolites worldwide (Lu et al., 2022). Amphibole megacrysts are abundant in the Har Alon vent, but rare elsewhere.

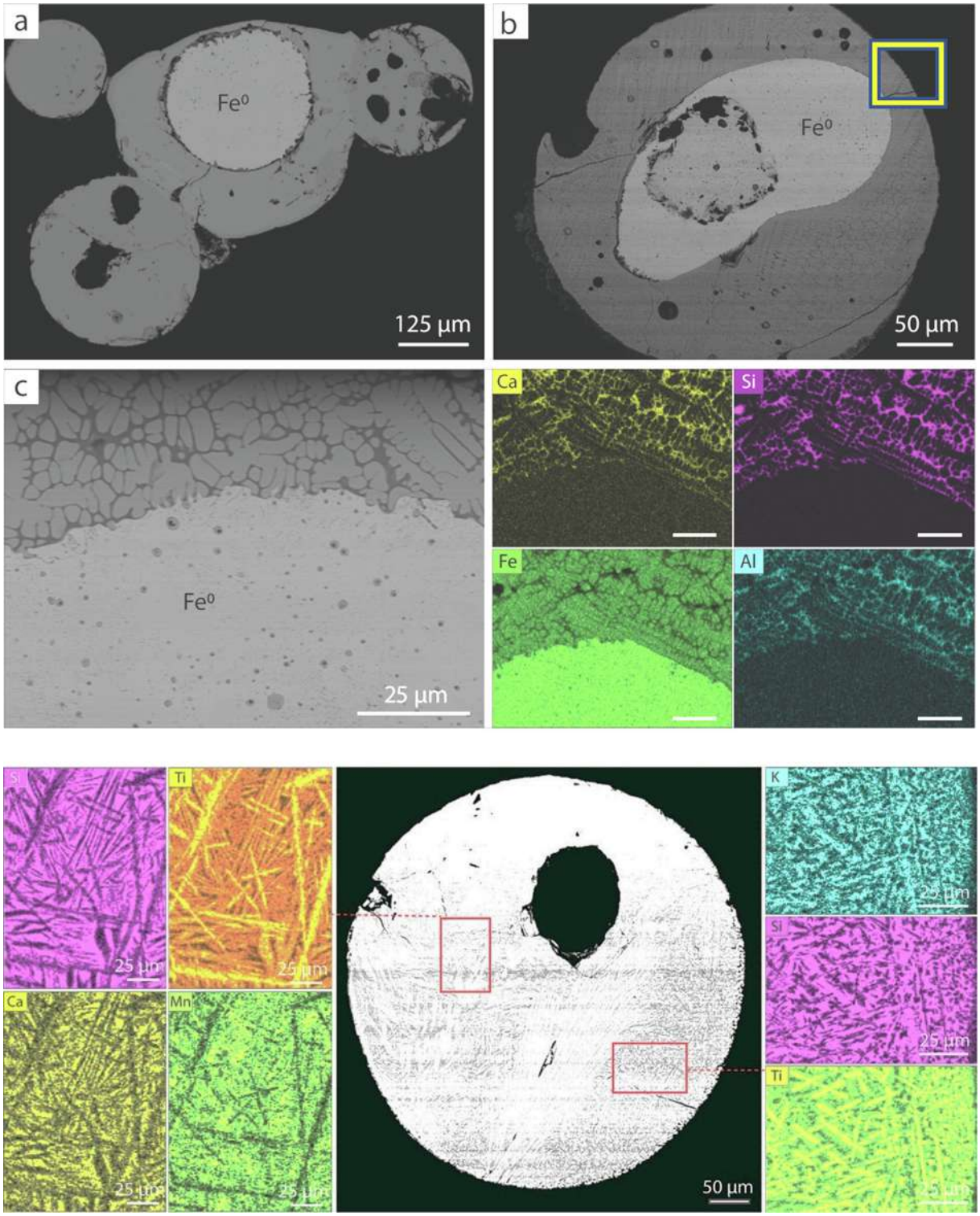

Fig. 8. Above; (a), (b). BSE images and element maps of Fe-oxide balls with cores of Fe^0 and rims of ferroarmalcolite crystals in silicate matrices. The example in (b) has an inner core of iron alloyed with Mn; the shape of the outer core suggests it was originally molten. Box shows location of maps in (c). (c) The Fe^0 core in contains abundant droplets with compositions similar to the rims; many also contain a vesicle. Below, element maps of a vesicular ball consisting of ferroarmalcolite in a silicate matrix.

4.5. Reduced and super-reduced parageneses

4.5.1. Iron-, iron oxide- and Fe-Ti oxide melts

The pyroclastics and the paleoplacer deposits contain abundant spherules up to 3 mm in diameter of native iron (Fe^0) and a range of Fe-Ti oxides (Fig. 7). Some balls are alloys of Fe with Mn, Cr and Ni. The Fe^0 balls are commonly surrounded by rims of Fe-Ti oxides, and some Fe^0 cores contain many tiny inclusions of FeO, each with a bubble of unknown composition. Similar oxides occur as spheres or aggregates of spheres, many of which are vesicular or contain one large spherical central void (Fig. 7). The oxides may be microcrystalline or coarsely crystalline with finer-grained rims (Fig. 8). Three populations have been recognized in terms of bulk composition (SEM-EDS areal analysis; Supplementary Material, Table S-6): (1) $\geq$ 80 wt% FeO, $\leq$10 wt% TiO_2; (2) mean FeO 38 wt%; TiO_2 40 wt %; (3) mean FeO 15 wt%; TiO_2 54 wt%. The first type, where

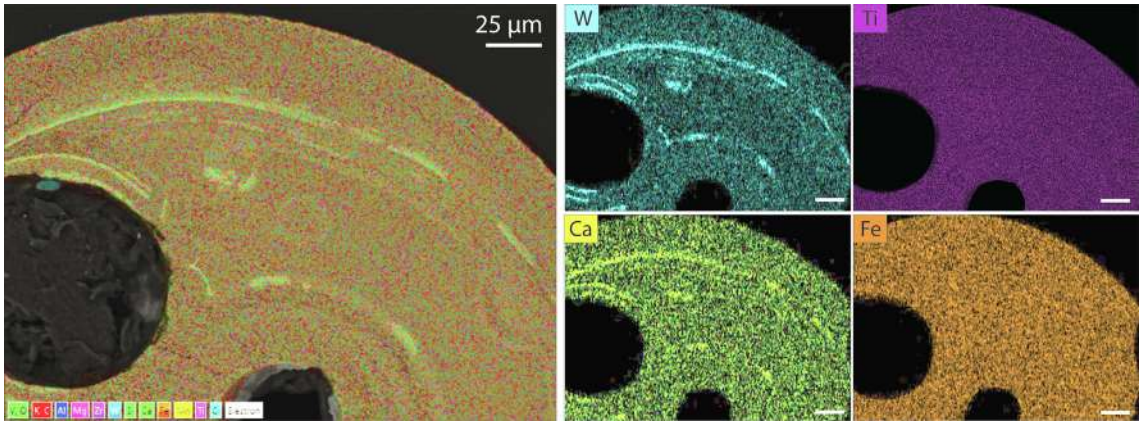

Fig. 9. Element maps of a portion of a vesicular, oscillatorily-zoned Fe-Ti-oxide ball. See analyses in Supplementary Material, Table S-6.

crystalline, consists of skeletal crystals of nearly stoichiometric FeO in a matrix richer in Si, Ca and Al. The more Ti-rich varieties commonly crystallize blades of Si-rich ferroarmalcolite ($Fe^{2+}Ti_2O_5$; Fig. 8; Table S-6) in a matrix rich in Si, Ti, Ca and K; some microcrystalline types show fine oscillatory zoning (Fig. 9). Some contain crystals of tephroitic fayalite (analysis 689-2c).

The interstitial matrices in the oxide spherules show wide variations in Ca, Mg, Al, Ti and Si (Table S-6). In Fe-oxide shells on Fe^0 cores (Fig. 8a) the matrix concentrates Ti, Al, Ca and Si, while in the Fe-oxide and Fe-Ti-oxide spherules the matrix concentrates Si, Al, Ca and Mg. In the Ti-oxide spherules, the matrix concentrates Si, W and S relative to the ferroarmalcolite blades.

Some Fe^0 and oxide spherules are enclosed in frothy fine-grained devitrified silicate glass with pronounced oscillatory zoning, defined by variations in (Fe + Mn) *vs* (Si + K) (Fig. 10). This frothy glass is much richer in Ti and Ca than homogeneous glass spherules found attached to Fe-Ti oxide balls (Supplementary Data, Table S-6) but is broadly similar to the average of silicate matrices in the crystallized Fe-Ti oxide spherules.

The microstructures suggest that the oxide spheroids represent ≥ 2 mutually immiscible metal-oxide melts, an Fe^0 melt and a silicate melt. Aggregates of spheroids may comprise any combination of these compositions. The abundance of hollow and/or vesicular spheres implies the additional presence of a mutually immiscible volatile phase. Several of these metal-oxide spherules are attached to fragments of corundum.

The vent pyroclastics and alluvial deposits also contain platy fragments of an iron monoxide, up to several mm across. These can be both mono- and polycrystalline, and many grains contain abundant vesicles (Supplementary Material, Fig. S-5). Some show minor zoning in MnO, which ranges up to 1.7 wt%; many grains contain traces of SiO_2 and/or Al_2O_3. Molar (Fe + Mn)/O ranges from 0.86 to 1.2, with a mean of 1.12. The microstructures of the grains suggest that they represent quenched fluid-rich melts rather than phenocrysts.

4.5.2. Hibonite-gehlenite cumulates

Microxenoliths recovered from two alluvial bulk samples comprise coarse-grained (100–500 µm) laths of hibonite, gehlenite, anorthite and 100–200 µm euhedral crystals of a Ni-rich Mg-Fe-Al spinel (chihmingite, $(Ni,Mg,Fe)Al_2O_4$) set in groundmasses with some or all of these phases as well as perovskite, kushiroite (Ca-Tschermak-rich pyroxene), grossite ($CaAl_4O_7$), possible Ca-lorenzite and unidentified Ca-rich phases, among them possible Ca-lorenzenite, $Ca_2(Ti^{4+}Al)O_3(SiAl)O_6$, a very rare pyroxene-like mineral. The microstructures (Fig. 11) suggest that these xenoliths represent cumulates from very aluminous, high-Ca melts. The cumulate mineral assemblages are: spinel (with interstitial anorthite, gehlenite); hibonite (with perovskite, gehlenite, spinel, kushiroite); hibonite + gehlenite (with anorthite); hibonite + anorthite (with gehlenite, anorthite, spinel, unknown phases); hibonite + gehlenite + anorthite (with kushiroite, spinel). Larnite (Ca_2SiO_4) and the unknown mineral $Ca_4Al_6O_{13}$ (synthesized at 1250 °C and 2.5 GPa by Kahlenberg et al., 2000) are rare interstitial phases. Corundum occurs as inclusions in hibonite in one sample, while in others the "cumulate" assemblage is in direct contact with large rounded grains of a low-Ti corundum.

In addition to minor Ti and Mg, the hibonite and gehlenite have significant contents of Fe and Ni (Supplementary Material, Table S-7), unlike the more reduced hibonite-bearing assemblages described below. In a plot of (Mg + Fe + Mn) *vs* (Ti + Si) (not shown) the hibonite analyses fall along a 1:1 line, suggesting low to zero concentrations of Ti^{3+}.

The structural formulae of the cumulate spinels (chihmingite) suggest that the tetrahedral site is fully occupied by (Mg + Ni), and that most of the Fe may be Fe^{3+} substituting for Al. Neither of these features has been observed in spinels from other parageneses found at Mt Carmel. The presence of Fe^{2+} + Fe^{3+} + Ni^{2+} suggests an fO_2 of *ca* ΔIW + 2.

4.5.3. High-Cr corundum assemblages

Rubies are rare in the Mt Carmel ejecta, and most have relatively low Cr_2O_3 contents (1–2 wt%). However, some samples contain more Cr-rich corundum that carries important information on the evolution of fO_2 in the Mt Carmel assemblages (Griffin et al., 2021b). In one assemblage (Supplementary Material, Fig. S-6), laths of corundum (Cr_2O_3 up to 15 wt%) coexist with Fe-Mg-Cr-Al spinels, Fe-Mg-Al-Na oxides and Fe-Ni alloys in an apparent cumulate microstructure; areas with barred intergrowths of the major phases suggest the crystallization of a eutectic melt. The corundum laths are zoned from high-Cr cores to lower-Cr rims. The compositions of coexisting spinels and alloys suggest crystallization at fO_2 near the IW buffer (ΔIW ± 1).

In some apparent cumulates, corundum prisms with low-Cr cores and still lower-Cr rims coexist with Cr-Fe alloys (Fe 45 wt %). In other examples, corundum with inclusions of native Cr (Cr^0) has low-Cr cores, but high-Cr rims (to >30 % Cr_2O_3). These different zoning patterns reflect the strong decrease in the melting point of Cr_2O_3, relative to that of Al_2O_3, with decreasing fO_2. At low fO_2 melts are more Cr-rich than the crystallizing corundum, while the reverse is true at high fO_2. EELS analyses show that Cr is present as Cr^{3+} in corundum coexisting with Cr^0, suggesting that Cr^{2+} has disproportionated via the reaction $3Cr^{2+}$(melt) → $2Cr^{3+}$(Crn) + Cr^0 and implying $fO_2 \leq$ ΔIW-5. The most Cr-rich

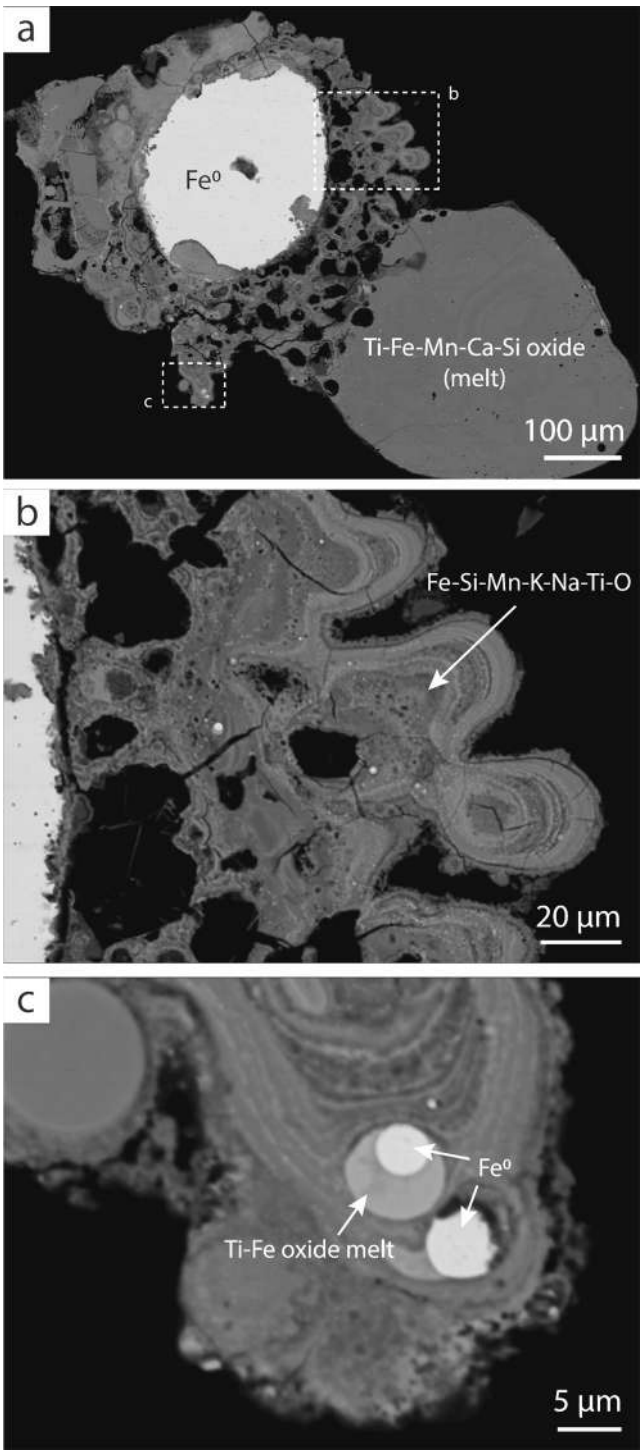

Fig. 10. BSE images of frothy, vesicular silicate melts coexisting with Ti-Fe oxide melts and Fe^0 melts, suggesting the presence of at least four mutually immiscible melts/fluids.

corundum crystallized together with β-alumina phases including $NaAl_{11}O_{17}$ (diaoyudaoite) and $KAl_{11}O_{17}$ (kahlenbergite) as well as β''-alumina phases; residual melts crystallized a range of unknown $(K,Mg)_2(Al,Cr)_{10}O_{17}$ phases with the kahlenbergite structure.

4.5.4. Hibonite-grossite-vanadium paragenesis

This paragenesis is found as rounded to angular xenoliths up to 2.5 cm across (Griffin et al., 2019a). Hibonite occurs as tabular crystals up to 1 cm long, in a matrix of granular grossite and spinel (commonly euhedral); fluorite was the last phase to crystallize (Supplementary Material, Fig. S-7). The oxyfluoride phase $Ca_4Al_6F_2O_{12}$ precedes fluorite in the crystallization sequence and coexists with grossite. Rare grains of perovskite ($CaTiO_3$) coexist with grossite or are intergrown with fluorite. Resorbed inclusions of corundum in hibonite laths indicate that hibonite crystallized via the peritectic reaction Crn + liquid/melt (L) → hibonite. This was followed by the cotectic precipitation of grossite, hibonite and spinel, and finally the assemblage grossite + spinel + krotite ($CaAl_2O_4$) + fluorite.

Small spherical inclusions of native vanadium (V^0) are common in both hibonite and grossite (Fig. S-7). V^0 with percent levels of Cr and Mn also occurs as spheres up to 500 µm across, either isolated within hibonite, or together with grossite and fluorite in pockets among hibonite grains. In some cases, vanadium inclusions in hibonite develop from spheres into 3D dendritic growths subparallel to the c axis of hibonite (Griffin et al., 2020a). The presence of V^0 requires $fO_2 \leq \Delta IW -9$, implying a coexisting hydrogen-dominated fluid phase. Kishonite (VH_2, the first natural hydride) was discovered attached to a V^0 ball (Bindi et al., 2020), and gasses released on crushing hibonite grains carry on average 67 ppm N, 1140 ppm C, 2800 ppm H and 480 ppm S (n = 4; Griffin et al., 2020b;). Raman spectroscopy shows that high levels of H occur in defects and interstitially in the lattice of the hibonite adjacent to V^0 inclusions (Griffin et al., 2019a).

The hibonite of this paragenesis is lower in REE by two orders of magnitude than those in the corundum aggregates (see below), but the REE patterns are essentially parallel, with similar negative Eu anomalies (Griffin et al. 2019a). The coexisting spinels contain percent levels of V (mean V_2O_3 31.3 ± 2.3 wt%, VO 21.4 ± 4.8 wt%) where V^0 is absent, but much lower levels when V^0 is present. The most V-rich spinels correspond to dellagiustaite ($(AlV^{2+}V^{3+})_3O_4$); Cámara et al., 2019), which occurs in Argentinian samples very similar to the Mt Carmel hibonite-grossite-V^0 material.

4.6. Corundum aggregates

4.6.1. Paragenetic types

The most abundant gem mineral from the Mt Carmel volcanics comprises aggregates of corundum crystals. These range from colourless through orange-brown to dark blue, and in size up to 2.5 cm (33.3 carats); they have been marketed by Shefa Gems Ltd as "Carmel Sapphire™". Three parageneses have been recognized, with different Ti contents in corundum, different types of trapped melts and different mineral associations.

The most common type of aggregate (*Crn-A*) comprises crystals 100–200 µm across with skeletal to hopper morphology, typical of rapid growth. This process has trapped abundant pockets of the parental melt, which contain a veritable zoo of phenocryst minerals, metallic melts (see below) and voids that presumably contained volatile phases. Voids may also contain euhedral crystals of phenocryst minerals, possibly grown from the volatile phases (Supplementary Material, Fig. S-8). 3D X-ray µCT imagery of 6 aggregates (see Graphical Abstract; Supplementary Material, Figs S-9, S-9-v) indicates that crystallographically-defined voids comprise 0.3–2.3 vol% (median 0.7 %). EELS spectra show that Ti is present in *Crn-A* corundum as Ti^{3+} (Oliveira et al., 2021). The growth process is recorded in complex cathodoluminescence (CL) patterns (Fig. 12a, b; Supplementary Material, Fig. S-10) related to variations in Ti content. The bright pale pink CL typical of low-Ti^{3+} corundum (<0.5 wt% Ti) is progressively extinguished as Ti contents increase first linearly, then exponentially, toward trapped pockets of silicate melt, to reach wt% levels (Fig. 12c).

Numerical modelling of the Ti-zoning patterns (Oliveira et al., 2021) indicates that the skeletal corundum crystals initially grew

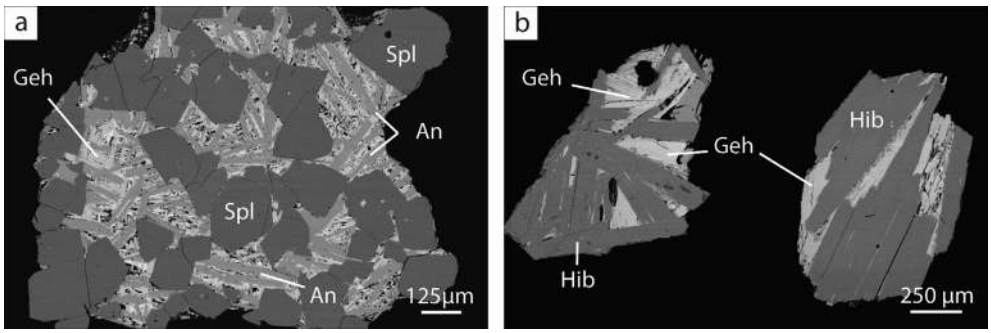

Fig. 11. BSE images of microxenoliths of the hibonite (Hib) – gehlenite (Geh) – spinel (Spl) – anorthite (An) association.

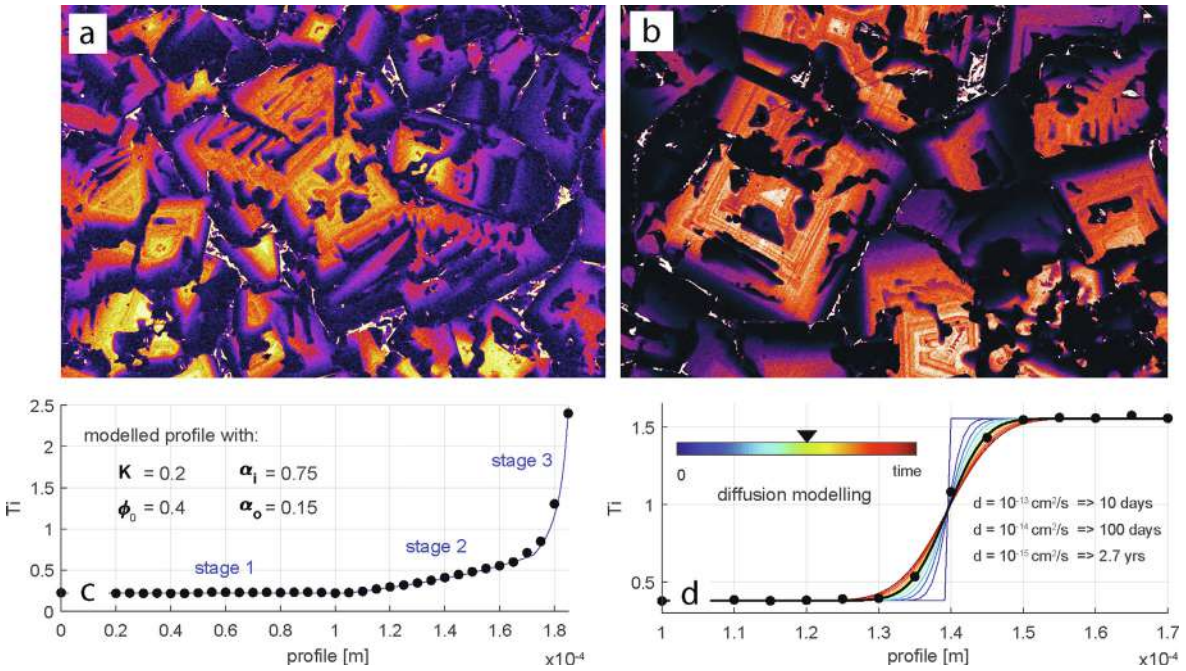

Fig. 12. a,b. False-colour cathodoluminescence (CL) images of Crn-A corundum. The true CL colour of the bright parts is pink; it fades to black as Ti contents rise toward the rims. The skeletal (“hopper”) growth pattern reflects very rapid crystallization, trapping the Ti-rich melt in the porous skeletal structure. c, typical Ti zoning profile from light to dark CL, showing growth stages discussed in the text. d, diffusion modelling of a stage 3 growth profile, which probably developed shortly before eruption of the host magma. After Oliveira et al., 2021.

in open systems with a through-flowing magma, giving a low and homogeneous Ti content. The subsequent linear increase of Ti contents in the growth direction (Fig. 12c) reflects decreasing porosity due to crystal growth, while the exponential increase in Ti near melt pockets marks the closure of the system, isolating melt pockets from the percolating melt. Calculations based on diffusion profiles and experimental growth rates constrain the growth process to periods of days to years prior to entrainment in the ascending host basalt (Fig. 12d).

Another paragenesis (*Crn-B*) consists of larger corundum crystals with high Ti contents (1.5–2.8 wt% Ti, mean 2.4 wt%) and no CL; most of these crystals are only weakly zoned in Ti. Contacts between grains tend to be smooth and interstitial melt pockets are dominated by coarse-grained phenocrysts with little glass but many irregular voids. There is little evidence of early skeletal growth as seen in *Crn-A* aggregates.

The third paragenesis (*Crn-C*) comprises coarse-grained aggregates of relatively low-Ti corundum (≤1.0 wt% Ti; mostly < 0.5 wt %), which typically has homogeneous pale CL and little if any zoning. Interstitial clusters of oxide and silicate phases are generally coarse-grained and few contain any glass. The corundum typically is colourless, but some aggregates take on a blue colour from inclusions of hibonite.

The CL images of corundum in all three parageneses, but especially *Crn-A*, show square cross-sections, and separated crystals show cubic forms (Fig. 12; Supplementary Material, Fig. S-10). These are pseudocubic rhombohedra, terminated by (0 1 2), ($\bar{1}$ 0 2), (1 0 $\bar{2}$), (0 $\bar{1}$ $\bar{2}$), (1 $\bar{1}$ 2), and ($\bar{1}$ 1 $\bar{2}$) faces (i.e., the {0 1 2} form). Similar forms are occasionally seen in other hexagonal-rhombohedral minerals including calcite (e.g., Hatipoglu and Chamberlain, 2011) and quartz (e.g. Tarr and Lonsdale, 1929). Gurlo et al. (2008) suggested that this morphology reflects rapid, kinetically-driven growth and/or the effect of other components on the surface energy of different faces.

4.6.2. Mineralogy of parageneses

Crn-A (Supplementary Material, Fig. S-11)**.** Melt pockets in aggregates with strongly Ti-zoned corundum typically show a crystallization sequence Mg-Al spinel → tistarite (Ti_2O_3) → carmeltazite ($ZrAl_2Ti_4O_{11}$; Griffin et al., 2016a). However, some spinels contain inclusions of tistarite, indicating a slightly differ-

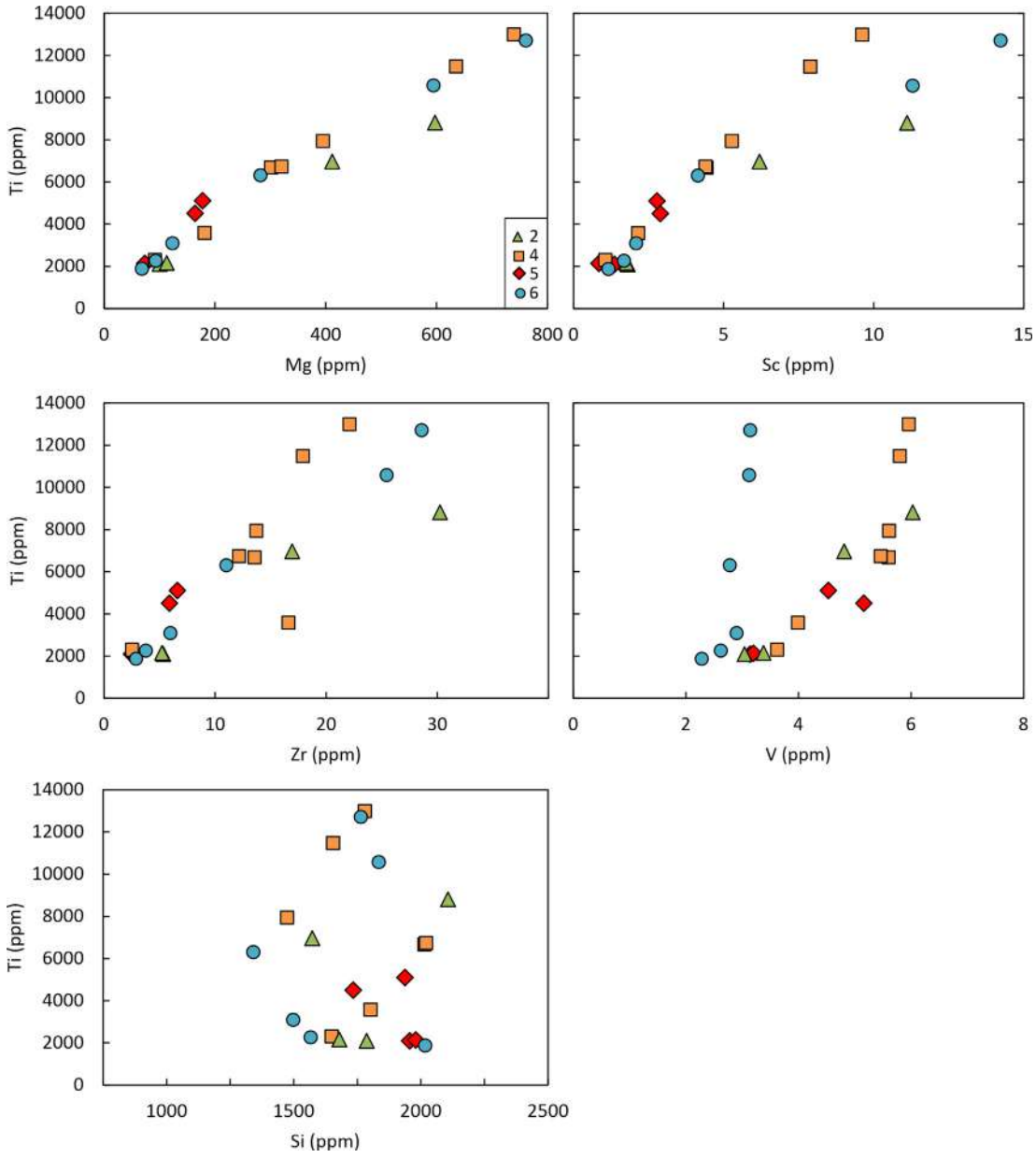

Fig. 13. Bivariate plots of trace-element analyses across four grains of corundum from the *Crn-A* paragenesis.

ent sequence. Some tistarite grains retain a primary cubic morphology, but most are rounded and overgrown by carmeltazite, which is typically skeletal and euhedral against the glass. The initial sequence is followed by a range of phases, including several unknown silicates, the most common of which is $MgTiAl_2(Si,Zr)O_8$. The glasses commonly contain rounded voids, suggesting the presence of a coexisting volatile phase. Late-crystallizing phases comprise a range of sulfides (TiS, (Ti,Cr)S, CaS, MnS), zirconolite and several unidentified REE-bearing phases, khamrabaevite (TiC), moissanite (SiC; Huang et al., 2020), and jingsuite (TiB_2; Griffin et al., 2020a). Residual glasses commonly contain needles or blades of dmisteinbergite ($CaAl_2Si_2O_8$), a quench phase.

Crn-B (Supplementary Material, Fig. S-12). Pockets in aggregates of high-Ti corundum with little Ti-zoning display several crystallization sequences.

- $(Ti^{3+}, Al)_2Ti^{4+}O_5$ + melt. The oxide phase (an Al-rich sassite) forms long rods in glass; the ends of the rods are overgrown by the host corundum, which is euhedral against the glass (Fig. S-12a).
- $(Ti,Zr)O_2 \rightarrow Ti_2Al_2O_6 + (K,Na,Ca)Al_2Si_7O_{18}$ + melt.
- Tistarite → carmeltazite → hibonite + melt. (Mn,Ca,Ti,Fe)S, nöggerathite and $Zr(Ti,Al,Y)_4O_8$ are accessory phases.
- Tistarite → Ti-Al-Zr oxide + melt. Some tistarite has exsolved blades of kaitianite ($Ti_2^{3+}Ti^{4+}O_5$; Ma et al., 2023) (Supplementary Material, Fig. S-13).
- Tistarite → hibonite + melt

The interstitial pockets may be dominated by voids rather than melt, or contain melt but are connected to interstitial voids. Such voids may contain euhedral crystals of tistarite, carmeltazite, hibonite, or moissanite (Fig S-12e). Rare melt pockets contain dmisteinbergite quench crystals.

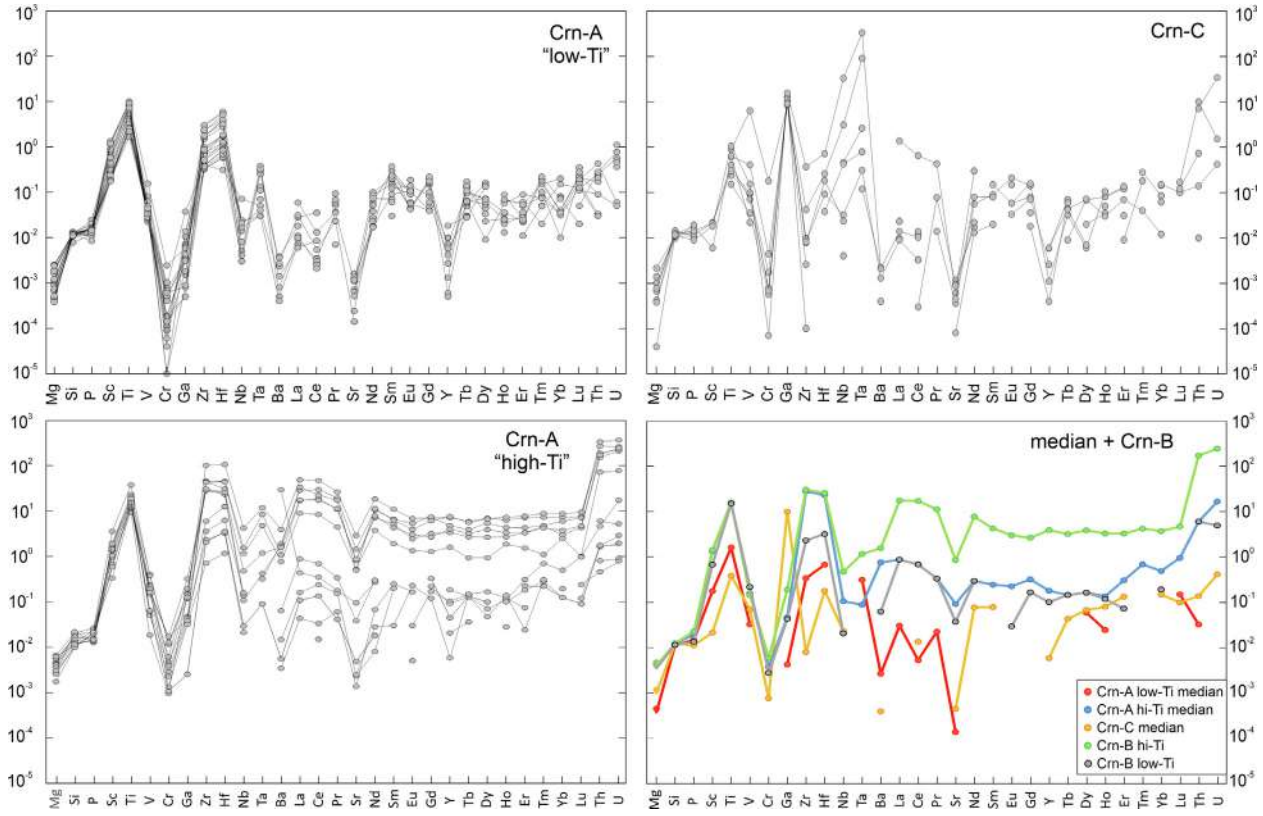

Fig. 14. Chondrite-normalized trace-element plots for corundum of parageneses *Crn-A, B* and *C*.

Crn-C. Melt pockets in this paragenesis (Supplementary Material, Fig. S-14) are dominated by hibonite and Ti-Al oxides; tistarite is absent. Observed assemblages are:

- Hibonite + melt
- Hibonite + $(Ti,Mg,Al,Zr)_{1.8}O_3$ (analog of panguite?) + melt
- Machiite $(Al_2Ti_3O_9)$ + $(Ti,Mg,Al,Zr)_{1.8}O_3$ + melt
- Griffinite $(TiAl_2O_5)$ + $(Zr,Ti)O_2$ + melt.
- Ti-Al-Zr oxide + hibonite + melt

As in *Crn-B*, voids are common and may contain euhedral crystals of the phases that coexist with the melts. Dmisteinbergite has not been observed as a quench phase.

4.6.3. Mineral chemistry

4.6.3.1. Corundum. Analyses of corundum in the aggregates are summarized in Fig. 13 and Supplementary Material, Table S-8. Details of the Ti-Mg zoning in *Crn-A* are given by Oliveira et al., (2021; see Fig. 12). The two elements are closely correlated in *Crn-A*. Ti is also positively correlated with Sc, Zr and V, but not with Si. The corundum in the *Crn-C* paragenesis contains only 0–1 wt% Ti or Mg, whereas the typical Ti contents of *Crn-B* are 2.0–3.5 wt%, extending beyond the levels in the high-Ti zones in Crn-A.

The extended trace-element patterns of the early-crystallizing corundum in *Crn-A* show low Ti and low HREE and LREE relative to MREE, with negative anomalies in Y and Sr (Fig. 14). At higher Ti contents (Fig. 14b), two populations are apparent, which correlate with the second and third growth stages defined by Oliveira et al. (2021). The higher-Ti population has a small positive Y anomaly; the pattern is essentially flat from Nd to Lu and rises toward La and Ce. Zr, Hf, Th, U, Nb and Ta all rise in concert with Ti. In the lower-Ti population the LREE are higher and the Y anomaly smaller. The two available LA-ICPMS analyses of corundum from Crn-B closely mimic the two populations in the high-Ti group of paragenesis Crn-A. Analyses of corundum from Crn-C are most similar to the low-Ti group in Crn-A, but stand out by their much higher Ga contents and much lower Sc, Ba, Zr and Hf; a few analyses have strikingly high contents of Nb, Ta, Th and U.

Besides Ti, the major differences between the "basaltic sapphire" megacrysts (section 4.2.1) and the aggregate corundums are in Fe and Ga; both elements and Ga/Mg are much lower in the *Crn-A* and *Crn-B* corundums, because Fe and Ga are sequestered into inclusions of immiscible Fe-Ti silicides (Griffin et al., 2022; see below). However, *Crn-C* corundum is notably enriched in Ga (*ca* 100x the levels in *Crn-A* and *-B*). Most of the corundum in the aggregates contains 1–14 ppm Sc, which is below detection in the "basaltic" sapphires and rubies, and >100 ppm Mg, while most sapphires and rubies contain <100 ppm Mg.

O-isotope data are presented in Fig. 3 and in Supplementary Material, Table S-3. While the "basaltic" sapphires of the megacryst suite lie within the range of mantle values, *Crn-A* shows a range in $\delta^{18}O$ from 6.8 to 17 ‰. Most values fall between 10 and 13 ‰; the mean and median values are 11.4 and 11.7 ‰, respectively. There is no clear correlation between Ti contents and $\delta^{18}O$. Two *Crn-B* grains have $\delta^{18}O$ of 8.2 and 8.7 ‰, but a third is at 16.1 ‰. Seven grains of *Crn-C* have $\delta^{18}O$ from 8.5 to 13.1 ‰, with a median value of 9.0 ± 1.3 ‰. Rubies have $\delta^{18}O$ values within the range of the *Crn-A* samples. Most pink sapphires fall in a distinct group around $\delta^{18}O$ = 16 ‰, but some with low Ti go down to $\delta^{18}O$ = 9 ‰.

4.6.3.2. Trapped melts. The melts trapped as glasses in the *Crn-A* aggregates are Ca-Al-Mg silicates with Ca≫K > Na, and a wide range in Ti, Ca, Al, Si and Mg. Much of this variation reflects the post-entrapment crystallization of corundum, producing negative correlations of most elements with Al, but these fractional-crystallization trends are modified to various degrees by crystal-

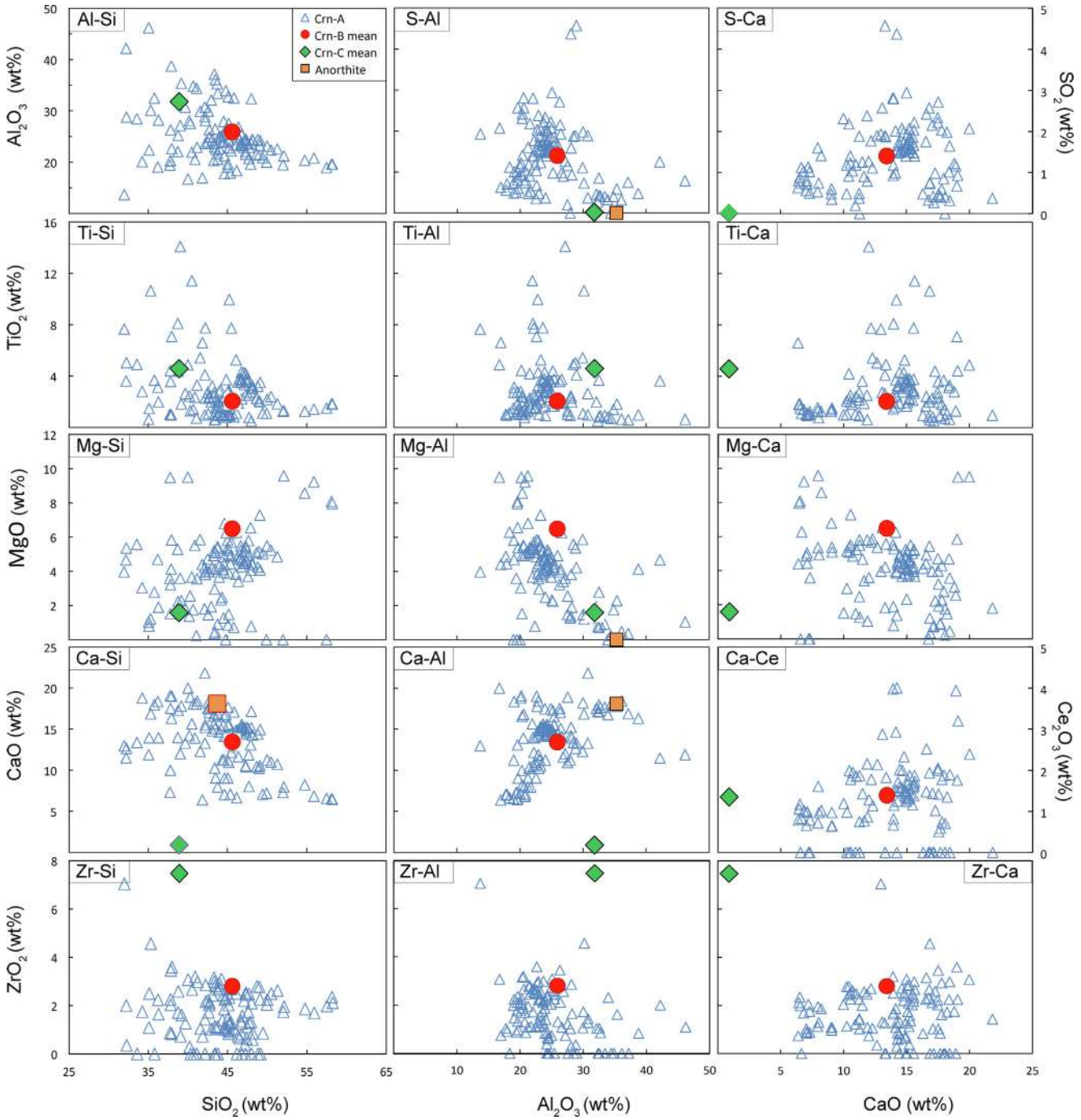

Fig. 15. Bivariate plots of oxide contents in melts trapped in corundum aggregates. While *Crn-B* melts appear closely related to *Crn-A* melts, the *Crn-C* melts are clearly different. The composition of anorthite is shown in plots where the crystallization of quench anorthite clearly has influenced the interelement trends (*e.g.*, Ca-Al).

lization of the phenocryst and quench phases described above (Fig. 15, Supplementary Material, Table S-9). Most EPMA analyses of the glasses have analytical totals of 85–95 %, suggesting abundant dissolved volatiles, which is consistent with the presence of spherical voids in many melt pockets. A TEM-EDS analysis (with no carbon coating) of a typical *Crn-A* melt (Supplementary Data, Table SD-9) provided a carbon content of 0.9 wt% C, or 3.2 wt% CO_2.

The mean values for elements such as Th, La and K in melts (Table S-9) are biased by outliers with high concentrations. Incompatible elements such as Ce and S show strong negative correlations with Al_2O_3; phenocryst-controlled elements such as Ti, Mg and Zr show more scattered negative correlations. A plot of CaO *vs* Al_2O_3 (Fig. 15) shows two well-defined correlations; the negative one is controlled by the fractional crystallization of corundum, and the positive one by the crystallization of dmisteinbergite as a quench phase. FeO contents are typically below 0.01 wt%, as Fe is strongly partitioned into the coexisting Fe^0 and Fe-Ti silicide melts.

The glasses have very high concentrations of Ti, Zr, Ba, REE and S. Binary plots (Fig. 15) show strong positive correlations of S with Ca and Al in the middle of the distribution, which suggests that the Ti-Mn sulfides began to crystallize from the trapped melts after removal of corundum (and/or quench dmisteinbergite?) had lowered Al_2O_3 from *ca* 38 wt% to *ca* 25 wt%, and CaO from *ca* 18 wt% to *ca* 13 wt%. Chondrite-normalized trace-element diagrams

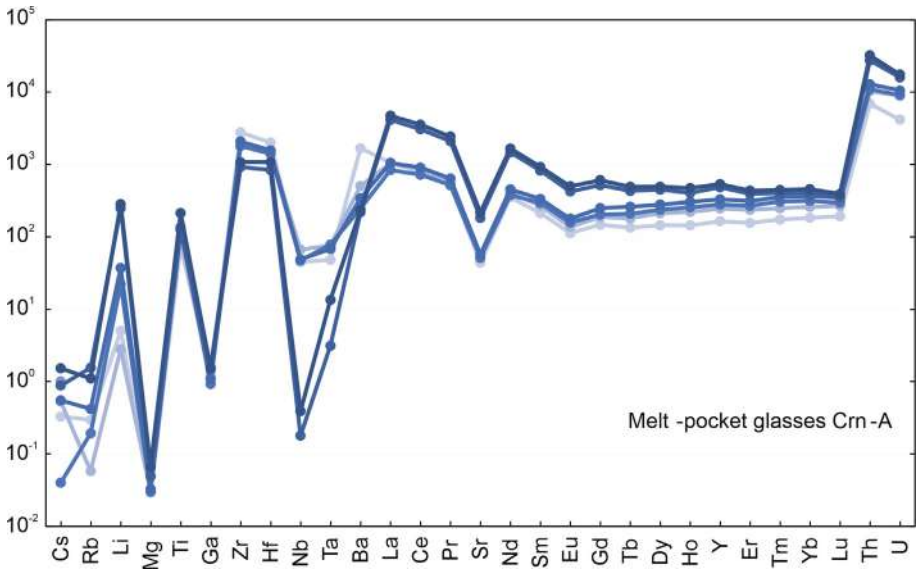

Fig. 16. Chondrite-normalized trace-element patterns of *Crn-A* melts.

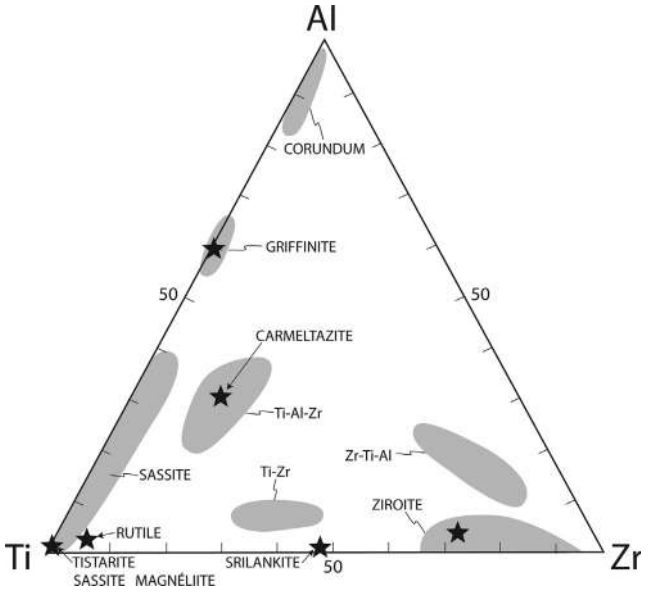

Fig. 17. Ti-Al-Zr triplot illustrating the range of compositions in known (stars) and unknown phases.

(Fig. 16) show flat HREE-MREE patterns, enrichment in LREE, U and Th, and negative anomalies in Mg, Ga, Sr, Nb and Ta. Overall the pattern resembles that of the high-Ti *Crn-A* corundum (Fig. 14), though at much higher concentrations. The principal differences are the greater enrichment of the LREE relative to Zr-Hf and Ti, the lower Ga/Ti and the slightly deeper Eu anomaly in the glasses.

Melts are less commonly preserved in the *Crn-B* and *Crn-C* samples; most glasses contain abundant phenocrysts and thus are extremely residual. The glasses in *Crn-B* are similar to those in Crn-A, but have higher mean Mg, Ca and Zr, higher Mg/Al and lower K, Na and Th. They typically contain < 0.05 wt% S, in contrast to the *Crn-A* glasses. The glasses in *Crn-C* are distinctly different, with lower Si, Mg, S and especially Ca, but higher mean Ti, Al, Zr and K. Another distinctive feature is their high contents of V, which is below EPMA detection limits in the other parageneses (LA-ICPMS analyses show a mean of 175 ppm in Crn-A glasses (Supplementary Material, Table S-9)). The unusually high Zr content of the mean Crn-C glass is consistent with the presence of minute quench crystals of baddeleyite and ziroite (polymorphs of ZrO_2; Ma et al., 2024).

4.6.3.3. Phenocryst phases. Ti-Al-Zr oxides

Ti-Al-Zr oxides are the most abundant phenocryst phases and cover a wide spectrum of compositions (Fig. 17; Supplementary Material, Table S-10). Tistarite (Ti_2O_3) typically contains < 0.6 at.% Zr (mean 0.1), <1.6 at.% Al (mean 0.84) and up to 4 at.% Mg (mean 1.4). Ti and Al are negatively correlated, but Zr shows no correlation with other elements. In some melt pockets in *Crn-B* aggregates, long rods of Al-bearing sassite occur as the only phenocryst (Supplementary Material, Fig. S-12).

Carmeltazite ($ZrAl_2Ti_4O_{11}$) shows a moderate range in composition, with Zr 5–7 at.%, Ti 19–23 at.% and Al 10.8–12.2 at.%. Zr is negatively correlated with Ti but positively correlated with Al, while Ti and Al are negatively correlated. Mg (1–2 at.%) and Si (typically 1 at.%) are the only significant minor elements. EELS spectra (Supplementary Material, Fig. S-15) and XRD (Griffin et al., 2018a) indicate that Ti is trivalent in carmeltazite.

A large population of Ti-Al-Zr oxides overlaps the field of carmeltazite, but with a much greater range in Zr:Al:Ti (Fig. 17). These are structurally and compositionally similar to the Ti-Al-Zr phases found in the Allende chondrite (Ma and Beckett, 2021) and are distinct from carmeltazite. They commonly appear as phenocrysts, or surrounding tistarite, in *Crn-B* and *Crn-C* (Supplementary Material, Fig. S-14). Stoichiometric calculations show a wide range of Ti^{3+}/Ti^{4+} (from *ca* 3–20; Supplementary Material, Table S-10). In parageneses *Crn-B*, these phases tend to have higher Ti and Al, but similar Zr to carmeltazite (Fig. 18). Those in *Crn-C* have generally lower Zr, Si and Sc and higher Al and Mg than those in *Crn-A* and *Crn-B*, but there is considerable overlap among the parageneses.

Ti occurs with mixed valence in several other phases in Fig. 17. A scatter of data along the Ti-Al join represents solid solution between sassite and griffinite (Al_2TiO_5; Ma et al., 2023b). Kaitianite ($Ti_2^{3+}Ti^{4+}O_5$) occurs rarely as oriented lamellae in grains of tistarite, suggesting oxidation during or prior to formation of the enclosing Ti-Al-Zr oxide (Supplementary Material, Fig. S-14). Unlike its parageneses in the Allende chondrite (Ma and Beckett, 2021) it is not associated with rutile. Griffinite is rare in *Crn-A* but common in *Crn-B* and *Crn-C*; in several occurrences it coexists with rutile and appears to form by the oxidation of carmeltazite. The incorporation of minor

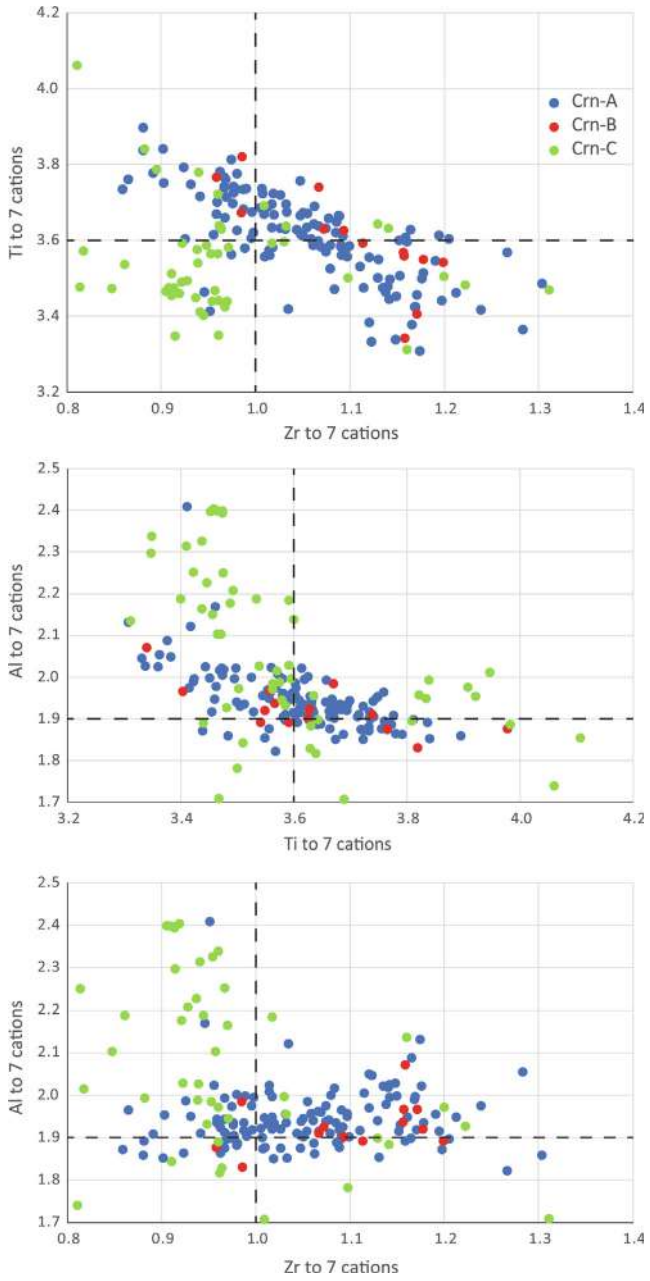

Fig. 18. Binary plots by paragenesis of major elements in the structural formulae of Ti-Al-Zr oxide phases (Ti-Al-Zr field in Fig. 17), normalized to 7 cations. Dashed lines mark the composition of type carmeltazite from *Crn-A*.

Ti^{3+} is equivalent to limited solid solution with sassite. Magnéliite ($(Ti^{3+}, Al)_2Ti_2^{4+}O_7$) is a rare phenocryst in glass in *Crn-B*.

Baddeleyite (monoclinic ZrO_2) is a common minor phase in all parageneses, and contains no detectable Ti, Al or Mg. However, ziroite ($(Zr,Ti)O_2$; Ma et al., 2024) may contain up to 10 at.% Ti and 5 at.% Al. Srilankite ($(Ti,Zr)O_2$) occurs together with griffinite and Zr-rutile in possible pseudomorphs after carmeltazite, an assemblage typical of *Crn-C*.

Ti-Al-Mg Oxides with Ca, Zr

Several unknown oxides representing combinations of Ti + Al + Mg ± Zr ± Ca (Supplementary Material, Table S-11) have been analyzed, mostly in *Crn-A* and *Crn-B* (Supplementary Material, Figs S-11b,c; S-12b; S-14) but some in *Crn-C*. Some occur as phenocrysts while others appear to be late-crystallizing or have ambiguous relationships to other phases.

Mg-Al spinels are mainly confined to paragenesis *Crn-A* and can be divided on inclusion types into 3 categories: pre-tistarite, post-tistarite and late (small, euhedral); sectioning effects may classify some post-tistarite spinels as pre-tistarite (Fig. 19, Supplementary Material, Table S-12). All the spinels are Fe-free non-stoichiometric Mg-Al-Ti oxides; Mg (as cations to 4O) ranges from 0.69 to 0.97, mean 0.79, while the sum of cations to 4O rarely reaches 3 and averages 2.89. Ti in spinel coexisting with tistarite can be expected to be mainly trivalent; Al is negatively correlated with (Ti + Mg), and Ti with Mg, both suggesting that Ti^{3+} substitutes for Mg in the tetrahedral site. Temperatures estimated using the MgO-Al_2O_3 phase diagram of Jung et al. (2004) range from 1200 to 1545 °C, with most estimates between 1285 and 1460 °C. Ti contents show a rough positive correlation with *T*. *In general*, pre-tistarite spinels (7/11) have *T* >1400 °C, post-tistarite spinels (8/12) have *T* ≤1400 °C and late spinels (7/11) record *T* ≤1375 °C. Non-stoichiometry is also correlated with *T*; the pre-tistarite spinels have the lowest number of cations. This may reflect the exsolution of abundant tiny unidentified Ti-rich phases in some of these spinels (Fig. 19a). Spinels that crystallized together with TiC from Fe-Ti silicide melts enclosed in Crn-A corundum (Fig. 19b) have compositions similar to pre-tistarite spinels.

Hibonite is common in all three corundum parageneses, but especially *Crn-B* and *Crn-C*. It typically has an intense blue colour, which may reflect high levels of Ti^{3+} (Beckett et al., 1988); this contrasts with the pale purple colour of the low-Ti hibonite (mean 290 ppm Ti; Griffin et al., 2019a) in the hibonite-grossite-V^0 xenoliths discussed above. The same colour has been observed in V-rich hibonite with almost no Ti and can be related to the presence of both V^{2+} and V^{3+} (Ardit et al., 2021). Fig. 20 and Table S-13 (Supplementary Material), show that *Crn-A* hibonite has the widest range of Ti and Al contents; *Crn-B* hibonite has Al contents in the lower end of the *Crn-A* range, while most *Crn-C* hibonites are grouped more tightly at the lower-Ti end of the *Crn-A* range. Mg contents are similar across the three parageneses, but *Crn-B* hibonite has generally lower Ca contents than *Crn-A* hibonite, while *Crn-C* hibonite has the highest Ca levels. The plot of Mg *vs* Ca shows a wide scatter for *Crn-A*, perhaps with a weak positive trend; however, data for *Crn-B* and *Crn-C* together define a broad negative trend. The hibonites from the *Crn-A* and *Crn-B* parageneses contain significant levels of Sr and REE (mean atomic (La + Ce + Nd) = 0.19 cations), while *Crn-C* hibonite has much lower levels of these elements. In *Crn-B* hibonite, Nd/Ce is typically >1, while the opposite is true in *Crn-A* hibonite; Nd is seldom above EDS detection limits in *Crn-C* hibonite. In *Crn-B*, the paragenetic position of hibonite can be taken by mizraite-(Ce) ($Ce(Al, Mg)_{11}O_{19}$; Ma et al., 2024), reflecting the high concentration of REE in the residual melts.

Hibonite compositions can be expressed as solid solutions of 3 components: CAH ($CaAl_{12}O_{19}$), MTH ($CaAl_{10}MgTiO_{19}$) and MSH ($CaAl_{10}MgSiO_{19}$), where MSH and MTH represent the substitution of $Mg^{2+}+(Ti,Si)^{4+} \rightarrow 2Al^{3+}$. We assume here that the REE substitute for Ca and require substitution of divalent elements for Al (REE^{3+}+ Mg → Ca + Al). A plot of Mg *vs* (Ti + Si) (Fig. 20) shows some points near the line corresponding to 1:1 substitution, but most analyses show a large excess of Ti and an overall positive correlation between Mg and (Ti + Si). Plots of Ti and (Ti + Si) *vs* Al show very strong negative correlations. When the excess Ti above that required by Mg substitution is added to the Al, the resulting sum matches the number of trivalent cations required to balance the 2 + cations. This is seen in Table S-13 where the number of 3 + cations required by the proportions of CAH, MTH and MSH components is identical within uncertainties to the sum of (3^+ cations + excess Ti). This suggests that the Ti excess is a rough measure (given the uncertainties in the EPMA analyses) of Ti^{3+}. If so, then Ti^{3+}/Ti ranges from 0 to 60 % (n = 75; Fig. 20) and has a mean

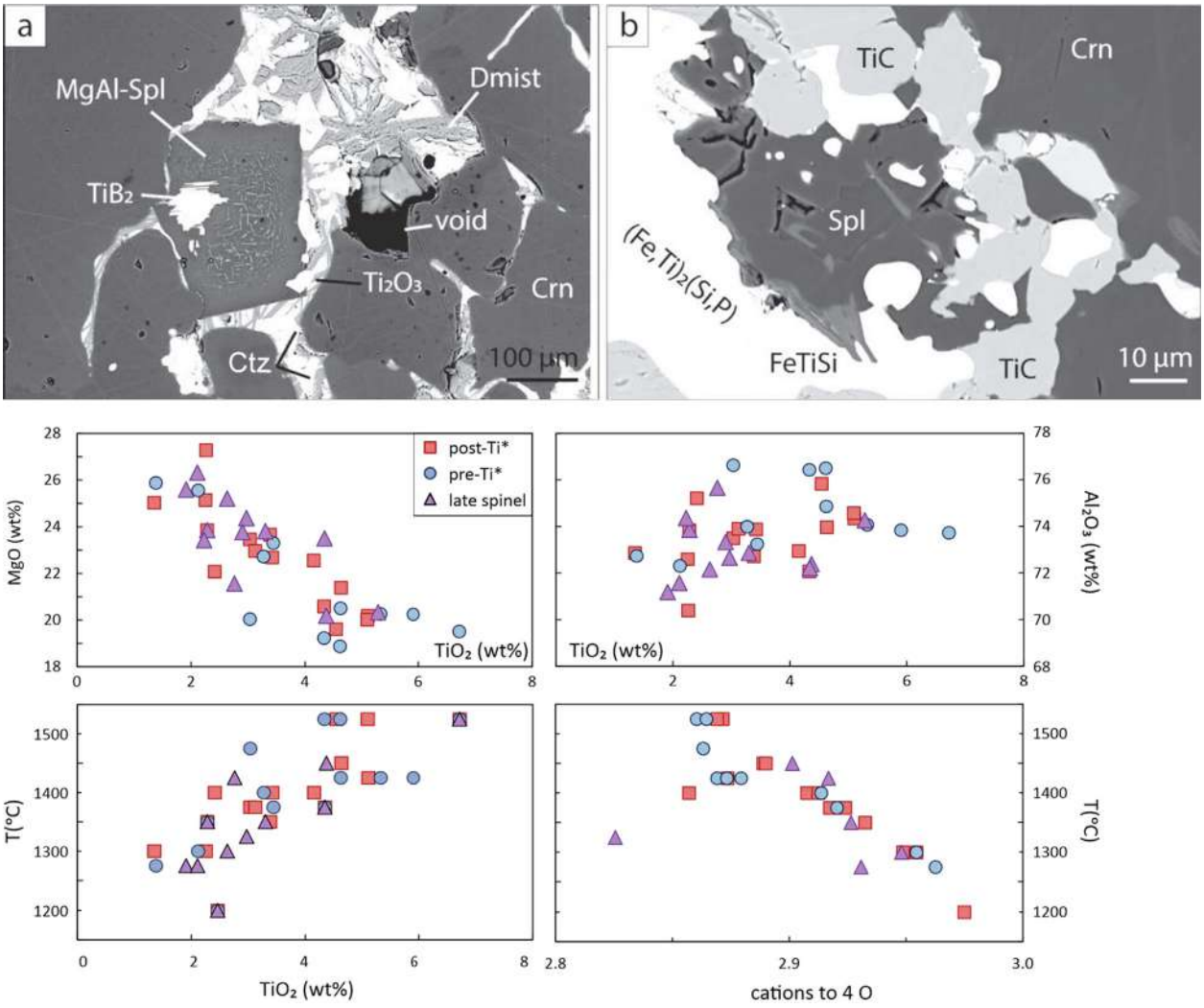

Fig. 19. Parageneses of spinels included in corundum. a, spinel (with exsolved Ti-rich phase) encloses lamellar TiB_2 and tistarite (Ti_2O_3), coexists with carmeltazite (Ctz) and is enclosed by quench crystals of dmisteinbergite. b, spinel is intergrown with Fe-Ti silicides and TiC. Below, bivariate plots of major elements in spinels divided by paragenesis (see text for explanation).

value of 33–37 % across all three parageneses. This is in the range of blue-hibonite analyses from refractory inclusions in carbonaceous chondrites (Beckett et al., 1988). Ti^{3+}/Ti rises with the number of Ti cations, but plateaus at *ca* 0.6 (Fig. 20) and the different parageneses appear to define subparallel distributions. The curve for *Crn-A* is the shallowest, while the steepest curve is dominated by *Crn-C* hibonite. A similar levelling-off of Ti^{3+}/Ti (or /Ti^{4+}) has been observed in synthetic hibonites under reducing conditions and may be related to reduction of all Ti^{4+} to Ti^{3+}on the five-fold site (Beckett et al., 1988).

Silicate Phases

Silicates are minor phases in the melt pockets and typically crystallize after most other phenocryst phases, as Si concentrations increase in residual melts. The most common are Mg-Ti-Al-Zr silicates which range from $MgTi_2(Al,Zr)_4(Si,Al)O_{12}$ in *Crn-B* to $Mg(Ti,Mg)_2(Al,Mg)_4(Si,Al)O_{12}$ in *Crn-A*; they may comprise a solid-solution series with two more silica-rich variants $Mg(Al,Ti)_2Si_4O_{12}$ (phases 3 and 4 in Supplementary Data, Table SD-14). The most common Ca-Al silicate in *Crn-A* melt pockets has the nominal formula $(Ca,Mg)_3(Al,Ti^{3+},Zr,Mg)_5(Si,Al)_4O_{18}$; a similar phase in *Crn-B* pockets has higher Al and Ti, while in *Crn-C* pockets it has higher Mg and Si. A rare aluminosilicate can be expressed as $(Al,Ti^{3+})_6(Si,Ti^{4+})_2O_{13}$. A rare Zr-rich silicate (expressed as $Zr_2(Ti^{3+},Al)_2SiO_9$) occurs with hibonite in both *Crn-A* and *Crn-B* melt pockets. Sapphirine ($(Mg,Al)_8(Al,Si)_6O_{20}$) has been observed in association with tistarite, kaitianite, and the unknown phase $MgTi_2^{3+}Al_4SiO_{12}$ in one sample (Ma et al., 2023a).

Sulfides

Sulfides are trace phases in melt pockets in the *Crn-A* paragenesis, and very rarely in the *Crn-B* paragenesis. The most common is TiS, which typically forms long blades either intergrown with oxide and silicate phenocrysts (Supplementary Material, Table S-15; Fig. S-16), isolated crystals in glass, or emulsions of TiS spherules dispersed in glass. TEM-EDX analyses of one example of TiS fits the hexagonal structure $P6_3mc$; this distinguishes it from wassonite (TiS), which is rhombohedral (Nakamura-Messenger et al., 2012). However, EBSD analyses of other TiS phases confirm that they are wassonite. It commonly is associated with MnS (alabandite), which typically forms cuboid to spheroidal grains (Supplementary Material, Fig. S-16b). Wassonite contains 0.5 wt% Mn on average, while alabandite takes up considerable amounts of Ti, Cr, Fe and Mg. Other less-common sulfides have compositions corresponding to (Cr,Mn)S, (Ti,Ce)S and (Mn,Ti)S. The petrography of the sulfides suggests that they have crystallized very late, possibly during ascent of the corundum xenoliths in the melt column.

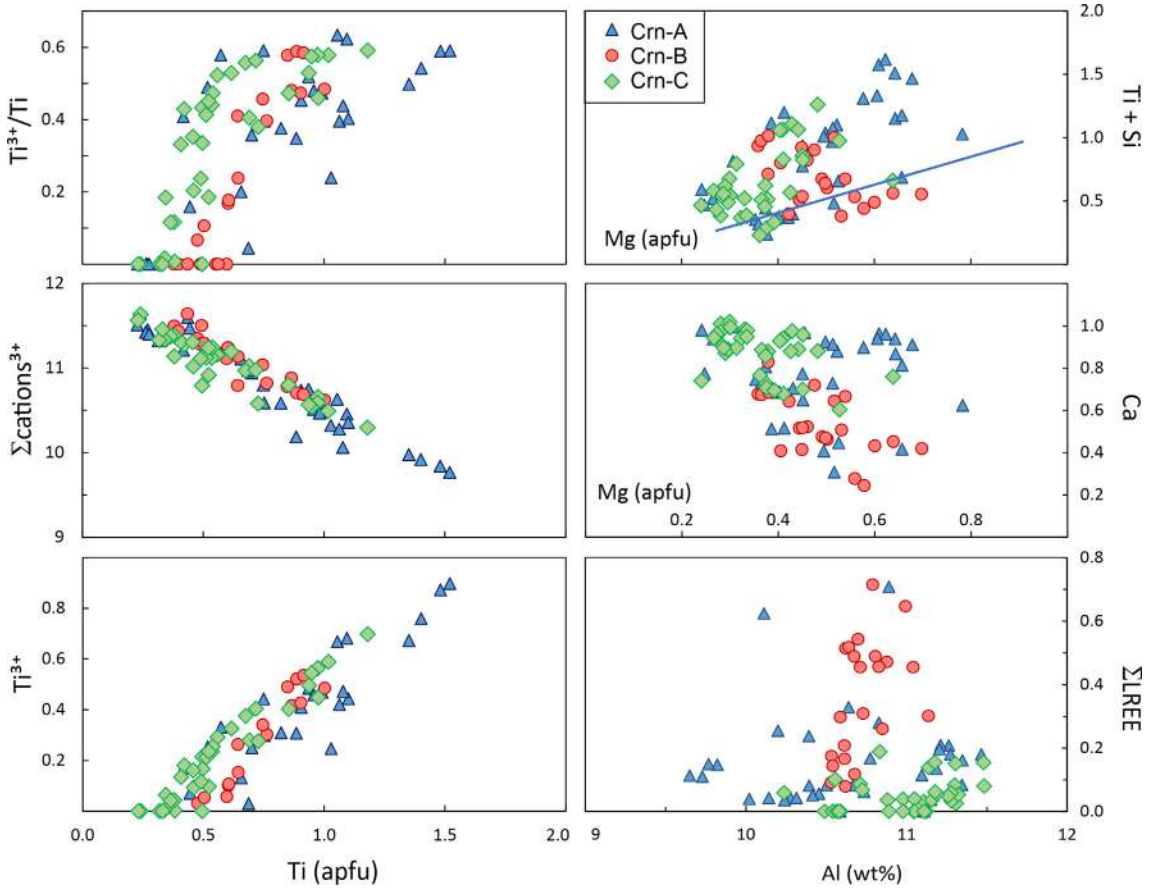

Fig. 20. Bivariate plots of hibonite compositions by paragenesis. The blue line in upper right represents 1:1 substitution of Mg *vs* (Ti + Si); points falling above the line probably contain significant Ti^{3+}.

Quench phases

The glasses in the melt pockets of the *Crn-A* paragenesis, in particular, commonly show randomly oriented blades with the chemical composition of anorthite (Fig. 19a, Supplementary Material, Fig. S-8d; Table S-16). Raman spectra show that these are the hexagonal polymorph dmisteinbergite, first reported from burning coal dumps, where it crystallizes from extremely reducing gasses at *ca* 1000 °C (Zolotarev et al., 2019). In the Mt Carmel samples, it appears to represent a quench phase, probably formed during the explosive eruption and rapid cooling of the xenolith-bearing magmas.

An Fe-free, highly aluminous Ti-rich clinopyroxene, also apparently a quench phase, typically has nucleated on other silicates as triangular to elongate porous crystals, and at the contact between Fe^0 spheres and Ca-Al glasses in *Crn-A* melt pockets. It is similar to the grossmanite ($CaTi^{3+}SiAlO_6$; Ma and Rossman, 2009) found in carbonaceous chondrites and comets (Table S-16), with 26 wt% Al_2O_3 and *ca* 12 wt% Ti_2O_3, and high LREE contents but with significant Zr in the M1 site. Terrestrial grossmanite was first reported as inclusions in high-Ti corundum from the Karpinska-1 kimberlite (Arkangelsk field, Russia; Yatsenko et al., 2021b).

Several REE-rich phases occur in quench-type textures (Supplementary Material, Fig S-11a, b; Fig. S-12d; Table S-17). Zirkelite is the most common, followed by a Fe,Nb-free equivalent of nöggerathite-(Ce) ($(Ce,Ca)_2Zr_2(Nb,Ti)(Ti,Nb)_2Fe^{2+}O_{14}$, a zirconolite-group mineral), a Nb equivalent of belyankinite ($Ca_{1-2}(Ti,Zr,Nb)_5O_{12}\cdot 9H_2O$) and Al-rich perrierite-(Ce). The presence of these phases emphasises the strong enrichment of the trapped melts in REE and Zr, at low a_{SiO2}. Baddeleyite (ZrO_2) is a rare quench phase in melt-pocket glasses but is common as skeletal crystals in the glass rims on xenoliths of the corundum aggregates. Zircon appears to be a quench phase in some melt pockets, where it forms spherical aggregates up to 30 μm across, composed of tiny euhedral to subhedral crystals together with euhedral crystals of mullite, in a glass matrix. Similar balls up to 1 mm in diameter have been found in heavy-mineral concentrates.

4.6.4. Metallic melts and moissanite

The metallic melts have been described in detail by Griffin et al. (2022); here we give a brief summary, including new phases identified more recently.

Microstructural evidence (Supplementary Material, Fig. S-17) indicates that immiscible carbon-rich metallic (Fe-Ti-Zr-(Si,P)) melts separated from the silicate melts of the *Crn-A* and *Crn-B* parageneses early in their evolution; in some cases tistarite overgrows spheroids of silicide melt. These silicide-melt inclusions are most abundant in *Crn-A*, and rare in *Crn-C*. Reconstructed compositions of individual complex silicide inclusions (Griffin et al., 2022) fall close to cotectic curves in the Fe-Ti-Si system (Weitzer et al., 2008), consistent with their trapping as metallic liquids. The further evolution of the silicide melts was driven by crystallization of two main ternary phases (FeTiSi and $FeTiSi_2$) and several near-binary phases, as well as the separation of later immiscible melts, many enriched in P and Zr (Griffin et al., 2016, 2022). Temperatures estimated by comparison with experimental work range from ≥1500 °C to *ca* 1150 °C; these probably are maximum values, since the solution of C, P, Zr and especially H_2 would lower the crystallization *T* of the melts. With decreasing *T*, the Si, Fe and P contents of the Fe-Ti-Si melts increase, while contents of Ti and C decrease.

Recently reported phases from parageneses *Crn-B* (Ma et al., 2024) include $(Ti,Fe,Mn)_6Si_5$, $CrSi_2$, and toledoite (TiFeSi; also found in *Crn-A*). Others from *Crn-C* are yeite (TiSi) and wenjite (Ti_5Si_3), while the parageneses of oreillyite (Cr_2N; Bindi et al., 2020) and FeTiP are ambiguous.

Some silicide melts have crystallized Mg-Al spinel (Fig. 19), jingsuite (TiB_2; Supplementary Material, Fig. S-18a; Griffin et al., 2020a; Xiong et al., 2022) khamrabaevite (TiC; Fig. S-17) and moissanite (SiC). Melt-inclusion studies (Huang et al., 2020) show that most SiC has crystallized from immiscible silicon (Si^0) melts, but SiC crystals include several phases that also occur in the Fe-Ti silicide melts, suggesting that immiscible Si^0- and Fe-Ti silicide melts coexisted. Volatiles released upon crushing of acid-leached SiC grains are dominated (75 wt%) by H_2, suggesting the presence of a third immiscible phase during crystallization (Huang et al., 2020). *In situ* (SIMS) isotopic analyses of carbon define two main populations ($\delta^{13}C$ = -30 to –32 ‰, $\delta^{13}C$ = -25 to −28 ‰). The latter population is similar to SiC from kimberlites and from ophiolites in the Tethyan and Central Asian orogenic belts (Shiryaev et al., 2011; Huang et al., 2020).

4.6.5. Ti-oxynitrides in Crn-A

Ti oxynitrides (Ti(N,O,C)) are abundant in the *Crn-A* aggregates (Griffin et al., 2021a). They appear in a remarkable array of morphologies (Supplementary Material, Fig. S-18): cuboid crystals included in tistarite; small isolated globular to cruciform inclusions in corundum; irregular blobs, drop-shaped lenses and cruciform inclusions in silicate melts; long arrays or lattice patterns apparently controlled by orthogonal voids in the skeletal structure of corundum aggregates; and irregular bodies interstitial to corundum crystals. Some nitrides appear to be crystals on the rims of balls of Fe-Ti silicide melts, often together with TiB_2 (Griffin et al., 2020a) and/or TiC (Griffin et al., 2022); microstructures suggest that others were immiscible with Fe-Ti-silicide melts (Supplementary Material, Fig. S-18b). EELS spectra (Supplementary Material, Fig. S-15) indicate that Ti is divalent in analyzed Ti-nitrides and in coexisting TiC.

The TiN phase shows a wide range of solid solution (Griffin et al., 2021a; Supplementary Material, Fig. S-19), taking up 0–10 wt% carbon and 1.7–17 wt% oxygen. TEM analysis confirms that the nitrides have crystallized in the halite (*fcc*) structure. Nitrides coexisting with silicide melts have higher C/O than those coexisting with silicate melts. Analyses with no carbon fall along the TiN-TiO join in Ti-N-O phase space (Fig. S-19), implying that their Ti is a mixture of Ti^{3+} and Ti^{2+}, while those with 1–3 at.% C appear to be solid solutions between TiN and $Ti_{0.75}O$. Analyses with >10 at. % C have higher Ti^{2+}/Ti^{3+}, suggesting lower fO_2. The implied fO_2 across this range of compositions is ≈ΔIW −6 to −8.

4.6.6. Oxygen fugacity: Variation with paragenesis

The three corundum-aggregate parageneses display gradational differences in fO_2. *Crn-A* is dominated by minerals containing Ti as Ti^{3+} (tistarite, carmeltazite, hibonite), Ti^{2+} (TiC, Ti(N,O), TiB_2) and Ti^0 (various Fe-Ti-Zr-Si alloys); spinels commonly show extensive substitution of Ti^{3+} for Mg. Tistarite also occurs in *Crn-B*, and the high levels of Ti in corundum of *Crn-B* require Ti^{3+} substitution, but this paragenesis also contains several phases with both Ti^{3+} and Ti^{4+} (sassite, magnéliite, hibonite, kaitianite) or only Ti^{4+} (griffinite, rutile). TiC and Ti(N,O) are rare. Fine-grained intergrowths of griffinite with rutile and ziroite suggest late oxidative breakdown of carmeltazite. In *Crn-C*, corundum has very low levels of Ti and hibonite appears to contain only Ti^{4+}; griffinite is a common phase in interstitial pockets. The *Crn-C* aggregates do not contain metal-alloy inclusions. It is clear that fO_2 decreases from *Crn-C* to *Crn-B* to *Crn-A*.

4.6.7. Trapped gasses

Several attempts were made at IGG-CAS (Beijing) to analyze the noble gasses in *Crn-A* corundum. Only one was successful, yielding $^3He/^4He(Ra)$ = 8.1 ± 0.2 (^4He = 8 E-7 cc STP), indicative of a mantle derivation (H. He, *pers. comm.*).

Four 2–3 mm grains of the hibonite-grossite-V^0 aggregates and four *Crn-A* corundum aggregates were analysed for H, C, N, and S contents by ignition in an O_2-He atmosphere at *ca* 1150 °C, followed by chromatographic analysis (Griffin et al., 2020b; see Supplementary Material III and Table S-18). The hibonite samples contain concentrations of gas 4–5 times higher than the corundum aggregates, even though the latter have much more void space than the hibonite crystals (Supplementary Material, Fig. S-9). However, in both cases the included fluids comprise > 95 at.% hydrogen. Carbon is the second most abundant element, as expected from the common occurrence of carbide minerals in the aggregates and amorphous carbon in the breccia xenoliths (Fig. S-20).

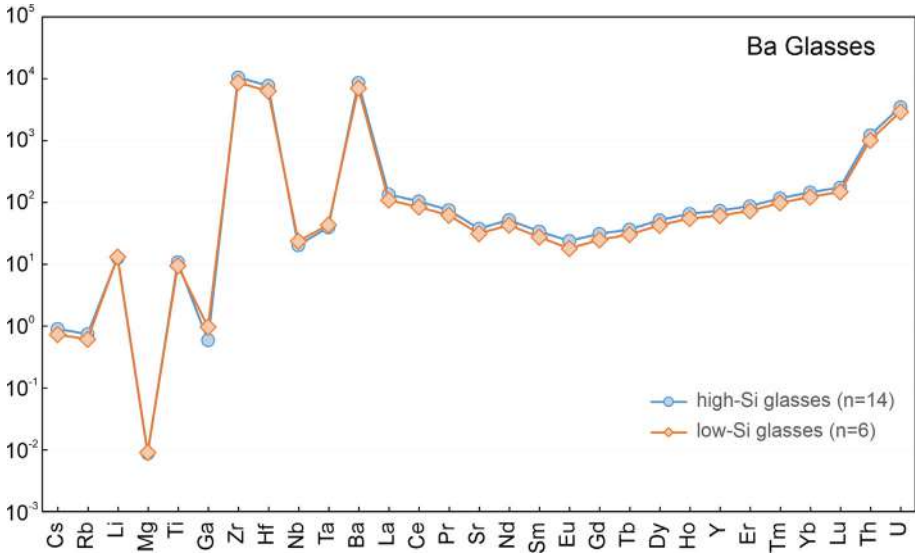

Fig. 21. Trace-element distribution in glass rims on corundum-aggregate xenoliths.

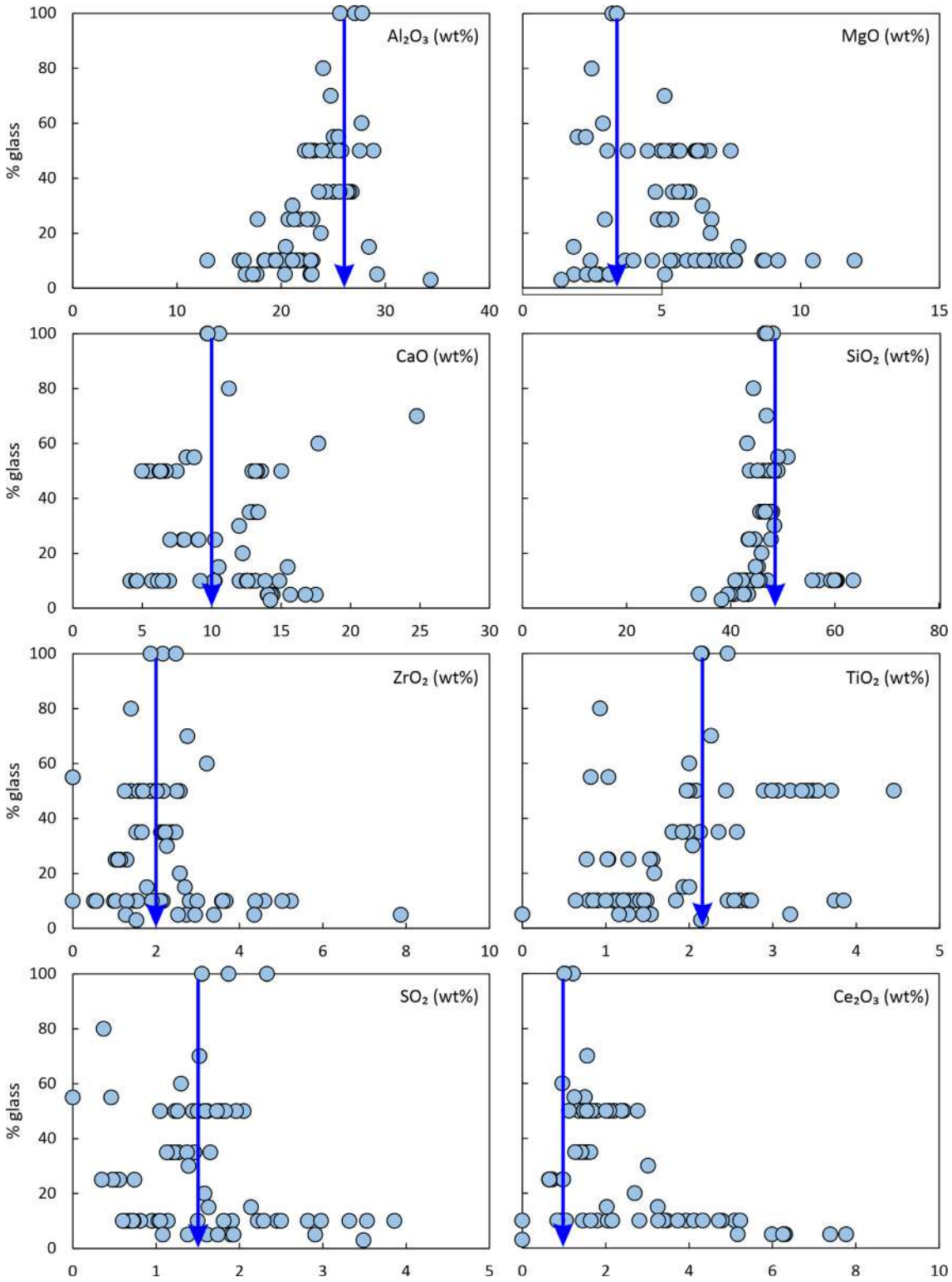

Fig. 22. Estimating the composition of primary trapped melts in *Crn-A* aggregates; see text for explanation.

4.7. Eruption-related breccias and silicate melts

Some larger fragments of corundum aggregates are breccias, with angular clasts of the corundum aggregate (dominantly *Crn-C*) embedded in a matrix composed dominantly of carbon (Fig. S-20). TEM, EBSD and Raman analyses indicate that the carbon is amorphous. TEM images show corundum grains and melt pockets cut by parallel-sided veins of vesicular amorphous carbon from several tens of microns to $\leq$ 50 nm thick.

In the breccias the carbon is mixed with angular, rotated fragments of corundum, SiC and sulfides (FeS, FeS_2, ZnS). Fluorine resides in abundant fluorite, a cryolite-like phase (possibly $Na_3AlF_4(OH)_2$) and an unknown K-Al fluoride (possibly $KAlF_2(OH)_2$); chlorine is concentrated in NaCl and KCl. The microstructures

and the amorphous nature of the carbon suggest that these veins reflect brittle fracture and turbulent mixing during injection of carbon-rich fluids with high levels of sulfur, chlorine and fluorine. These processes may be linked to the eruption of the host magma,

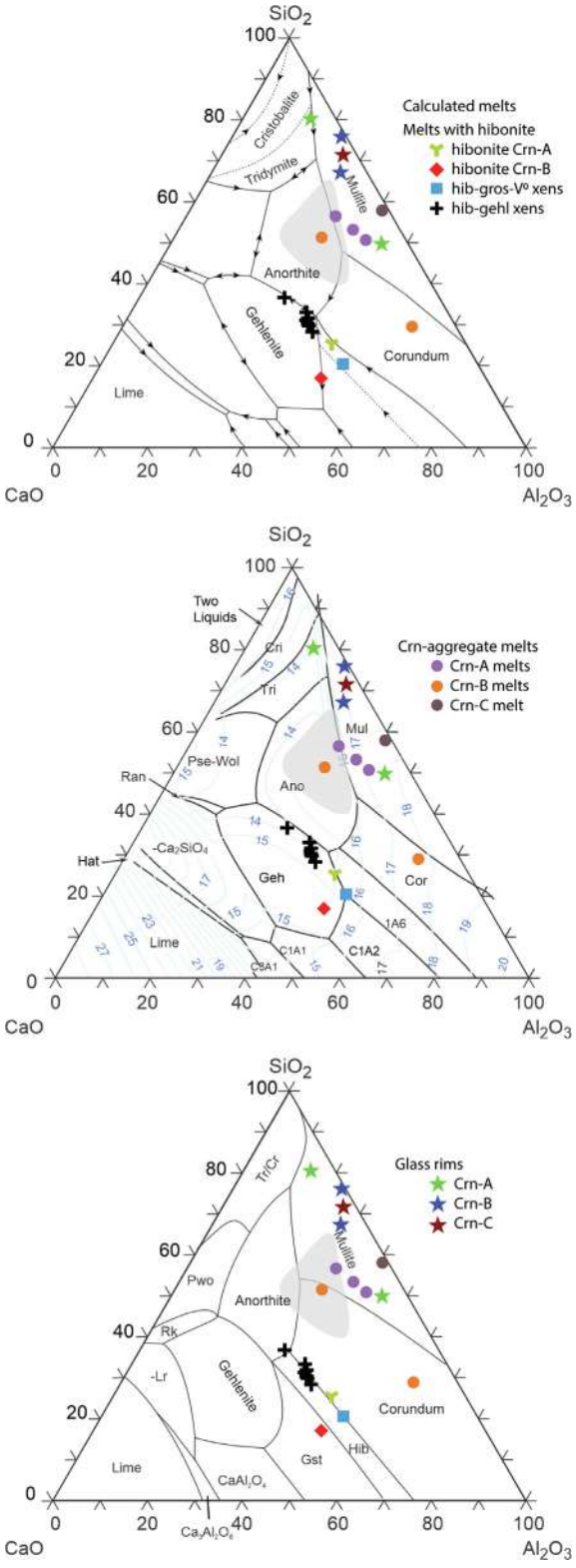

Fig. 23. Phase diagrams of the CaO-Al_2O_3-SiO_2 system. 1 atm. a, FactSage; b, Mao et al., 2006; c, Ottonello et al. (2013). a and b are from experimental data; c is from thermodynamic modelling. Grey field covers analyses of trapped glasses in Crn-A and B.

but many of the melt-pocket glasses in the corundum aggregates are also high in sulfur (Supplementary Material, Table S-9), suggesting that the volatiles are part of the corundum-aggregate system. TIMS analyses of the matrices of four samples give $\delta^{13}C$ between −19 and −21.7 ‰ (*vs* PDB; mean −20.5 ± 1.4 ‰ (1σ)).

Many rounded fragments of the corundum aggregates (mainly *Crn-A*) have thick rims of glass with fluidal textures; these glasses contain quench crystals of baddeleyite (Supplementary Material, Fig. S-21) and abundant resorbed zircon or aggregates of tiny euhedral zircon grains. There are two intermixed, apparently immiscible, glasses: high-Si/low-Al and low-Si/high-Al. High levels of BaO (3.7–3.8 wt%,) and Ca≈Na≫K (Supplementary Material, Table S-19) distinguish them from the melts trapped in the corundum aggregates, and the glasses of the volcanic ejecta (Supplementary Material, Tables S-1, 9).

The fine-scale mixing of the high- and low-Si glasses prevented separate LA-ICPMS analyses. The "bulk" compositions of glass rims on *Crn-A* aggregates, dominated by the low-Si component, have a V-shaped REE pattern with the minimum at Eu and a modest negative Sr anomaly (Fig. 21). Like the melt-pocket glasses, they show high levels of Zr, Hf, U and Th, but low Ti contents.

Crn-B aggregates may be rimmed by either a high-K glass or a Ba, Ca, Na-rich glass similar to those rimming *Crn-A* aggregates (Table S-19). Glass rims on Crn-C aggregates are low in Ba, but otherwise intermediate in composition between the two populations of glasses on *Crn-B* fragments.

4.8. Parental melts

The compositions of most melt pockets in the corundum aggregates have been strongly modified by the post-entrapment crystallisation of corundum, phenocryst phases and quench phases. The composition of the least-modified trapped melts can be estimated from plots of % oxide *vs* % glass in individual pockets (Fig. 22). The volumes of glass can only be approximations, due to 2D sectioning effects, but with enough analyses, clear trends are observed. In these plots, a decrease in wt% oxide with decreasing % glass reflects the removal of that oxide (e.g. Al_2O_3) in a major crystallizing phase, while an increase in wt% oxide with decreasing glass content (e.g. Na_2O) shows that the element was incompatible in the crystallizing solids. The composition of this "first trapped" melt in the *Crn-A* paragenesis (Fig. 22; Supplementary Material, Table S-20) is low in SiO_2 (48 wt%) and Fe-free but with high Al_2O_3 and %-level contents of LREE, Zr, Ti, Mg and S.

To derive the composition of the "parental melt" from which the *Crn-A* aggregates began to crystallize, a significant amount of Al_2O_3 would have to be added to the "first-trapped" melt, equivalent at least to the last part of the zoned profiles (Fig. 12), which crystallized after the system was partially to completely closed (Oliveira et al., 2021). Addition of 20–35 % of corundum gives a rough estimate for the "parental melt" of *Crn-A* (Table S-20) that is high in Al_2O_3 and CaO, with low SiO_2; K_2O and MgO are the other major oxides. For a relatively low-SiO_2 melt, it is markedly enriched in Zr, Ti, LREE and S. However, this composition would represent a relatively late-stage melt from which an unknown proportion of immiscible oxide and silicide melt(s) had already separated.

Melt pockets with large rods of an Al-bearing sassite in glass (Supplementary Material, Fig. S-11a) have been used to reconstruct one "parental" melt in a sample of the *Crn-B* paragenesis. An overview of this xenolith (Supplementary Material, Fig. S-22) shows that the melt pockets represent the concentration of a residual melt within a compacting corundum cumulate, and the sassite thus is a late-crystallizing phase. The *reconstructed* melt is very high in Ti and Al, and low in Ca and Mg, but the *residual* melt (the glass) is similar to many trapped melts in both the *Crn-B*

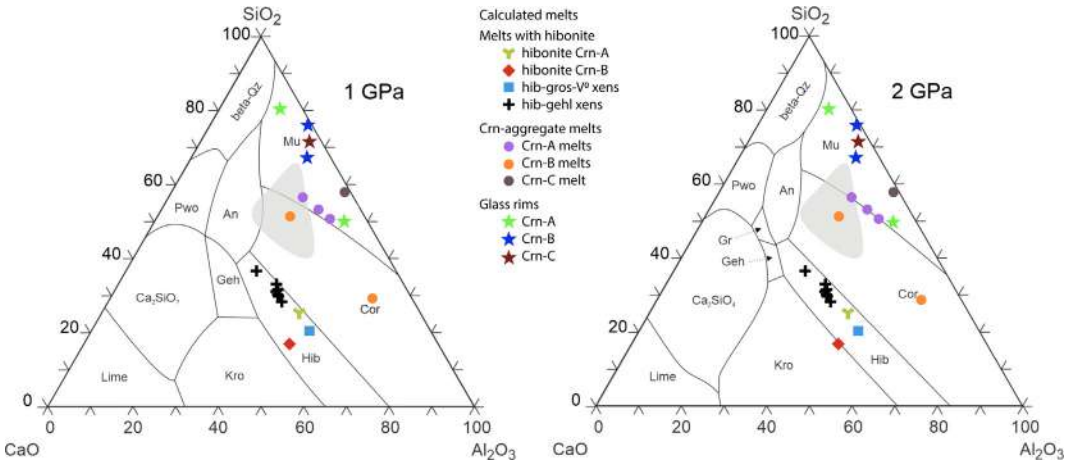

Fig. 24. Modelled CAS phase diagrams at 1 and 2 GPa (Ottonello et al., 2013). Grey field covers analyses of trapped glasses in Crn-A and B.

and *Crn-A* aggregates. The compositions of earlier-stage *Crn-B* melts have also been calculated from the composition of hibonite crystals (n = 24) in melt pockets. The average of these estimates (Supplementary Material, Table S-20) also has low SiO_2, but much higher CaO than the reconstructed late-stage melt.

The melt composition calculated from hibonites in the *Crn-C* paragenesis is higher in Si, Ti and Zr than the corresponding Crn-B melt, but lower in Ca. The melt compositions calculated for the coarse-grained hibonite + grossite ± vanadium xenoliths are even lower in SiO_2 and higher in Al_2O_3 and CaO.

In a cumulate of Cr-rich corundum, Fe-Ni alloys and Fe-Mg-Al spinels, barred intergrowths of these phases are strongly suggestive of eutectic crystallisation (Supplementary Material, Fig. S-6). An areal EDS analysis of these intergrowths (Supplementary Material, Table S-20) is dominated by Al_2O_3 and Cr_2O_3, with lesser amounts of FeO and MgO and only 2 wt% SiO_2. This may represent the composition of a metal-oxide melt. Similarly, the reconstructed parental melts of the Cr-corundum + spinel cumulates are Al-Cr-Fe-Mg oxides with *ca* 2 wt% SiO_2.

The compositions of melts that coexisted with the hibonite-gehlenite-anorthite-corundum cumulates (Fig. 11; Table S-20) have been calculated from hibonite, gehlenite, anorthite and spinel, using the crystal/melt distribution coefficients of Beckett and Stolper (1994), as modified by Griffin et al. (2019a). In most cases the contents of SiO_2 estimated from hibonite are lower by 5–10 wt % than those calculated from gehlenite and anorthite, and the latter were adopted. The estimates for other elements represent means of the values obtained from the other phases, which typically show little scatter; FeO could only be calculated from hibonite. These are all Ca-Al-Si melts with 2–5 wt% TiO_2. An areal EDS analysis of the mesostasis in one hibonite-gehlenite-anorthite cumulate (Figs. 23, 24) is similar in terms of CaO, but has higher SiO_2, TiO_2 and lower Al_2O_3, suggesting that the xenoliths are indeed cumulates and do not represent the crystallization of a eutectic melt.

4.9. Radiometric dating

U-Pb dating of carmeltazite, which can contain high levels of U and Th, was carried out using LA-ICPMS. This analysis is complicated by the occurrence of carmeltazite as small (typically $\leq$ 20 μm) phenocrysts in the melts (now glass) trapped in cavities in the corundum. The relatively high Pb contents of the melts, combined with the small size of the target grains, means that most analyses are mixtures of common Pb and radiogenic Pb. We have approached this problem by projecting from a young common Pb composition ($^{207}Pb/^{206}Pb$ = 1.106) to construct mixing lines, whose intersection with Concordia is taken as the corrected age (see Supplementary Material II). Analyses of 21 of the largest available carmeltazites are shown in Supplementary Material Table S-21. In some corundum grains carmeltazite could be analyzed in two melt pockets, giving a total of 13 estimated ages, of which nine represent 3-point mixing lines.

Nine of the 13 ages range from 1.6 to 4.6 Ma, i.e. Pliocene (2.6–5.3 Ma) to lower Pleistocene. Two ages are mid-Miocene (10 and 14 Ma). This group is supported by an estimated age of 13 ± 2 Ma (EMPA dating; Supplementary Material II) on a U-rich thorianite [$(Th,U)O_2$] coexisting with ziroite (ZrO_2), mizraite-(Ce) [$Ce(Al_{11}Mg)O_{19}$] and Ti-sulfide in a melt inclusion in a Carmel Sapphire (Sample 198, *Crn-B*) from surface alluvium near outcrops of the Cover Basalt at Migdal ha-Emeq (Supplementary Material, Fig. S-1).

One U-Pb age of 27 ± 2 Ma (upper Oligocene) and one of 225 ± 10 Ma (mid-Triassic) are accompanied by a TEM U-Pb analysis of an alloy phase $(Zr,U,Ti)_2(P,Si)$ (U = 23.4 wt%; Pb = 1.09 wt%; Griffin et al., 2022) in a corundum grain from alluvium (1130; Crn-B paragenesis) in the Yoqneam Valley. The calculated bulk U-Pb age is 323 ± 50 Ma (Upper Carboniferous); the presumed presence of minor Th would lead to a slightly younger age. This is within the age range identified in mantle-derived zircons from the Rakefet Magmatic Complex (Griffin et al., 2018b).

5. Discussion

The mineral assemblages and corundum aggregates described here show widely variable textural development, from unequilibrated skeletal growth (*Crn-A*) to cumulates (*Crn-B, C*), and evidence for > 1 primary melt composition as well as a wide range in oxygen fugacity. Individual samples are interpreted as fragments of individual subsystems, sampled by explosive eruptions at different stages of their magmatic evolution. To organize this mass of observations, we will discuss them as if they represent a single magmatic system.

We first attempt to define the geological setting and environmental conditions in which these melts evolved; we then discuss the implications of observed melt-melt and melt-fluid immiscibility for the origins of the melts themselves. Finally, we present a model of an idealized Mt Carmel magmatic system and discuss the broader implications of this model.

5.1. Crystallization environment

5.1.1. Volcanic sources

The age spectrum of carmeltazite from paleo-placer samples is similar to that of the zircons from the paleoplacer deposits (Griffin

et al., 2018), which shows major peaks at 3–4 Ma (Cover basalt) and 9–15 Ma (Lower Basalt) with a gap from 6 to 9 Ma, and a smaller peak at 28 Ma. The 10–14 Ma carmeltazite U-Pb ages correspond to the timing of the Lower Basalt, while the 1.6–4.6 Ma ages overlap the eruption of the Pliocene Cover Basalt but extend to younger ages. The youngest ages (<3 Ma) may reflect derivation from Pleistocene volcanism north of the study area. However, no zircons younger than 3.5 Ma have been found in the paleoplacers to date, and selection of a slightly more radiogenic common-Pb composition would move these analyses to slightly older ages, within the Pliocene. Most of the Plio-Pleistocene ages are from the Crn-A parageneses, while older ages are from Crn-B or Crn-C samples. This may reflect both the fragility of Crn-A during transport from the more distant Cretaceous vents, and an overall larger contribution of material from the nearby Miocene-Pliocene volcanics.

All three corundum-aggregate parageneses are found in both the Cretaceous tuffs and the Plio-Pleistocene paleoplacers. However, in the alluvial deposits the abundance of *Crn-A* is much higher relative to *Crn-B* and *Crn-C* than in the tuffs. This distribution, and the radiogenic ages noted above, suggest that the Miocene-Pliocene volcanism in the Yizre'el Valley has sampled younger SUR parageneses similar to those found in the Cretaceous volcanic centers on Mt Carmel. This would be consistent with the occurrence of corundum, moissanite and the basalt-megacryst suite in alluvial samples taken near outcrops of the younger basalts (Wald and Toledo, 2016; Supplementary Material, Fig. S-1). Over large areas between the Dead Sea and Mt Carmel, units of the Middle and Upper Judea Group, coeval with the Cretaceous volcanics on Mt Carmel, are overlain by the Cover Basalts (Kafri, 2002; Rozenbaum et al., 2016). It thus is possible that these younger basalts also sampled buried Cretaceous pyroclastics, similar to those on Mt Carmel.

The Lower Basalts on the divide between the Yizre'el valley and the Jordan Valley drained westward into the proto-Kishon river until relatively late in the uplift history, when streams flowing into the deepening Dead Sea Rift captured the upper reaches. Volcanism continued into the Pleistocene in the Golan Heights and northern Galilee, just outside the Yizre'el Valley; these younger basalts also probably drained southward until the present geomorphology began to develop after the Pliocene volcanism (Kafri, 2002; Matmon et al., 2003). All of these basalts thus may have contributed alluvium to the proto-Kishon valley.

Most of the Cretaceous volcanic centers on Mt Carmel have been draining to the west since uplift and tilting of the block began in the late Miocene, and probably have contributed little to the placers in the proto-Kishon River. The exceptions are the Rakefet Magmatic Complex, which drains into the Yoqneam River, a tributary of the Kishon, and the Muhraka outcrops (Supplementary Material, Fig. S-1).

5.1.2. A thin lithosphere and a basaltic underplate

Apter (2014) proposed a conductive geotherm (45 mW/m^2) for the upper mantle beneath Mt Carmel, based on single-clinopyroxene thermobarometry. Lu et al., (2022, references therein) used a suite of garnet-websterite and two-pyroxene + garnet granulite xenoliths to construct a more detailed picture, with an elevated advective geotherm typical of alkali-basalt fields worldwide (O'Reilly and Griffin, 1985). Peridotitic garnet xenocrysts from the Cretaceous volcanics and the alluvial deposits are limited to low-Cr types (Cr_2O_3 = 1–2 wt%) typical of low-*P* fertile garnet lherzolites with "asthenospheric" compositions (Lu et al., 2022). No garnet-peridotite xenoliths have been recovered from the tuffs and there is thus no evidence for a thick, depleted lithosphere in Cretaceous time. The xenolith data thus indicate a thin (<90 km), hot lithospheric mantle. However, the heat flow across the area (Moshen et al., 2006) is lower than would be expected above such a thin lithosphere, or from the xenolith-based geotherm. This discrepancy suggests that the lithosphere has been further thinned relatively recently and that the associated heat pulse has not yet reached the surface.

Geophysical surveys show that the area has a thin continental crust, with a Moho at 26–27 km (Hofstetter and Bock, 2004; Koulakov and Sobolev, 2006; Segev and Rybakov, 2011). *Vp* and *Vs* from the stations nearest to Mt Carmel suggest a mafic lower crust with SiO_2 = 45–53 wt% (Hofstetter et al., 2000; Hofstetter and Bock, 2004; Li et al., 2021). Receiver-function analyses at stations in northern Israel show unusually low sub-Moho *Vs* (4.3–4.4 km/sec; Hofstetter and Bock, 2004) and the station closest to Mt Carmel (MRNI) shows a gradual increase in *Vs* with depth from the Moho to a maximum of 4.7 km/sec at depths of 60–70 km. The underlying low-velocity zone is taken as the lithosphere-asthenosphere boundary (LAB); it rises from ca 80 km in northern Israel to 67 km near the Red Sea (Moshen et al., 2006). This combination of a mafic lower crust and a gradient in *Vs* with depth suggests a thick mafic underplate and a gradual crust/mantle transition beneath Mt Carmel (*cf.* Griffin and O'Reilly, 1987). This underplating is further recorded in the chemistry of the Miocene basalts of the area. The basalts of the Yisre'el Valley are basanites and nephelinites, derived from a mantle with a high proportion of pyroxenites, while basalts from areas to the E and SE are alkali basalts with a dominantly peridotitic source (Weinstein, 2000).

5.1.3. Pressure estimates

Some constraints on the crystallization pressures of the different parageneses can be derived by comparing the compositions of the trapped and reconstructed melts with experimental data and thermodynamic modelling on the CaO-Al_2O_3-SiO_2 (CAS) system, which comprises > 90 % of most of these melts. One-atmosphere experimental data are available (Fig. 23a, b; Mao et al., 2006) and Ottonello et al. (2013) have modelled the topology of the CAS system at 1 atm. (Fig. 23c), 1 GPa and 2 GPa (Fig. 24).

On experimentally-determined 1-atm. phase diagrams (Fig. 23a,b) nearly all of the trapped melts in the *Crn-A,B* parageneses plot in the liquidus field of anorthite. However, plagioclase is not a liquidus phase in these melts. Furthermore, the calculated parental melts for the *Crn-A* paragenesis fall in the liquidus field of mullite, rather than that of corundum, the observed liquidus phase. In the modelled 1-atm. phase diagram (Fig. 23c) the anorthite field is smaller, and both trapped and parental melts straddle the mullite-corundum cotectic.

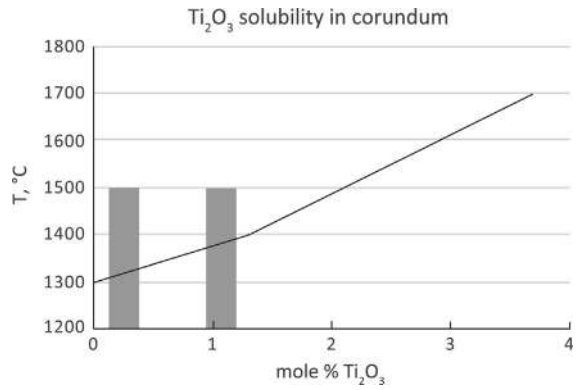

Fig. 25. Solubility of Ti_2O_3 in corundum *vs* temperature (after Yasuda et al., 1998). Vertical bars show mean values of Ti_2O_3 in the low-Ti cores of corundum in a typical Crn-A aggregate, and the high-Ti unzoned cores typical of Crn-B corundum. See text for further explanation.

At 1 GPa (Fig. 24a) some of these issues are resolved. The trapped melts no longer fall in the An field; this is consistent with the incongruent melting of anorthite to Crn + Liq at P > 0.9 Gpa (Goldsmith, 1980). Some of the *Crn-A, B trapped* melts (and the mean of 6 *Crn-C* melts) still fall in the liquidus field of mullite, but all of the *Crn-A, B reconstructed* melts fall in the liquidus field of corundum. In the modelled system at 2 Gpa (Fig. 24b) these relationships do not change substantially. It therefore seems likely that the *Crn-A, B, C* parageneses crystallized at pressures ≥ 1 Gpa, within the uppermost mantle beneath Mt Carmel.

On the modelled plots, the melts calculated from hibonite enclosed in corundum aggregates fall within the hibonite field or near the hibonite-corundum peritectic (crn + melt → hib) at all pressures; this is consistent with the parageneses, in which hibonite crystallizes after corundum.

The hibonite-related melt calculated from coarse-grained hib + gross ± V^0 xenoliths plots in the hibonite field in Fig. 23a, and on the hibonite-grossite cotectic in Fig. 23b and 23c, while at 1 and 2 Gpa (Fig. 24) it is on the peritectic, consistent with the occurrence of resorbed corundum cores in hibonite crystals. In the 1-Gpa plot, the liquidus field of grossite is absent, but it is not clear where (between 1 atm and 1 Gpa) grossite ceases to be a liquidus phase. This paragenesis may be genetically related to the *Crn-B* melts, but crystallized at *P* <1 Gpa.

The calculated melts in equilibrium with the hibonite-gehlenite anorthite xenoliths give conflicting results. In the 1-atm. phase diagrams (Fig. 23a,b) they plot close to the corundum-hibonite peritectic, consistent with their petrography. The mesostasis of the hibonite-gehlenite xenoliths plots in the gehlenite field in Fig. 23a near the anorthite-gehlenite cotectic. In Fig. 23b the mesostasis is close to the gehlenite-hibonite-anorthite eutectic, also consistent with its petrography. The presence of anorthite in the paragenesis implies that the hibonite-gehlenite cumulates crystallized at *P* < 0.9 Gpa (near the crust-mantle boundary) probably from melts like those that crystallized hibonite in the corundum aggregates.

The assemblage srilankite ($(Ti_{0.53}Zr_{0.47})O_2$) + rutile occurs in *Crn-C* aggregates. The Ti/Zr ratio of srilankite in equilibrium with rutile is a function of both *T* and *P* (Troitzsch et al., 2005). Assuming *T* of 1300–1400 °C (see below), this srilankite-rutile pair would require *P* of *ca* 1.5 GPa, corresponding to depths of *ca* 45 km, within the basaltic underplate imaged by seismic data. Sapphirine has a very small liquidus field in the $MgO-Al_2O_3-SiO_2$ system at P <2 GPa (Belmonte et al., 2017), but a wider stability range in the subsolidus. The rare occurrence of this phase in some melt pockets (Supplementary Material, Fig. S-14) implies *P* (at *T* > 1000 °C) above ca 1 GPa, but below 2 GPa (Christy, 1989; Podlesskii, 2010).

5.1.4. Temperature estimates

The immiscible separation of Fe-Ti-Si-P-C melts from oxide melts probably occurred at *T* ≤ 1500 °C, and many compositions cluster around cotectics and eutectics in the Fe-Ti-Si system (Weitzer et al., 2008) with temperatures ranging from 1300 to 1500 °C (Griffin et al., 2022); some subsolidus assemblages indicate temperatures of *ca* 1200 °C. Reconstructed Si^0 melt inclusions in SiC crystals suggest *T* between 1450 and 1250 °C (Huang et al., 2020). These *T* estimates must be regarded as maximum values, given the abundance of volatile phases in the Mt Carmel assemblages. Hydrogen, in particular, can lower the liquidus and solidus temperatures of metallic melts by several hundred degrees (Fukai, 2006).

The coarse-grained hibonite-grossite xenoliths contain the phase $Ca_4Al_6O_{12}F_2$, which in the 1-atm. $CaF_2-CaAl_2O_4$ system crystallizes from 1480 °C to a eutectic with CaF_2 at 1375 °C, but is unstable in the subsolidus at *T* < 1150 °C. The fluorite-grossite assemblage in these xenoliths crystallizes at *ca* 1375 °C in the same system (Griffin et al., 2019a). Crystallization temperatures for the spinels in the melt pockets of the *Crn-A* paragenesis are mostly between 1285 and 1460 °C (Fig. 19; Supplementary Material, Table S-12).

Experimental studies in the 1 atm. Zr-Ti-Al oxide system (Ilatovskaia et al., 2017) show that Al_2TiO_5 (griffinite) coexists with Al_2O_3 + TiO_2 (consistent with its paragenesis) at 1284 °C, but at 1357 °C griffinite would coexist with either ZrO_2 + Al_2O_3, $ZrTiO_4$ +- Al_2O_3 or $ZrTiO_4$ + TiO_2. $ZrTiO_4$ is equivalent to the srilankite ($(Ti,Zr)O_2$) noted above. Ferroarmalcolite, a major phase crystallized from the immiscible Ti-Fe-oxide melts (Supplementary Material, Table S-6), crystallizes from at *T* ranging from < 1200 °C at 1 atm. to 1350 at 1.5 GPa (Friel et al., 1977).

Under reducing conditions, the maximum solubility of Ti^{3+} in corundum is dictated by the precipitation of tistarite and increases with increasing temperature (Fig. 25; Yasuda et al., 1998). In the *Crn-A* paragenesis, unzoned or weakly zoned parts of corundum crystals with melt pockets containing tistarite carry 0.20–0.40 mol % Ti_2O_3 (Fig. 12c). Assuming equilibrium with tistarite, these would give T_{min} of 1300–1325 °C. Other grains have long unzoned profiles with up to 1.2 mol% Ti, equivalent to *ca* 1375 °C. The much higher Ti contents in the outer parts of zoned grains (1.5–3 mol %) would give T_{min} up to *ca* 1600 °C. However, this zoning to higher Ti is unlikely to reflect higher *T* during crystallization, since resorption is not obvious. This suggests that the melts were no longer in equilibrium with tistarite, as fractional crystallization closed off individual melt pockets (Oliviera et al., 2021), and reactions such as tistarite + melt → carmeltazite isolated early-crystallized tistarite from the melt. Similarly, microstructures indicate that the Crn-B grains with the highest Ti_2O_3 were not in equilibrium with tistarite, but were still reduced enough to keep Ti as Ti^{3+}.

All of these *T* estimates lie well above the xenolith-based geotherm (Lu et al., 2022) at lithospheric pressures. If the values > 1400 °C are correct they imply high mantle potential temperatures, consistent with models that derive the basalts from a fossil plume head (Stein and Hoffmann, 1992), and with the high MgO contents and Mg# of the vent magmas (Supplementary Material, Table S-1). The intrusion of high-T melts at relatively shallow mantle depths is also consistent with the advective nature of the xenolith-based geotherm.

There are few firm subsolidus temperatures below *ca* 1150 °C, suggesting that most of the sampled subsystems did not cool significantly below this *T* prior to eruption.

5.1.5. Oxygen fugacity

In the hibonite-gehlenite xenoliths, the presence of spinels with both Fe^{3+}, Fe^{2+} and high levels of Ni^{2+} suggests fO_2 ca two log units above the iron-wüstite buffer (ΔIW + 2), whereas the coexistence of Fe-bearing spinels and metallic alloys in the cumulates of Cr-rich corundum implies fO_2 near IW. The onset of melt-melt immiscibility recorded by the iron-iron oxide-titanium oxide spherules also must have occurred at fO_2 near the IW buffer. The coexistence of Cr^0 with the most Cr_2O_3-rich corundum implies fO_2 near the Cr-Cr_2O_3 buffer, at ΔIW −4.4. The abundance of Ti^{3+}-bearing phases in the melt pockets of Crn-A and Crn-B aggregates, and the presence of phases with both Ti^{3+} and Ti^{4+} in Crn-B and Crn-C indicate fO_2 near or below the TiO_2-Ti_2O_3 buffer, at ΔIW −4.6. The separation of immiscible Si^0 melts could occur near the SiO_2-Si buffer (ΔIW-6.5). The presence of moissanite (SiC) in both Fe-Ti-Si melts and the trapped silicate melts of the corundum aggregates requires fO_2 = ΔIW ≤ -6.7 (Ulmer et al., 1998). Still lower fO_2 is required by the presence of native vanadium in the coarse-grained hibonite-grossite xenoliths; the V^0-VO buffer lies at ΔIW −8.2 (Ulmer et al., 1998). The occurrence of Ti^{2+} phases such as TiS, Ti(N,O,C) and TiB_2 (Griffin et al., 2020b,2021a) suggests fO_2 below

the Ti_2O_3-TiO buffer, at *ca* ΔIW −9.3. In the Crn-A paragenesis the increase in the Si content of the Fe-Ti-Si melts with decreasing T (Griffin et al., 2022) also requires a corresponding decrease in fO_2 (Weitzer et al., 2008), probably to *ca* ΔIW −9.

There is some evidence for reversals of this overall reduction trend; local oxidation is indicated by the exsolution of kaitainite from tistarite (Supplementary Material, Fig. S-14) and by pseudomorphs of carmeltazite by griffinite + rutile ± ziroite.

5.2. The basalt-megacryst suite – Guides to the magmatic setting

5.2.1. Zircons

The zircons record ≥200 Ma of basaltic underplating near the base of the crust, from Permian to Cretaceous (Griffin et al., 2018b), and extending into Miocene-Pliocene time. Over this time the temperature in the crust-mantle transition zone (25–40 km) probably did not fall below 800–1000 °C (Lu et al., 2021), allowing the slow cooling and differentiation of successive generations of magmas. Zircon rarely crystallizes from mafic magmas, but with slow cooling and extended fractional crystallization it can crystallize from late residual melts or fluids (Guo et al., 1996). As noted above, most of the zircons from the Mt Carmel tuffs and the associated paleoplacer deposits have trace-element patterns consistent with crystallization from syenitic or monzonitic melts, and mantle-like O isotopes.

5.2.2. Sapphires

The sapphire megacrysts from Mt Carmel are similar in terms of colour, zoning, and O isotopes to those from alkali basalts in e.g. Laos, Vietnam, Thailand and eastern Australia. In the plot of Peucat et al., (2007; Supplementary Material, Fig. S-23) the Mt Carmel sapphires have Fe contents typical of magmatic sapphires, but extend out of the "magmatic field" toward lower Ga/Mg. However, Ga/Mg is well-correlated with Fe/Mg, and the generally higher Mg content of the Mt Carmel sapphires is accompanied by higher Cr and higher Ti, following the plumasitic "Kashmir trend" (Fig. S-23), related to desilication of low-SiO_2 magmas by interaction with ultramafic rocks.

Mineral inclusions from basalt-related sapphires worldwide comprise plagioclase, zircon, monazite, Nb-Ta oxides and carbonates, accompanied by CO_2-rich fluids (Guo et al., 1996; Song and Hu, 2009; Xu, 2021), supporting an origin by crystallization from broadly syenitic differentiates of mafic magmas in the deep crust/upper mantle. Melt inclusions in sapphires from Bo Ploi (Thailand) have compositions ranging from trachyte-trachyandesite to Ne-syenite, with homogenization temperatures ranging from 800 to 1000 °C (Srithai and Rankin, 1999). For example, sapphires from S. Vietnamese basalts contain zircons with ages identical to the basalts' eruption ages, and trace elements indicating crystallization from highly evolved felsic melts (Vu et al., 2021).

5.2.3. Ilmenites

The Mt Carmel ilmenite "megacrysts" are similar to those in alkali basalts from many locations (e.g., Haggerty, 1976; Ellis, 1976; Barr and Dostal, 1986; Agata, 1998). They form two broad groups; low-Cr grains that overlap the compositions of ilmenites from garnet pyroxenite xenoliths (Lu et al., 2022) and high-Mg, Cr,Ti ilmenites that suggest a more complex process. A possible analogue for the latter group is found in the Lherz peridotite massif (France) where ilmenite has crystallized from alkali-rich felsic melts that intruded and reacted with peridotites at 1.25–1.5 GPa (Lorand and Gregoire, 2010); the most Mg-rich ilmenites come from the thinnest veins. The Lherz ilmenite trend of high Mg and Cr also is seen in the ilmenites from the Rakefet Magmatic complex (Fig. 5c). Lorand and Gregoire (2010) argue that the felsic veins at Lherz were water-poor, which would suppress the crystallization of amphibole and enhance the early crystallization of an Fe-Ti oxide. They calculate an fO_2 of ΔQFM −4.7 (*ca* ΔIW −1) and suggest that the peridotite was being fluxed by CH_4-rich fluids that oxidized during passage through the SCLM.

These comparisons suggest that the Mt Carmel sapphires, zircons and ilmenites crystallized from broadly syenitic melts, in a

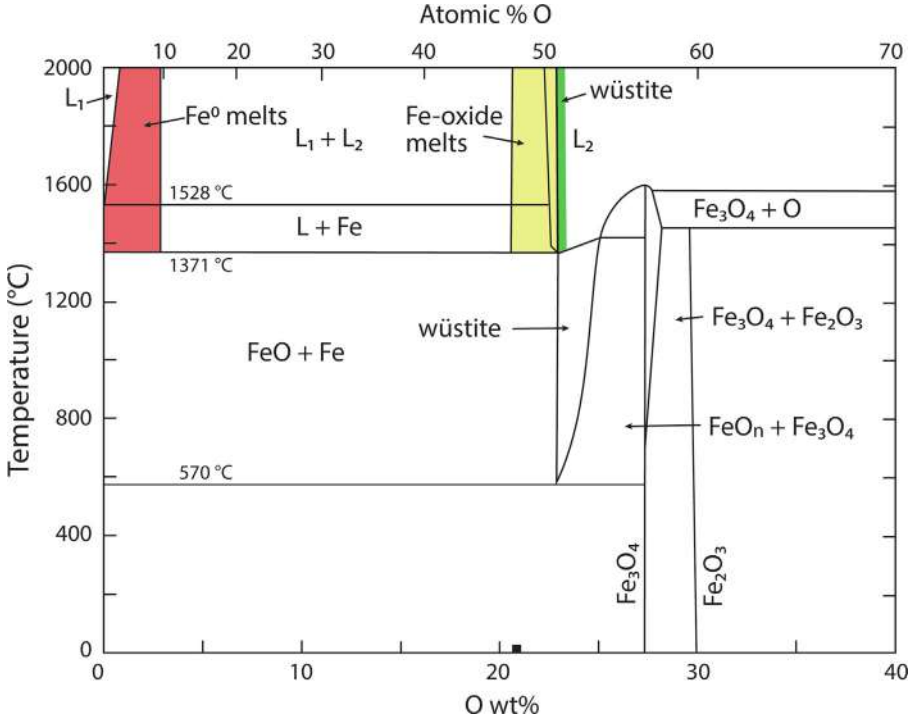

Fig. 26. Phase diagram of the Fe-O system at 1 atm. (after Wriedt, 1991). See text for explanation.

setting where they could interact with ultramafic or high-Mg mafic rocks. The low-Cr spinels suggest the differentiation of mafic magmas, perhaps during the evolution of the syenitic melts, while the ilmenite populations appear to reflect interaction between syenitic melts and the surrounding ultramafic rocks. This type of reaction could also desilicate syenitic melts and lead to the crystallization of the "plumasitic" sapphires.

The ponding and differentiation of mafic magmas would be expected within the thick mafic underplate that developed beneath the Mt Carmel/Yizre'el Valley area from Permo-Triassic to Late Cretaceous and Miocene-Pliocene time. The interaction of each melt generation with earlier ones is evidenced by the abundance of older cores in younger zircons throughout this period (Griffin et al., 2018a). Slow cooling toward an elevated geotherm and the intermittent input of heat from mantle-derived mafic magmas would provide the conditions required for both extended fractional crystallization and the interaction of melts with the mafic to ultramafic wall rocks. Even if older melt ponds had largely crystallized, they would be easily remelted with modest additions of heat and volatiles from the next magmatic episode.

5.3. Significance of the Fe-Ti oxide melts – Silicate-rich vs Fe-rich melts

The compositional and microstructural features of the Fe-Ti oxide spherules, some with cores of native Fe (section 4.5.1), suggest that they represent melt immiscibility at fO_2 near the IW buffer, while the crystallization of ferroarmalcolite indicates conditions near the Fe-TiO_2-$FeTiO_3$ buffer (ΔIW −1).

The 1-atm. phase diagram of the Fe-O system (Darken and Gurry, 1946; Wreidt 1991; Fig. 26) shows a two-liquid field between Fe^0 and Fe-oxide melts down to *ca* 1528 °C; this field is poorly constrained at $T > 1600$ °C. Below 1528 °C, Fe^0 coexists with an Fe-O liquid down to 1371 °C; at lower temperatures Fe^0 coexists with near-stoichiometric FeO. Below 1528 °C the liquid oxide coexisting with solid Fe^0 becomes more oxygen-rich with decreasing temperature, and at the eutectic (1371 °C) Fe + liq + wüstite the liquid has 23.2 wt% O, while the wüstite has 25.3 wt% O. This analysis suggests that the Fe-oxide melts and the stoichiometric FeO phase (s) analyzed here formed at temperatures higher than 1370 °C (Supplementary Material, Table S-22). The compositions of the Fe^0 and FeO melts (Fig. 26) suggest that under the natural conditions the gap between the Fe^0 and Fe-oxide melts is narrower than in Fig. 26. However, the overall phase relationships are consistent; the blocky wüstite grains (Supplementary Material, Fig. S-5) are more oxygen-rich than most of the Fe-oxide melts. The temperatures of the Ti-oxide melts are difficult to constrain, but slag studies (Fourie et al., 2005) show that these compositions would be liquids in equilibrium with Fe-liq + pseudobrookite at 1500 °C. As noted above, all *T* estimates drawn from these simple systems would be maximum values, given the presence of Mn, Ca, Mg, Si, and especially H_2 in the melts (Fukai, 2006).

The microstructures of the metallic and oxide spheroids (Fig. 7,8) are notably similar to the organization of motile microscale oil-in-water emulsion droplets solubilized in an aqueous surfactant solution (Meredith et al., 2020; Supplementary Material, Figs S-24, S-24-v). In such emulsion systems, compositional differences between two or more partially miscible droplet species induce micelle-mediated oil exchange through the continuous aqueous phase. The asymmetric exchange of oil between droplets of differing composition establishes chemical gradients in the surrounding fluid and differences in interfacial tension across surfaces of adjacent droplets, resulting in droplet motion via the Marangoni effect. With sufficient asymmetry in the rates of chemical exchange, predator–prey-like interactions can emerge, leading to the capture of prey by predator droplets and motility-driven self-organization of multi-body clusters with dynamic behaviours (Fig. S-24-v). Adjusting the surfactant concentration and type affects the magnitude and direction of chemical exchange between droplets. Structures such as the Fe^0 cores in oxide-melt shells, Fe-oxide balls with vapour-bubble "cores", and aggregates of oxide-melt balls of different compositions (Figs. 7, 8) may have formed through analogous processes of chemical exchange and locally emergent flows between dispersed melt and fluid phases. Similar effects have been observed in calcium aluminosilicate glasses (Clark et al., 2022).

The clusters of metallic and oxide spheroids (Figs. 7, 8) reflect a process involving multiple immiscible liquids: Fe^0 melt, Fe-oxide melts, Ti-Fe oxide melts, and C-O–H fluid. In a differentiating melt, all of these phases may have appeared essentially simultaneously, producing a dense emulsion similar to the experimental situation described above. We suggest that this multiple immiscibility occurred when the fO_2 of the melt dropped below the IW buffer, triggering the separation of Fe^0 melts. Gravitational removal of the metal/metal oxide droplets would deplete the host silicate melt in Fe, and perhaps in Ti, but enrich it in most other elements.

Immiscible high-iron oxide melts in syenitic xenoliths from basalts of the Western Carpathians closely resemble the Fe-oxide and Ti-Fe oxide melts described here (Hurai et al., 1998; Supplementary Material, Table S-21). The xenoliths are interpreted as differentiates of the alkali basalts. Another analogue may be the blocks of native iron in the basalts of Disko Island, Greenland. These are cumulates of spherules (0.5–1 mm) of immiscible iron melts formed by interaction between basalt magmas and carbonaceous sediments >3 km below the surface (Bird et al., 1981; Pedersen, 1979,1981; Ulff-Møller, 1990) generating fO_2 in the range IW to ΔIW −1. These conditions are more reducing than the CCO buffer at the estimated pressures and imply a high fH_2. The removal of the Fe^0 droplets from the basaltic parent melt left a broadly andesitic residual melt, found as xenoliths in the basalts (Ulff-Møller, 1990).

5.4. Origin of "parental melts" by immiscibility

The melts parental to those trapped in the corundum aggregates (Supplementary Material, Table S-20) are low in SiO_2 and nearly Fe-free, yet have very high concentrations of HFSE and REE, and their very small Eu anomalies (Fig. 16) make feldspar fractionation unlikely. It is difficult produce such melts by simple fractional crystallization from a syenitic or basaltic melt. We suggest that the solution lies in the element partitioning that takes place during the immiscible separation of Si-Al-rich melts and FeO-rich melts, accompanied by extreme reduction.

Coexisting melts have been described in melt inclusions in lunar basalts, in mantle-derived peridotites, and in the groundmass of terrestrial volcanic rocks. Most studies of melt immiscibility deal with broadly tholeiitic parental melts, and typically produce two conjugate melts, one concentrating Fe, Mg, Ca and P, and other Si, Al, Na and K (Supplementary Material, Table S-23). This process has been recognized in plutonic settings, including the upper zones of the Skaergaard intrusion (McBirney and Nakamura, 1974; Jakobsen et al., 2005) and the Bushveld Complex (Fischer et al., 2016), mainly by analysis of fluid inclusions in cumulate phases such as apatite. Similar coexisting melts have been produced experimentally (Table S-23; Watson, 1976; Veksler et al., 2006, references therein), and coexisting Fe-rich and Si-rich melt inclusions in typical "basaltic" sapphires have been interpreted as reflecting immiscibility in a parental syenitic melt (Xu et al., 2021). In natural occurrences and experimental studies the transition elements, HFSE and REE partition strongly into the immiscible FeO-rich melts (Hurai et al., 1998; Veksler et al., 2006), while coexisting silica-rich melts concentrate both Al_2O_3 and LIL elements. However, the stability of AlO_4 tetrahedra in a highly polymerized SiO_2-rich melt is

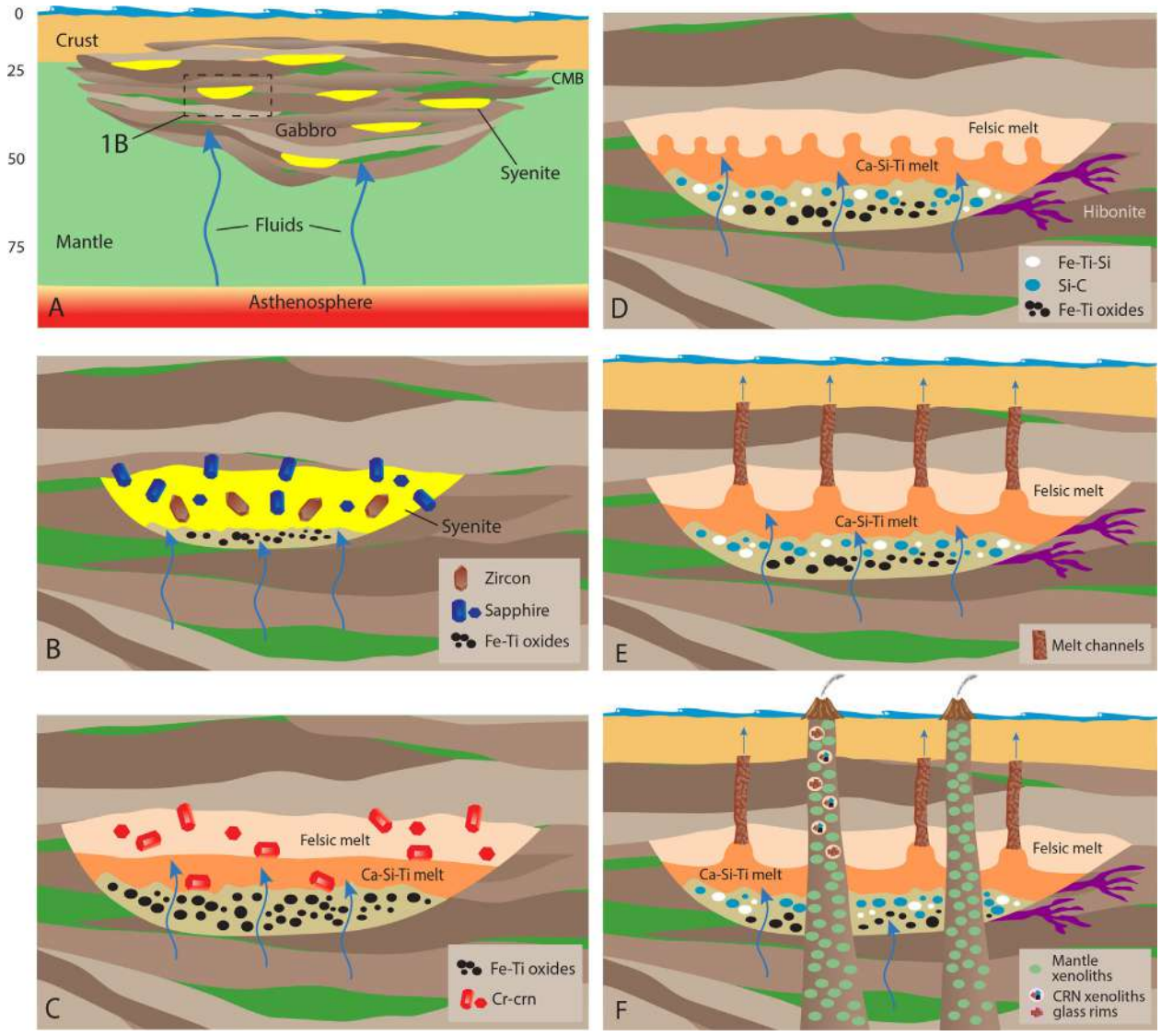

Fig. 27. Cartoon illustrating the proposed evolution of the super-reduced assemblages, focussed on the corundum-aggregate parageneses. (a) Formation of a gabbroic underplate (Triassic – Pleistocene) with lenses of syenitic differentiates, fluxed by mantle-derived $CH_4 + H_2$ fluids. (b) Crystallization of corundum and zircon megacrysts, separation and sinking of Fe^0, Fe-Ti-oxide melts. (c) separation of Fe-rich and Si-rich immiscible melts, crystallization of Cr-rich corundum. (d) Further reduction, separation of Fe-Ti-Si and Si^0-SiC melts; development of residual CAS melts. *Crn-B* is crystallizing and accumulating in the lower part of the chamber, and *Crn-C* in the upper parts. Loss of Fe decreases density of the Ca-Al-Si-Ti melts, leading to gravitational instability at the interface between Si-rich and Si-poor melts. Escape of evolved melts + H_2 produces highly-reduced hibonite + grossite + V^0 assemblages. e) melt mixing and fluid saturation leads to development of melt-escape channels with precipitation of *Crn-A* corundum aggregates. (f) explosive eruption of alkali basalts samples magma chambers, builds small volcanoes.

greatly reduced in systems with low contents of alkali elements. This results in a preference of Al (and Ti) for the FeO-rich melts by factors of 3–4, where their substitution is balanced by divalent cations.

The generation of immiscible Fe-rich and Si-rich melts can lead to the development of stratified magma chambers, as the denser Fe-rich melts sink to the bottom and the Si-rich members rise to the top (*cf. the Disko Island* example above). The upper part of the Bushveld intrusion may represent the largest single example of such vertical segregation (VanTongeren and Mathez, 2012), while in the smaller Skaergaard intrusion the two melts may have remained in an emulsion-like state (Charlier et al., 2013; Jakobsen et al., 2005). However, the rare eruptions of Fe-oxide melts (e.g., Naslund,1983) suggest that more complete segregation may be common, but rarely expressed due to the density constraints on eruption of such Fe-rich melts.

The second key to the origin of the "parental" melts of the corundum aggregates is the potential for an unusual fractionation path driven by the progressive lowering of fO_2. This prevents the crystallization of magnetite and retains Fe in the melt to the point (fO_2 = ΔIW 5 to −6) where it is extracted as immiscible Fe-Ti silicide melts, leading to desilication of the residual melt. This fractionation can explain the evolution of an essentially Fe-oxide melt to the highly aluminous, Fe-free CAS melts trapped in the corundum aggregates.

5.5. A model

The model proposed here (Fig. 27a) involves the evolution of syenitic magma chambers, formed by the fractional crystallization of mafic magmas, broadly analogous to the upper zone of the Skaergaard intrusion (McBirney and Nakamura, 1974; Jakobsen et al., 2005). These melts would crystallize the megacryst suite (including zircon, corundum, ilmenite) described above (Fig. 27b). The lowering of fO_2 by a flux of mantle-derived $CH_4 + H_2$ would prevent the early crystallization of magnetite, but the melt would

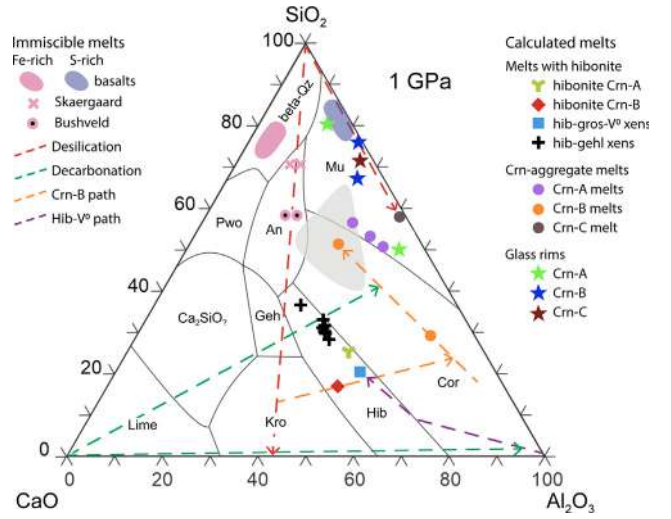

Fig. 28. CAS plot at 1 GPa (from Fig. 24), including compositions of immiscible felsic and Fe-oxide melts from basalts, the Bushveld Complex and upper zone of the Skaergaard intrusion (data from Table S-22). Dashed red lines show the effect of desilication (removal of Fe-Ti-Si and Si^0 melts); dashed green lines ("decarbonation") show the effect of removal of Ca-Mg carbonate, either by crystallization of carbonates or the extraction of carbonatitic melts, initiated by the production of CO_2 during the oxidation of methane-rich fluids. Dashed purple line shows the trajectory of melt compositions that led to the coarse-grained hibonite-grossite-V^0 assemblages (Griffin et al., 2019a). Dashed orange line traces the late crystallization of melts of the *Crn-B* paragenesis.

exsolve immiscible Fe^0- and Fe-Ti-oxide melts and wüstite as fO_2 approached the IW buffer. Further fractionation would lead to the separation of the syenitic melt into Si(Na,K,Al)-rich and Fe (REE,HFSE)-rich immiscible melts (Fig. 27c). Models of lunar systems suggest that the volume of the Fe-rich immiscible melt would be several times larger than that of the Si-rich melts.

Fe-oxide melts are very dense and very fluid (Bird et al., 1981; Pedersen, 1979; Veksler et al., 2006) and would sink to the bottom of the magma chamber, leaving the alkali-rich felsic melt above. This would produce an isolated lower layer with a thermal gradient, resistant to disturbance by convection (Jaupart et al., 1984). If the magma chamber were being flushed with reducing fluids, these might affect the lower layer most strongly, but such fluids also could reach the upper layer of the chamber, especially once the lower layer had lost any significant buffering capacity. For example, Nazzareni et al. (2019) have described the occurrence of SiC in syenitic differentiates of oceanic basalts.

The next recognizable step (in terms of decreasing fO_2) is the formation of Cr-Al-Na-K oxide melts (ΔIW −4 to −5) and the crystallization of cumulates with high-Cr corundum ± Cr^0 ± Cr-Ga alloys and Na,K β-alumina phases (Griffin et al., 2021b). The high alkali contents suggest that these melts separated from the Si-rich immiscible silicate melts. If similar melts also separated from the conjugate Fe-rich melts, they would effectively reduce the alkali-element contents to the low levels observed in the melt-pocket glasses.

The Si-SiO_2 and Ti_2O_3-TiO_2 buffers (ΔIW −5 to −7.5) mark the separation of immiscible Si^0, Fe-Ti-Si and Si-Fe-Al-C melts (Huang et al., 2020), leading to the gravitational removal of Fe, P and Si. The dissociation of $Ti^{4+} \rightarrow Ti^0$(in alloys) + Ti^{3+} would leave Ti^{3+} in the silicate melt. The loss of Si leads to saturation in Al_2O_3 and the precipitation of Ti^{3+}-bearing corundum.

As the cumulates compact, melt volumes shrink; the removal of Fe from the melts leaves them with little buffering capacity, and higher fluid/melt ratios lead to a rapid decrease in fO_2. The distribution of trace elements (section 4.6.3.1) and their microstructures (Supplementary Material, Fig. S-22) suggests that the *Crn-B* corundum aggregates crystallized as cumulates in the lower portion of this system, while *Crn-C* aggregates formed as cumulates in the upper, more felsic part.

The precipitation of the coarse-grained hibonite + grossite + v anadium assemblage at ΔIW-8 to −9 implies that fO_2 was controlled by hydrogen-dominated fluids. This paragenesis may have been localized in smaller melt volumes with high fluid contents, favouring pegmatitic growth.

The removal of the immiscible Fe-Ti-Si and Si-C melts reduces the density of the remaining fluid-rich oxide melt, creating a gravitational instability conducive to overturns and disruption of the layering (Fig. 27d). Overturns could trigger the escape of volatile-rich melts and reduced fluids; the skeletal *Crn-A* corundum aggregates probably grew along short-lived melt-escape channels (Fig. 27e), with high levels of H_2. These overturns and mixing between more- and less-reduced layers could explain the late oxidation of carmeltazite and other SUR phases in some *Crn-B* corundum aggregates (Supplementary Material, Figs S-12, S-13). Explosive eruption (Fig. 27f) was accompanied by brecciation driven by the injection of volatile-rich fluids (Na, K, F, S, Cl, C, CH_4). The preservation of glass and quench textures in the corundum-aggregate melt pockets is consistent with the known speed of xenolith-bearing pyroclastic eruptions (O'Reilly and Griffin, 2010) leaving no time for reaction of the melts with the surrounding crust.

Can this generalized model produce the range of "parental melts" identified for the different parageneses described above? The melts calculated or reconstructed from hibonite-bearing assemblages in the corundum aggregates and the coarse-grained hibonite + grossite xenoliths are typically low in SiO_2. Fig. 28 shows that desilication of the natural immiscible melts listed in Supplementary Material Table S-23 would produce low-Si melts, but with Ca/Al ratios higher than any observed or calculated for the Mt Carmel materials.

To move these desilicated melts toward the compositions of those calculated from the hibonite-bearing assemblages, significant amounts of Ca would need to be removed. The Mt Carmel assemblages contain no important Ca-rich phenocryst phases that could accomplish this through fractional crystallisation. However, the reduction of the magmatic system by oxidation of CH_4 would produce CO_2, with the potential to crystallize Ca-bearing carbonates, or to generate immiscible carbonatitic fluids/melts that would sequester CaO and to some extent MgO. Such carbonatitic melts may be the source of the zoned carbonate crystals in the volcanic ashes (Supplementary Material, Fig. S-4). The $^{87}Sr/^{86}Sr$ values of these carbonates (0.706 ± 1; Supplementary Material, Table S-3) are similar to those of EMI basalts, a signature that has been variously interpreted as reflecting the involvement of the metasomatized lithospheric mantle or the lower continental crust (see review by Lustrino and Dallai, 2003).

The generalized evolution of the desilicated melts can be sketched by the compositional trajectory of the Crn-B paragenesis in the CAS plot (Fig. 28), from the melts coexisting with hibonite (an early phase) to those that precipitated sassite (a late phase) and finally to the residual melt. The calculated parental melt of the sassite (Supplementary Material, Figures S-12 and S-22) is Si-poor but high in TiO_2 (41 wt%) and Al_2O_3 (30 wt%). The step from the hibonite-related melt to the sassite-related melt cannot be accomplished by the removal of hibonite or grossite, both low in Ca, but could be driven by the separation of a carbonatitic melt/fluid, accompanied by the continued crystallization of corundum. The residual melt (following removal of sassite and corundum; Supplementary Material, Table S-20) is similar to many other trapped melts in both *Crn-A* and *Crn-B*. The evolution of the coarse-grained hibonite + grossite + V^0 assemblages (Griffin et al.,

2019a) requires a very low-Si melt in the corundum field; crystallization of corundum drives the melt to the hibonite-corundum peritectic, and then to the hibonite-grossite cotectic (not shown in Fig. 28).

The parental melt of hibonite in *Crn-A* aggregates is close to the one for *Crn-B*, but *Crn-A* hibonite is higher in Ti and lower in LREE than *Crn-B* hibonite. The trajectory from "parental" melts to trapped melts in *Crn-A* is not constrained, but may be similar to that sketched for *Crn-B*. This model suggests that the "first trapped melts" of the *Crn-A* paragenesis actually were residual melts in contact with *Crn-B* cumulates, consistent with their high levels of incompatible elements and volatiles.

The felsic component of natural immiscible-melt pairs is typically CaO-poor (Fig. 28, Supplementary Material, Table S-22), and the effect of desilication would be simply an increase in Al_2O_3 and alkali elements. However, the Si-Al-rich immiscible melts would have low contents of elements that could form silicides to produce extensive desilication. As shown in Fig. 28, most glass rims on corundum-aggregate xenoliths are only weakly depleted in SiO_2 compared to natural immiscible felsic melts.

The occurrence of Ba-rich glasses as rims on ejecta of the corundum aggregates implies that this melt coexisted with the CAS trapped melts. Compared to the trapped melts, the Ba-rich glasses are also strongly enriched in Na, Al, Zr and Hf, but depleted in REE, Ca, Sr and Ti (Supplementary Material, Table S-19). The Ba-rich melts thus may be fractionation products of the SiO_2-rich melts in the upper parts of a magma chamber, coexisting with cumulates similar to the Crn-C aggregates. This would be consistent with these glasses coating corundum-aggregate xenoliths derived from the lower parts of the chamber, as they ascended during eruption.

The evolution of the idealized magma system sketched above may have proceeded on timescales of 10^4-10^5 years, as suggested for bodies such as the Skaergaard or Bushveld intrusions (e.g., McBirney, 1996). In contrast, diffusion modelling (Fig. 12) indicates that the growth of *Crn-A* corundum proceeded on timescales of days to years. In its final stages, this idealized magmatic system would have contained several mutually immiscible melts, including Ti(N,O,C), Fe-Ti-Zr-Si alloys, the *Crn-A* "parental melt", the Ba-rich felsic melts, carbonatitic melts, and one or more fluids rich in alkali elements, carbon, hydrogen, Cl and F·H_2O-rich, CH_4-rich and H_2-rich fluids would be mutually immiscible and could coexist under these conditions (Bali et al., 2013; Preteanu et al., 2017; Vlasov et al., 2023). The conditions at which such immiscibility appears to have occurred in the Mt Carmel material lie at higher *T*/*P* than experimental determinations of the critical point for H_2-H_2O systems, but are close to the curve modelled by Bergermann et al. (2021).

The magmatic underplate as a whole may have been zoned in fO_2, with the lower parts generally more reduced due to longer exposure to the reduced fluids. In such a scenario, the hibonite-gehlenite xenoliths might represent cumulates formed at shallower levels and somewhat higher fO_2 than the idealized model. The materials described here thus may represent many different magma chambers that developed episodically from Triassic time onward before being sampled during the late Cretaceous Mt Carmel volcanism, and again during Miocene-Pliocene volcanism in the Yizre'el Valley.

5.5.1. Volatiles in the magmatic system

The wide range of fO_2 recorded in the Mt Carmel xenoliths requires a source of low-fO_2 fluids to reduce the primary melts produced by immiscibility within broadly syenitic precursors. Our model predicates the introduction of such fluids at high fluid/rock ratios, gradually overwhelming any mineral associations capable of buffering fO_2 at the more "normal" levels (*ca* FMQ) typical of most volcanic eruptions.

Throughout the proposed evolution, the presence of a free fluid phase, immiscible with the silicate/oxide melts, is witnessed by vesicular plates of wüstite and hollow spheres of Fe-FeO and Ti-Fe oxide melts; spherical to ovoid bubbles in the glasses of melt pockets; crystallographically controlled voids in hopper crystals of corundum (especially in *Crn-A*); interstitial voids with euhedral crystals of phenocryst phases; and explosive breccias with a matrix of amorphous carbon. The high carbon content of these fluids is confirmed by analysis of the trapped volatiles (Supplementary Material, Table S-18) and by the crystallization of C-rich phenocryst phases (Ti(N,O,C), TiC, SiC) in trapped melts.

The lowest fO_2 values are similar to those estimated for the early Solar nebula, in which H_2 was the dominant species. This is consistent with the speciation of sulfur in the Mt Carmel material. S normally partitions into the vapour phase (relative to the melt phase) at low P, and this partitioning is enhanced at low fO_2, where S^{2+} is less soluble in melts (Edmonds and Wallace, 2017). However, even though the corundum aggregates (especially Crn-A) are highly reduced, S was retained in the trapped melts, finally crystallizing as TiS, MnS and mixed sulfides of Ti, Mn, Cr and Ce (Supplementary Material, Table S-15). This suggests that *P* was high enough (≥1 GPa) to retain S in the melt despite the low fO_2, and that the partial pressure of H_2S was relatively high. At magmatic temperatures (1300–1500 °C) MnS is stable only at $H_2S/H_2O > 10^{-3}$ (Larimer, 1968); this is similar to estimates for Cosmic gasses (H_2S/H_2O *ca* $10^{-1.7}$), where hydrogen is by far the dominant species (H_2O/H_2 *ca* 10^{-4}). However, the absence of CaS and MgS in the Crn-A,B aggregates indicates that H_2S/H_2O probably was not much higher than the Cosmic value (Larimer, 1968).

Gasses released by fusing samples of *Crn-A* (n = 4) have average contents of 107 ppm N, 310 ppm C, 490 ppm H (ca 95at.% H) and 130 ppm S (Supplementary Material, Table S-18). At the low fO_2 of these fluids and *P ca* 1 GPa, most C would be present as CH_4. It therefore seems clear that the fluids were dominated by CH_4 + H_2, with lower but significant levels of S and N. If the corundum aggregates crystallized within the mafic underplate below the crust/mantle boundary (*P ca* 1 GPa) then the reducing fluids must have been derived from the subjacent mantle (>75 km).

The isotopically light carbon in the abundant SiC ($\delta^{13}C$ = -25 to –32; Huang et al., 2020) and in the amorphous carbon of the eruptive breccias ($\delta^{13}C$ = -19 to –22) is similar to the low-$\delta^{13}C$ component in kimberlites sourced from the deep mantle (Giuliani et al., 2022), and in sublithospheric Type IIb diamonds ($\delta^{13}C$ = -25 ‰; Smith et al., 2016). Isotopically light carbon in the mantle typically is ascribed to the subduction of crustal organic material. However, isotopic fractionation occurs during metal-carbonate reactions, with ^{13}C concentrating in melts while ^{12}C is sequestered in alloys; this mechanism seems more consistent with the high ratio of carbonate to organic carbon in subducted oceanic crust (Reutsky et al., 2023). The isotopically light carbon, as well as the primitive isotopic nature of the He (R_A = 8.1 ± 0.2) trapped in the corundum aggregates, is thus consistent with a mantle derivation of the reducing fluids.

CH_4 probably is ubiquitous in the sublithospheric mantle (Matjuschkin et al., 2020) where fO_2 is at least locally controlled by the presence of a free metallic phase (Matveev et al., 1997; Frost and McCammon,2008; Griffin et al., 2018c). CH_4 is only weakly soluble in silicate melts, but it might be physically entrained in volumes of upwelling mantle ("plumes") and liberated once the "plume" stalled at the base of the lithospheric mantle. If the redox state of the lower lithospheric mantle is near the IW buffer (Yaxley et al., 2012), CH_4 would need to travel a few tens of km before reaching the underplate. This could be aided by the concentration of fluids into channels with progressively reduced wall rocks.

This scenario implies that the evolution of the reduced melts within the basaltic underplate was driven by volatiles related to

contemporaneous magmas that stalled at the LAB until eruption. We have no samples of the equivalent volcanic eruptions during the Permo-Triassic to Jurassic magmatic episodes, but the limited radiometric data suggest that some super-reduced material in the Cretaceous and Miocene volcanics dates back to this older magmatism. This may be supported by the drop in fO_2 recorded by zircon xenocrysts that crystallized toward the end of each of the older magmatic episodes (Fig. 4).

5.5.2. Crustal components in fluids?

Some aspects of the fluid chemistry could be regarded as inconsistent with a mantle source. One is the O-isotope composition of the corundum aggregates; most analyses have $\delta^{18}O$ significantly higher than the typical range of "mantle" sapphires recovered from alkali basalts (Fig. 3). This distribution is broadly related to paragenesis. *Crn-B* corundums lie within the field of basaltic sapphires, while those of *Crn-C* spread from the heavy end of the basaltic-sapphire range to $\delta^{18}O$ = 13 ‰. Some *Crn-A* corundums also lie within the basaltic-sapphire field, but most fall in the range $\delta^{18}O$ = 11 to 13 ‰.

In the worldwide summary of Giuliani et al. (2007), $\delta^{18}O$ values of 14–16.5 ‰ are recorded in corundum from skarns and desilicated pegmatites. However, the microstructures, parageneses, *P-T* estimates and low fO_2 of the Mt Carmel samples make a crustal origin unlikely; interaction with the subcontinental lithospheric mantle would, if anything, lead to lower $\delta^{18}O$.

A more probable explanation for the $\delta^{18}O$ range in the *Crn-A* aggregates lies in their crystallization in open systems through which immiscible fluids and melts were moving independently. In this situation, the lighter isotope will concentrate in the fluids, leaving the crystallizing phases isotopically heavier (Mysen, 2018). Similar Rayleigh fractionation is observed during the experimental degassing of tektites, which produces residues with $\delta^{18}O$ up to 4.3 ‰ higher than the starting material (Macris et al., 2017, 2018). It seems likely that the parental melts (and dissolved fluids) of the corundum aggregates had $\delta^{18}O$ within the "mantle range" (Fig. 3), and that higher $\delta^{18}O$ values reflect isotopic fractionation driven by the escape of the volatile phase(s) during the rapid disequilibrium crystallization of *Crn-A* corundum.

Other potential "crustal" components of the melts and fluids include B, F and Cl. Boron occurs as TiB_2, mostly in association with immiscible metallic melts trapped in the corundum aggregates (Griffin et al., 2020a; Supplementary Material, Fig S-18a). Fluorine occurs in fluorite and $Ca_2Al_6O_{13}F_2$ in the coarse-grained hibonite + grossite ± V^0 paragenesis (Griffin et al., 2019a) and as Na-Al-F and K-Al-F phases in the amorphous-carbon groundmass of the explosion breccias. No chlorine-bearing phases have been recognized in the corundum melt pockets, but NaCl and KCl are abundant in the amorphous-carbon matrix of the explosion breccias.

This suite of elements would not be expected to concentrate in the deep crust, much less in the lithospheric mantle; it is more typical of sediments and could be a signature of subducted material in the source of the primary melts. Boron is present in the deep mantle, as shown by the occurrence of boron-bearing Type IIb sublithospheric diamonds (Smith et al., 2018), and Maas et al. (2005) have argued for a Cl-rich reservoir in the deep mantle as the origin of comagmatic chlorides and carbonates in the very fresh Udachnaya East kimberlite.

There is no evidence for a subducted slab beneath Mt Carmel, but the mantle Transition Zone (MTZ) of the eastern Mediterranean may contain remnants of slabs derived from the subduction zones that have affected the region since mid-Proterozoic time. The MTZ might therefore have served as a source of "crustal" elements and volatiles, to be incorporated in melts rising from deeper levels or from the MTZ itself. Seismic tomography (Kaviani et al., 2018) suggests that the MTZ beneath the Levant is thinned, with upwarping of the 660-km discontinuity, and has a relatively low *Vs*. This mapping suggests an upward flow of lower-mantle material into the upper mantle, concentrated beneath the Afar Rift but spreading strongly northward along the plate boundary marked by the Dead Sea Rift. This deep upwelling could provide a source of recycled subducted volatiles.

5.6. A world-wide process

The super-reduced mineral assemblages described here are not simply mineralogical curiosities; their terrestrial occurrence has a wider significance. Under current paradigms, the fO_2-*T* conditions required to produce SiC, silicide melts, Ti^{3+}-bearing phases and native vanadium would not be expected to occur in Earth's upper mantle. However, their presence at Mt Carmel shows that melts derived from the sublithospheric mantle may be accompanied by CH_4-H_2 fluids, and when concentrated in specific environments such fluids can produce highly reduced rocks. How widespread are these processes, and what is their role in the global carbon cycle?

As noted above, samples of a hibonite-grossite-V-spinel-V^0 assemblage with strong similarities to that in Mt Carmel have been reported from the Sierra de Comechingones, San Luis, Argentina (Cámara et al., 2019). The locality is not more closely specified, but the authors have suggested that it is derived from the Neogene Volcanic Belt of San Luis in Argentina.

Rappenglück (2022) has provided an exhaustive review of occurrences of natural iron silicides, and lists > 40 localities of Fe silicides associated with mantle-derived rocks. He includes information on many associated minerals, but relatively sparse data on the geological evidence for their natural origin.

Heavy-mineral concentrates of chromitites in ophiolites from Tibet (Xu et al., 2015), the Polar Urals (Yang et al., 2014) Bulgaria (Xiong et al., 2017) and other ophiolites along major continental-collision zones contain SiC, diamond, Fe-Ti -Si alloys, native metals and other phases indicative of low fO_2 (Supplementary Material, Table S-25). Many of these phases also occur as inclusions in corundum together with tistarite, carmeltazite, TiN, TiC and native V (Xu et al., 2009, 2015), as in the Mt Carmel material. Spherules of wüstite and Fe^0 are also common. Because most of the reported minerals have been separated from very large rock samples by industrial-scale processes, there has been controversy surrounding these occurrences. However, Zhang et al. (2016) have demonstrated that the SUR phases occur *in situ* in both chromitites and in their peridotitic host rocks; key examples are SiC inclusions in highly magnesian olivine (Fo_{96-98}), SiC + wüstite + Fe^0 in olivine, and Fe^0 + Si^0 in chromite. Industrial contamination is therefore very unlikely.

The ophiolitic diamonds, now reported from numerous localities, have attracted particular opprobrium, and a campaign insisting that the diamonds are man-made (Litasov et al., 2019a,b,c,d; 2020a,b), because of their similarity in morphology and carbon-isotope composition to HPHT synthetic diamonds. This campaign appears to imply either improper behaviour from researchers, or widespread contamination with synthetic diamonds from drill bits, polishing wheels or similar industrial equipment. At least in the case of Luobusa both accusations seem improbable, because diamonds were first found in Luobusa in the 1970s (Fang and Bai, 1981) at a time when synthetic HPHT diamonds apparently were not widely available in China.

More directly, Yang et al. (2014, 2015) and Zhang et al. (2016) have demonstrated that diamonds (and SiC) occur *in situ* in both chromite and olivine from the Ray-Iz (Polar Urals) and Luobusa chromitites; in each case the diamonds and SiC are surrounded by microbreccias filled with amorphous carbon. Furthermore, Xu et al. (2017) and Moe et al. (2017) have shown that the ophiolitic

diamonds have a suite of fluid inclusions containing REE, carbonate and minerals (chromite, moissanite) that are not found in any known synthetic diamonds. They also note that the diamonds from both chromitites and peridotites at Luobusa display a much wider range of $\delta^{13}C$ (−15 to −29 ‰; Howell et al., 2015; Xu et al., 2017) than HPHT diamonds, which are typically homogeneous around $\delta^{13}C$ = −21 ‰. Both Howell et al. (2015) and Xu et al. (2017) observe that the ophiolitic diamonds contain high levels of trace elements (not found in synthetic diamonds) and inclusions of Ni-Mn-Co alloys rather than the Fe-Ni alloys common in HPHT diamonds. The trace-element patterns of Luobusa diamonds are broadly similar to those of kimberlitic diamonds (Howell et al., 2015), but differ in having strong negative anomalies in redox-sensitive elements such as Eu, Sm, Yb and Y, and containing essentially no Fe; these features link the diamonds to the SUR assemblages. Moe et al. (2017) have used spectroscopic techniques to identify fluid inclusions of carbonate and silicate fluid, solid inclusions of CO_2, and reduced mineral inclusions (moissanite and Mg-chromite) in diamonds from both Luobusa and Ray-Iz. There is thus no reasonable basis to regard the diamonds in the Tethyan and Urals ophiolites as being man-made, nor that they are part of a natural SUR mineral association. Other occurrences can be expected when similar bodies in continental-collision zones are subjected to similarly meticulous examination.

There is evidence that the Tibetan ophiolites experienced a subduction episode that carried the peridotites and chromitites from a near-surface environment to the Mantle Transition Zone (MTZ). Yang et al. (2007) and Dobrzhinetskaya et al. (2009) described an association of diamond, a high-*P* form of TiO_2 and coesite pseudomorphs after stishovite, all included in chromite. McGowan et al. (2015) and Griffin et al., (2016b) described exsolved pyroxenes and coesite in chromite, suggesting inversion from a high-P Ca-ferrite polymorph of chromite. Microstructural evidence indicates that the chromitites recrystallized from fine-grained highly deformed mixtures and an octahedral polymorph of chromite (Satsukawa et al., 2015). An inverse-ringwoodite phase found in concentrates from Luobusa was later synthesised at 20 GPa and 1600 °C (Bindi et al., 2018). Symplectites of opx + Cr-Al spinel ± cpx in the peridotites are related to the breakdown of majoritic garnet. Geodynamic modelling (Griffin et al., 2016b) suggests that the exhumation of the peridotites from the MTZ was initiated by slab rollback and took <10 m.y., consistent with the low aggregation state of N in the diamonds (Howell et al., 2015, Xu et al., 2017).

It seems very probable that deeply subducted peridotites in major suture zones would have interacted with highly reduced fluids both in the deep upper mantle or the MTZ, and on their way back to the surface. This reaction is consistent with the many similarities between the mineral associations in Mt Carmel and those in Luobusa, Ray-Iz and many other ophiolites in similar tectonic settings (Supplementary Material, Table S-25). Aside from the absence of diamond in Mt Carmel, the major difference lies in the abundance of PGE-Fe-Mn-Cr alloys and native elements in the ophiolitic assemblages. This clearly reflects a difference in starting points for the reduction processes: mafic-felsic melts at Mt Carmel *vs* peridotites and chromitites in the ophiolitic rocks.

The occurrence of diamond + SiC + CH_4 + CO_2 inclusions in garnet from Alpine UHP metasedimentary rocks (e.g., Janák et al., 2015) indicates that highly reducing conditions also may exist in the crustal section of subducting slabs that reach UHP conditions. The reducing fluids in these situations may be derived from carbonaceous-pelitic sediments within the downgoing crustal section. However, the similarity in tectonic setting to the Tethyan ophiolites suggests that such deep-seated mantle structures may serve as conduits for CH_4 + H_2 fluids derived from the deeper mantle and released by the mantle upwellings that accompany subduction activity on such structures.

Xenocrysts in subduction-related explosive mafic–ultramafic volcanics on the Kamchatka peninsula include diamond, Ti-corundum, SiC, Fe-Ti-Cr alloys, Fe-Si alloys and native Fe; the largest suite has come from the 2012–2013 eruption of the Tolbachik Fissure (Karpov et al., 2014; Galimov et al., 2020; Supplementary Material, Table S-25). The diamonds have been found both in cavities in basalts, and in pyroclastic eruption products sampled while still warm. The authors have provided extensive evidence for the natural occurrence of the diamonds, including high concentrations of volatile elements (F, Cl, S) that also are abundant in the gasses from the eruptions, and inclusions of both SiC and Mn-silicides that are not found in HPHT diamonds. At least six other Kamchatka volcanoes have provided similar material, while aggregates of polycrystalline diamond cemented with tilleyite ($Ca_5(Si_2O_7)(CO_3)_2$), SiC, Fe-Ni-Mn-Cr silicides, graphite and Si^0 ("kamchatkites"; Kaminsky et al., 2019) have been reported from the Valizhgen Peninsula. The authors proposed that this assemblage was formed by gas-phase condensation or chemical vapor deposition; the implication is that the volcanic gasses in this case must have been extremely reducing.

Kamchatka provides other importance evidence for reduced mantle-derived fluids (Table S-24). Spinel-harzburgite xenoliths from the Avacha volcano, representing fragments of the sub-arc upper mantle, contain a metasomatic mineral assemblage with native metals (Ni, Ti, Fe) and silicides (Fe_3Si, Fe_5Si_3, FeSi, $FeSi_2$, Fe-Ti-Si), many distributed in inclusion trails through olivine (Fo_{89-96}) and opx (Ishimaru et al., 2009). Composite inclusions suggest that a complex Fe-Ti-Si melt precipitated FeSiTi (toledoite; phase τ_2 of Weitzer et al., 2008), leaving residual melts that crystallized FeSi and other Fe-Ti-Si phases on cooling; similar relationships have been observed in the Mt Carmel corundum aggregates (Griffin et al., 2022). These assemblages require very low fO_2, while the host peridotites record high fO_2 (ΔQFM = +1 to + 2) related to earlier Si-rich metasomatism. These observations are critical to the interpretation of similar SUR assemblages in the Tethyan ophiolites, because the reduced fluids apparently have traversed the mantle wedge without achieving equilibrium with the enclosing rocks, and the assemblages precipitated by the fluids are consistent with the very low fO_2 of the volcanic gasses at the surface (Galimov et al., 2020). In these cases of obvious disequilibrium. the argument that such assemblages "cannot exist in the mantle" (e.g. Ballhaus et al., 2021) is clearly invalid.

Ishimaru et al. (2009) suggest that H_2 was derived from serpentinization in the underlying slab, which is plausible but perhaps not necessary. Modelling by J.C. Afonso (Griffin et al., 2016b) shows that slab rollback leads to the rapid exhumation of deep-mantle material, offering another source of CH_4-H_2 fluids. In either case, the examples from Kamchatka emphasise the similarity of products that can be produced by mantle-derived reduced fluids accompanying volcanism.

Kimberlites and related rocks also carry SUR mineral assemblages similar to those found at Mt Carmel (Table S-25). Yatsenko et al. (2017, 2018, 2021a,b) have documented a widespread "Highly Reduced Mantle Mineral Association" (HRMMA) including spherules of Fe-FeO melts (and related silicate glasses), metallic alloys, SiC, diamond, WC and Ti-rich corundum with inclusions of TiN, TiC, TiS, Fe-Ti-Si alloys, tistarite, grossmanite, carmeltazite and hibonite. They have described this association from numerous localities, including pyroclastic kimberlites and lamproites in the Azov and other blocks of the Ukrainian shield. We have independently verified their observations on the Azov kimberlites, using concentrates kindly provided by the late V.I. Tatarintsev (Tatarintsev et al., 1987; authors' unpublished data). The

HRMMA also is reported from Ukrainian lamproites (Yatsenko et al., 2020), diamondiferous pyroclastic "visherites" in the western Urals (Chaikovskii and Korotchenkova, 2012; Yatsenko et al., 2018), the Karpinska-1 kimberlite of the Arkhangelsk region (Yatsenko et al., 2021b), and several kimberlites in the Yakutian kimberlite fields (Yatsenko et al., 2017, 2018). Shiryaev et al. (2011) reported that SiC is common in Yakutian kimberlites, in grain sizes much larger than any used in synthetic abrasives. We also have observed that Ti-rich corundum from the Udachnaya East kimberlite carries inclusions of FeTiSi, TiC, carmeltazite, $TiFe_2Si_2$, Ti_2FeSi, Ti_3O_4 and Fe-carbide (authors' unpublished data).

Unfortunately, heavy-mineral concentrates from South African kimberlites have not been routinely examined for phases such as SiC and Ti-rich corundum, although Leung et al. (1996) described SiC microcrystals from a kimberlite in the Kimberley field. However, corundum with the bright pink CL characteristic of Ti^{3+} substitution in Mt Carmel corundum has been observed in microdiamond residues from the Svartruggens kimberlite (M. MacCallum, *oral pers. comm.*). The archives of microdiamond residues retained by diamond exploration companies thus are a potential resource for evaluating the presence of SUR phases in kimberlites.

The association of the HRMMA with kimberlites extends to its occurrence as inclusions in diamonds. A corundum inclusion with 1.8 wt% Ti was found in a diamond from the Monastery Mine kimberlite (South Africa; Moore and Gurney, 1989), and other diamonds from this mine contain inclusions of SiC. Otter and Gurney (1989) reported corundum inclusions with 0.7 and 1.2 wt % Ti in two diamonds from the Sloan kimberlite (Colorado). Native iron (Fe^0) has been found in diamonds from kimberlites in Yakutia (Sobolev, 1981), Sloan (Meyer and McCallum, 1986) and Rio Soriso (Brazil; Hayman et al., 2005), while Stachel et al. (1998) described a spherical inclusion of Fe^0 rimmed by wüstite (cf. Fig. 8a, b) in a diamond from the Mwadui kimberlite (Tanzania). Bulanova et al. (1998) found that many Yakutian diamonds contain a central "seed" of wüstite, suggesting the involvement of Fe-oxide melts in diamond formation.

SiC has also been recognized as inclusions in diamonds from Siberia (Marshintsev, 1990), the North China Craton (Fuxian kimberlite; Leung, 1990), the Argyle lamproite in Australia (Jaques et al., 1986, 1989), Sloan (Otter and Gurney, 1989) and Monastery Mine (Moore and Gurney, 1989). It therefore seems likely that these diamonds have formed by deposition of carbon released during the oxidation of methane, while in at least some cases Ti-corundum was crystallizing from coexisting reduced melts, as at Mt Carmel. The mineralogical links between Mt Carmel and the HRMMA in kimberlites and diamonds appear to support a critical role for methane-melt interactions in both the deep lithosphere and areas with thin SCLM.

The role of methane in diamond formation has been extensively debated. Stachel and Harris (2009) concluded that diamonds may have formed by both oxidation of methane and reduction of carbonates, with the former path dominant in Hadean to Archean time. Others (e.g., Jablon and Navon, 2016) have argued against the generation of diamonds from methane. However, fluid inclusions of methane have been described in diamonds from the Marange deposit in Zimbabwe (Smith et al., 2016), and from alluvial deposits in Siberia (Tomilenko et al., 1997). Other arguments for the growth of diamonds from methane-rich fluids have been based on the covariance of $\delta^{13}C$-N in single diamonds (Smit et al., 2016) and in a suite of cogenetic diamonds (Thomassot et al., 2007). The latter study of 59 diamonds in a small xenolith found correlations of [N], $\delta^{13}C$ and $\delta^{15}N$ that could best be explained by crystallization from a methane-bearing fluid undergoing Rayleigh fractionation (oxidation) under mantle conditions (150 km depth, 1200 °C).

A potential problem with such modelling is that reduced fluids from the asthenosphere will contain not only methane, but a rich variety of heavier hydrocarbons (O'Reilly et al., 1990; Sverjensky et al., 2017), and partition coefficients for CH_4/diamond may not describe the full natural situation. In such fluids, a decrease in *P* and *T* can produce changes in *pH* that can precipitate diamond or graphite independently of redox processes (Sverjensky et al., 2014; Sokol et al., 2017). Stachel et al. (2017) modelled the variations in $\delta^{13}C$ of diamonds and concluded that fluid speciation, rather than silicate-buffered redox reactions, is the key factor controlling $\delta^{13}C$. Stressing the rarity of $\delta^{13}C$-depletion trends, they concluded that most diamonds have crystallized from CH_4- and CO_2-bearing water-rich fluids. Perhaps more importantly, they conclude that these fluids must have a narrow low range of X_{CO2}, which would imply a nearly constant (buffered) initial fO_2 for the fluid source, presumably the asthenospheric mantle.

In these examples the mineral associations, and in particular the link between Ti-rich corundum and the super-reduced phases, are similar to those reported from Mt Carmel. We conclude that this association reflects a fundamental process – the transfer of highly reduced fluids from the mantle to the lithosphere -- that occurs across a range of tectonic settings, including cratonic roots, intraplate areas with thin lithosphere, volcanic arcs and continental-collision zones. The ubiquity of this process is strong evidence that the sublithospheric upper mantle is metal-saturated, so that fluids derived from this source will be dominated by $CH_4 + H_2$.

6. Conclusions

The Mt Carmel megacryst suite, combined with seismic and geochronological data, suggests that broadly syenitic melts evolved within a thick basaltic underplate built up from Permian to Miocene-Pliocene time, fluxed by highly reducing mantle-derived fluids. Our observations indicate that these melts were reduced to fO_2 near the IW buffer, leading to the separation of immiscible Fe^0- and Fe-Ti-oxide melts, coexisting with more felsic melts and a C-O–H fluid phase. The microstructural similarity between these products and experimental systems with multiple immiscibility (Meredith et al., 2020) suggests a promising new direction for investigations of differentiation in mafic systems under reducing conditions.

With further reduction the felsic melts separated into immiscible Si-Al-Na,K oxide melts and Fe-rich, Si-poor oxide melts, as observed in other basaltic magma chambers. In a model magma/crystal-mush chamber, the FeO-rich melts, enriched in Ca, Mg, HFSE and REE + Zr sank, leaving the Si-Al-Na-K melts in an upper zone.

At fO_2 of ΔIW −6 to −7 further immiscibility produced Si-C and Fe-Ti-Si-C melts. Their gravitational removal led to (super)saturation in Al_2O_3 and crystallization of corundum (*Crn-B*) from the residual Ca-Al-Si oxide melt. Oxidation of CH_4 to CO_2 could produce carbonatitic melts that removed Ca, driving the residual melts to higher Si, as seen in the trapped melts in the corundum aggregates. The most reduced assemblages (hibonite + grossite + V^0) crystallized at *ca* ΔIW −9, from Ca-Al-silicate melts coexisting with H_2-dominated fluids, perhaps in pegmatitic segregations.

The evolution of the conjugate silicate melts in the upper parts of the model magma chamber is less well-defined; it may have crystallized the rare Cr-rich corundum (Griffin et al., 2021b) when fO_2 reached ΔIW −5, and *Crn-C* corundum at lower fO_2. The residual melts may be represented by the Ba-rich glasses coating many corundum-aggregate xenoliths. The *Crn-A* paragenesis reflects rapid crystallization of corundum in an open system, probably in fluid-escape channels opened during overturn of the magma

chamber as the deeper melts became less dense. Explosive basaltic eruptions from at least late Cretaceous to Miocene-Pliocene (-Pleistocene?) time appear to have sampled many versions of the model system described here, reflecting individual magma chambers at different depths, with different fluid mixtures, initial compositions and fluid dynamics, to produce the remarkable mineralogical diversity of Mt Carmel.

Such localized highly reduced volumes may commonly develop in the lithospheric mantle, regardless of its thickness, through the introduction of mantle-derived, magma-transported CH_4-H_2 fluids. The occurrence of the HRMMA suite in kimberlites and diamond inclusions implies that similar processes occur in the roots of cratons. The idea that "these phases cannot exist in the mantle" (e.g., Ballhaus et al., 2021) is invalid simply because it assumes that the reduced phases must equilibrate with more oxidized mantle peridotites and pyroxenites. The Mt Carmel example, and the many ophiolitic examples, show that reduced systems and their products can be protected from oxidation by entrapment in phases like corundum or chromite, by crystallization from H_2-saturated melts, or by isolation in pockets of amorphous carbon, as in the case of diamonds and SiC in ophiolitic chromitites (Howell et al., 2015; Griffin et al., 2016b). The example of the Avacha xenoliths discussed above demonstrates that reduced fluids can traverse mantle peridotites even on very small scales and deposit super-reduced phases, without equilibrating with the oxidised lithospheric mantle.

The interaction of such reduced fluids with the lithospheric mantle may be one control on lithosphere viscosity and stability (Jackson and Gibson,2023). The oxidation of such fluids also may be the ultimate source of the more commonly recognized metasomatic fluids dominated by CO_2 + H_2O. These observations suggest that more attention should be paid to the role of methane and other reduced fluids in mantle petrology, and their relevance to metasomatic processes, the genesis of diamonds, and the transport of elements that may form crustal mineral deposits. Global carbon cycles must include CH_4 as a major factor in mantle outgassing, especially during magmatism. There is a great deal to be learned about these processes from a careful examination of heavy-mineral concentrates and mantle-derived xenoliths in explosive volcanic rocks, from kimberlites to volcanic arcs and intraplate basalts.

Declaration of Competing Interest

The authors declare the following financial interests/personal relationships which may be considered as potential competing interests: Author Vered Toledo is no longer employed by Shefa Gems, and has no financial, personal or other connection with the company. She therefore declares no competing interests. All other authors declare that they have no competing interests.

Acknowledgements

We are very grateful to: John Ward for education on alluvial systems, including insightful guidance in the field; Reli Wald for education on the geological and geophysical history of the region; Eitan Sass for discussions on the geology of Mt Carmel; Hongkun Dai for education on basalt chemistry; Norm Pearson for his innovative and dedicated leadership of the laboratories of the Geochemical Analysis Unit; Yi-Jen Lai for assistance in the lab; Manal Bebbington for many, many sample preparations; Mike DeWit and Dave Apter for discussions on the Mt Carmel volcanism; Paul Asimow and Dan Harlow for insightful comments on several previous papers.

Prof. H. He (IGG-CAS, Beijing) contributed noble-gas analyses, Vlad Malkovets some kimberlite concentrates, Dima Kamenetsky the initial FE-SEM imaging, Ananuer Halumalati the analyses of trapped gasses and Anita Andrew the C-isotope analyses of carbonates. Sally-Ann Hodgekiss and Montgarri Castillo-Oliver patiently and calmly brought order from chaos to make the final graphics for the "crazily long paper". We especially thank Dr. M. Santosh for his encouragement and editorial handling, and Tim Horscroft for the invitation to present this review.

The research was funded in part by MIUR-PRIN2017, project "TEOREM: Deciphering geological processes using Terrestrial and Extraterrestrial ORE Minerals", prot. 2017AK8C32 (PI: Luca Bindi). Fernando Cámara gratefully acknowledges funding from the Italian Ministry of University and Research (MIUR) through the project "Dipartimenti di Eccellenza 2023–2027". SEM, EBSD and EPMA analyses were carried out at the Caltech GPS Division Analytical Facility, which is supported, in part, by NSF Grants EAR-0318518 and DMR-0080065. The authors acknowledge the facilities and the scientific and technical assistance of Microscopy Australia at the Centre for Microscopy, Characterisation & Analysis, The University of Western Australia, a facility funded by the University, State and Commonwealth Governments. This study also used instrumentation funded by ARC LIEF and DEST 567 Systemic Infrastructure Grants, Macquarie University and industry. This is contribution 1761 from the ARC Centre of Excellence for Core to Crust Fluid Systems (www.ccfs.mq.edu.au) and 1530 from the GEMOC Key Centre (www.gemoc.mq.edu.au).

Funding Sources

This research did not receive any specific grant from funding agencies in the public, commercial or not-for-profit sectors. Shefa Gems Ltd. provided resources required for field work, conference presentations and laboratory visits by WLG, SYOR, SEMG and JXH.

Appendix A. Supplementary data

Supplementary data to this article can be found online at https://doi.org/10.1016/j.gr.2023.10.013.

References

Agata, T., 1998. Geochemistry of ilmenite from the Asama ultramafic-mafic layered igneous complex, Mikabu greenstone belt, Sambagawa metamorphic terrane, central Japan. Geochem. Jour. 32, 231–241.
Anovitz, L.M., Essene, E., 1987. Phase equilibria in the system $CaCO_3$-$MgCO_3$-$FeCO_3$. Jour. Petrology 28, 389–415.
Apter, D.B., 2014. High pressure indicator minerals from the Rakefet magmatic complex (RMC). Mt. Carmel, Israel. Kimberley Diamond Symposium, Kimberley, South Africa.
Ardit, M., Cámara, F., Hålenius, U., 2021. Vanadium-induced coloration in grossite (CaAl4O7) and hibonite (CaAl12O19). Amer. Mineral. 106, 599–608.
Bali, E., Audetat, A., Keppler, H., 2013. Water and hydrogen are immiscible in Earth's mantle. Nature 495, 220–222.
Ballhaus, C. et al., 2021. Ultra-reduced phases in ophiolites cannot come from the Earth's mantle. Amer. Mineral. 106, 1053–1063.
Barnes, S.J., Roedder, P.L., 2001. The range of spinel compositions in terrestrial mafic and ultramafic rocks. Jour. of Petrology 42, 2279–2302.
Barr, S., Dostal, J., 1986. Petrochemistry and origin of megacrysts in Upper Cenozoic basalts, Thailand. Journal of SE Asian Earth Sci. 1, 107–116.
Beckett, J.R. et al., 1988. Ti3+ in meteoritic and synthetic hibonite. Geochim. Cosmochim. Acta 52, 1479–1495.
Beckett, J., Stolper, E., 1994. The stability of hibonite, melilite and other aluminous phases in silicate melts: Implications for the origin of hibonite-bearing inclusions from carbonaceous chondrites. Meteoritics 29 (1), 41–65.
Belmonte, D., Ottonello, G., Zuccolini, M.V., Attene, M., 2017. The system MgO-Al2O3-SiO2 system under pressure: a computational study of melting relations and phase diagrams. Chem. Geol. 461, 54–64.

Belousova, E., Griffin, W.L., O'Reilly, S.Y., Fisher, N., 2002. Igneous zircon: trace element composition as an indicator of source rock type. Contrib. Mineral. Petrol. 143, 602–622.
Bergermann, A., French, M., Redmer, R., 2021. Gibbs-ensemble monte carlo simulation of H2–H2) mixtures. Phys. Chem. Chem. Phys. 23, 12637–12643.
Bindi, L. et al., 2018. Synthesis of inverse ringwoodite sheds light on the subduction history of Tibetan ophiolites. Sci. Repts 8, 5457.
Bird, J.M., Goodrich, C.A., Weathers, M.S., 1981. Petrogenesis of Uivfaq iron, Disko Island, Greenland. Journal of Geophys. Res.: Solid. Earth 86, 11787–11805.
Bulanova, G., Griffin, W., Ryan, C., 1998. Nucleation environment of diamonds from Yakutian kimberlites. Min. Mag. 62, 409–419.
Cámara, F., Bindi, L., Pagano, A., Pagano, R., Gain, S.E.M., Griffin, W.L., 2019. Dellagiustaite: a novel natural spinel containing V^{2+}. Minerals 9, 4–20.
Chaikovskii, I.I., Korotchenkova, O.V., 2012. Explosive mineral phases of diamondiferous pyroclastites of Western Urals. Lithosphere 2, 125–140. in Russian.
Charlier, B., Namur, O., Grove, T.L., 2013. Compositional and kinetic controls on liquid immiscibility in ferrobasalt–rhyolite volcanic and plutonic series. Geochim. Cosmochim. Acta 113, 79–93.
Christy, A.G., 1989. The stability of sapphiring+clinopyroxene: implications for phase relations in the CaO-MgO-Al2O3-SiO2 system under deep-crustal and upper mantle conditions. Contrib. Mineral. Petrol. 102, 422–428.
Clark, N.L., Chuang, S.Y., Mauro, J.C., 2022. Microstructural evolution of droplet phase separation in calcium aluminosilicate glasses. Jour. Amer. Ceram. Soc. 105, 193–206.
Darken, L.S., Gurry, R.W., 1946. The system Iron-Oxygen. II. Equilibrium and thermodynamics of liquid oxide and other phases. Jour. Amer. Chem. Soc. 68, 798–816.
Davis, A., Clague, D., Paduan, J., 2007. Diverse origins of xenoliths from seamounts at the continental margin, offshore central California. Jour. Petrology 48, 829–852.
Dobrzhinetskaya, L.F. et al., 2009. High-pressure highly reduced nitrides and oxides from chromitite of a Tibetan ophiolite. Proc. Nat. Acad. Sci. 106, 19233–19238.
Dvorkin, A., Kohn, B., 1989. The Asher Volcanics, northern Israel: petrography, mineralogy, and alteration. Israel Jour. Earth Sci. 38, 105–123.
Edmonds, M., Wallace, P., 2017. Volatiles and exsolved vapor in volcanic systems. Elements 13, 29–34.
Ellis, D., 1976. High pressure cognate inclusions in the Newer Volcanics of Victoria. Contrib. Mineral. Petrol. 58, 149–180.
Fang, Q., Bai, W.-J., 1981. The discovery of Alpine-type diamond-bearing ultrabasic intrusions in Tibet. Geol. Rev. 22, 455–477.
Fischer, L.A. et al., 2016. Immiscible iron-and silica-rich liquids in the Upper Zone of the Bushveld Complex. Earth Plan. Si. Lett. 443, 108–117.
Fourie, D.J., J, E.J., Zietsman, J.H., 2005. Calculation of FeO-TiO_2-Ti_2O_3 liquidus isotherms pertaining to high titania slags. Jour. s. African Inst. Mining Metal. 105, 695–710.
Friel, J.J., Harker, R.I., Ulmer, G.C., 1977. Armalcolite stability as a function of pressure and oxygen fugacity. Geochim. Cosmochim. Acta 41, 403–410.
Frost, D.J. et al., 2004. Experimental evidence for the existence of iron-rich metal in the Earth's lower mantle. Nature 428, 409.
Frost, D.J., McCammon, C.A., 2008. The Redox State of Earth's Mantle. Annu. Rev. Earth Planet. Sci. 36, 389–420.
Fukai, Y., 2006. The metal-hydrogen system: basic bulk properties. Springer Series. Mater. Sci. 21, 497 pp.
Galimov, E.M. et al., 2020. Enigmatic diamonds from the Tolbachik volcano. Kamchatka. Amer. Mineral. 105, 498–509.
Galuskin, E., Galuskina, I., 2023a. Evidence of the antoropogenic origin of the "Carmel Sapphire" with enigmatic super-reduced minerals. Min. Mag. 87, 619–630.
Galuskin, E., Galuskina, I., 2023b. Reply to the discussion of "Evidence of the anthropogenic origin of the "Carmel sapphire" with enigmatic super-reduced minerals" by E. Galuskin and I. Galuskina (Mineralogical Magazine, 87, 631–634) by W.L. Griffin, V. Toledo and S.Y. O'reilly. Min. Mag. 87, 635–638.
Garfunkel, Z., 1989. Tectonic setting of phaneroozoic magmatism in Israel. Israel Jour. of Earth-Sci. 38, 51–74.
Giuliani, G. et al., 2007. Oxygen isotope systematics of gem corundum deposits in Madagascar: relevance for their geological origin. Mineral. Dep. 42, 251–270.
Giuliani, A. et al., 2022. Perturbation of the deep-Earth carbon cycle in response to the Cambrian Explosion. Sci. Advances 8, eabj1325.
Goldsmith, J.R., 1980. The melting and breakdown reactions of anorthite at high pressures and temperatures. Amer. Mineral. 65, 272–284.
Goldsmith, J.R., Heard, H.C., 1961. Subsolidus phase relations in the system $CaCO_3$-$MgCO_3$. Jour. Geol. 69, 45–74.
Graham, I.T. et al., 2019. Enigmatic alluvial sapphires from the Orosmayoretion, Jujuy Province northwest Argentina: Insights into their origin from in situ oxygen isotopes. Minerals 9, 390.
Griffin, W.L. et al., 2000. The Hf isotope composition of cratonic mantle: LAM-MC-ICPMS analysis of zircon megacrysts in kimberlites. Geochim. Cosmochim. Acta 64, 133–147.
Griffin, W.L. et al., 2016a. First terrestrial occurrence of tistarite (Ti2O3): Ultra-low oxygen fugacity in the upper mantle beneath Mount Carmel. Israel. Geology 44 (G37910), 1.
Griffin, W.L. et al., 2016b. Mantle recycling: Transition zone metamorphism of Tibetan ophiolitic peridotites and its tectonic implications. Jour. Petrol. 57, 655–684.
Griffin, W.L. et al., 2018a. Carmeltazite, $ZrAl_2Ti_4O_{11}$, a New Mineral Trapped in Corundum from Volcanic Rocks of Mt Carmel. Northern Israel. Minerals 8, 601.
Griffin, W.L. et al., 2018b. Permian to quaternary magmatism beneath the Mt Carmel area, Israel: Zircons from volcanic rocks and associated alluvial deposits. Lithos 314–315, 307–322.
Griffin, W.L. et al., 2018c. Super-reducing conditions in ancient and modern volcanic systems: sources and behaviour of carbon-rich fluids in the lithospheric mantle. Mineral. Petrol. 112, 101–114.
Griffin, W.L. et al., 2019a. A terrestrial magmatic hibonite-grossite-vanadium assemblage: Desilication and extreme reduction in a volcanic plumbing system, Mt Carmel. Israel. Amer. Mineral. 104, 207–219.
Griffin, W.L. et al., 2020a. Parageneses of TiB_2 in corundum xenoliths from Mt. Carmel, Israel: Siderophile behavior of boron under reducing conditions. Amer. Mineral. 105, 1609–1621.
Griffin, W.L. et al., 2020b. Extreme reduction: Mantle-derived oxide xenoliths from a hydrogen-rich environment. Lithos 358–359, 105404.
Griffin, W.L. et al., 2021a. Nitrogen under super-reducing conditions: Ti oxynitride melts in xenolithic corundum aggregates from Mt Carmel (N. Israel). Minerals 11, 780.
Griffin, W.L. et al., 2021b. Cr_2O_3 in corundum: Ultrahigh contents under reducing conditions. Amer. Mineral 106, 1420–1437.
Griffin, W.L. et al., 2022. Immiscible metallic melts in the upper mantle beneath Mount Carmel, Israel: Silicides, phosphides, and carbides. Amer. Mineral. 107, 532–549.
Griffin, W.L., Toledo, V., O'Reilly, S.Y., 2019b. Discussion of "Enigmatic super-reduced phases in corundum from natural rocks: Possible contamination from artificial abrasive materials or metallurgical slags" by Litasov et al. (Lithos, 340–341, p.181–190). Lithos, 348-349: 105122.
Griffin, W.L., O'Reilly, S.Y., 1987. Is the continental Moho the crust-mantle boundary? Geology 15, 241–244.
Guo, J., O'Reilly, S.Y., Griffin, W.L., 1996. Corundum from basaltic terrains: a mineral inclusion approach to the enigma. Contrib. Mineral. Petrol. 122, 368–386.
Gurlo, A. et al., 2008. Nanocubes or nanorhombohedra? Unusual crystal shapes of corundum-type indium oxide. Jour. Phys. Chem. C 112, 9209–9213.
Haggerty, S., 1976. Opaque mineral oxides in terrestrial igneous rocks. In Lindsley, ed., Oxide Minerals. MXSA Rev. Mineral. 25, 101–277.
Hatipoglu, M., Chamberlain, S.C., 2011. A gem diaspore occurrence near Pinarcik, Mugla, Turkey. Rocks Miner. 86, 242–249.
Hattingh, J., 2019. Updated competent person's report on the Shefa Gems Ltd gemstone assets. Internal Report, 114 pp. https://www.shefagems.com/geological-science-reports.
Hayman, P.C., Kopylova, M.G., Kaminsky, F.V., 2005. Lower mantle diamonds from Rio Soriso (Juina area, Mato Grosso, Brazil). Contrib. Mineral. Petrol. 149, 430–445.
Hofstetter, A., Bock, G., 2004. Shear-wave velocity structure of the Sinai subplate from receiver function analysis. Geophys. Jour. Internat. 158, 67–84.
Hofstetter, A., Dorbath, C., Rybakov, M., Goldshmidt, V., 2000. Crustal and upper mantle structure across the Dead Sea rift and Israel from teleseismic P-wave tomography and gravity data. Tectonophysics 327, 37–59.
Howell, D. et al., 2015. Diamonds in ophiolites: Contamination or a new diamond growth environment? Earth Plan. Sci. Lett. 430, 284–295.
Huang, J.-X. et al., 2020. Immiscible metallic melts in the deep Earth: clues from moissanite (SiC) in volcanic rocks. Sci. Bull. 65, 1479–1488.
Hurai, V. et al., 1998. Immiscible separation of metalliferous Fe/Ti-oxide melts from fractionating alkali basalt: P-T-f O_2 conditions and two-liquid elemental partitioning. Contrib. Mineral. Petrol. 133, 12–29.
Ilani, S., Karri, U., Harlavan, Y., 2005. Campanian volcanism within the Asher-1 borehole. Isr. J. Earth Sci 54, 179–181.
Ilatovskaia, M., Savinykh, G., Fabrichnaya, O., 2017. Thermodynamic description of the ZrO_2-TiO_2-Al_2O_3 system based on experimental data. Jour. Euro. Ceram. Soc. 37, 3461–3469.
Ishimaru, S., Arai, S., Shukuno, H., 2009. Metal-saturated peridotite in the mantle wedge inferred from metal-bearing peridotite xenoliths from Avacha volcano. Kamchatka. Earth Plan. Sci. Lett. 284, 352–360.
Jablon, B.M., Navon, O., 2016. Most diamonds were created equal. Earth Plan. Sci. Lett. 443, 41–47.
Jackson, C.G., Gibson, S.A., 2023. Build-up of multiple volatiles in Earth's continental keels: Implications for craton stability. Earth Plan. Sci. Lett. 611, 118134.
Jakobsen, J.K., Veksler, I.V., Tegner, C., Brooks, C.K., 2005. Immiscible iron- and silica-rich melts in basalt petrogenesis documented in the Skaergaard intrusion. Geology 33, 885–888.
Janák, M. et al., 2015. Diamond in metasedimentary crustal rocks from Pohorje, Eastern Alps: a window to deep continental subduction. Jour. Metam. Geol. 33 (5), 495–512.
Jaques, A.L., Lewis, J.D, Smith, C.B., 1986. The kimberlitic and lamproitic rocks of Western Australia. Geol. Surv. W. Aust. Bull. 132.
Jaques, A.L. et al., 1989. Composition of crystalline inclusions and C-isotopic composition of Argyle and Ellendale diamonds, in Ross, J. et al., eds Kimberlites and related rocks Volume 2, Their mantle/crust setting, diamonds and diamond exploration, Geol. Soc. Aust. Spec. Publ. 14, Ross, J. et al., eds: 966-989.
Jaupart, C., Brandeis, G., Allègre, C.J., 1984. Stagnant layers at the bottom of convecting magma chambers. Nature 308, 535–538.

Jung, I.-H., Decterov, S.A., Pelton, A.D., 2004. Critical thermodynamic evaluation and optimization of the MgO-Al_2O_3, CaO-MgO-Al_2O_3, and MgO-Al_2O_3-SiO_2 systems. Jour. Phase Equil. Diffus. 25, 329–345.
Kafri, U., 2002. Neogene to Early Quaternary drainage systems in the Lower Galilee, Israel and their relationship to young tectonics. Israel Jour. Earth Sci. 51, 50–65.
Kahlenberg, V., Fischer, R.X., Shaw, C.S.J., 2000. High-pressure $Ca_4Al_6O_{13}$: an example of a calcium aluminate with three different types of coordination polyhedra for aluminum. Amer. Mineral. 85, 1492–11196.
Kaminchik, J., Segev, A., Katzir, Y., 2014. The origin of intraplate alkaline mafic magmatism in continental shelves: lavas and xenoliths from the Upper Cretaceous volcanos of Mt Carmel. Beer Sheva University, Israel. Unpublished MSc thesis.
Kaminsky, F.V., Wirth, R., Anikin, L.P., Schreiber, A., 2019. "Kamchatite" diamond aggregate from northern Kamchatka, Russia: New find of diamond formed by gas phase condensation or chemical vapor deposition. Amer. Mineral. 104, 140–149.
Karpov, G. et al., 2014. Diamonds and accessory minerals in products of the 2012–2013 Tolbachik fissure eruption. Jour. Volc. Seism. 8, 323–339.
Kaviani, A., Sandvol, E., Moradi, A., Rümpker, G., Tang, Z., Mai, P.M., 2018. Mantle Transition Zone thickness beneath the Middle East: Evidence for segnented Tethyan slabs, delaminated lithosphere andLower Mantle upwelling. Jour. Geophys. Res. Solid Earth 123, 4886–4905.
Koulakov, I., Sobolev, S.V., 2006. Moho depth and three-dimensioinal P and S structure of the crust and jppermost mantle in the Eastern Mediterranean and Middle Ease derived from tomographic inversion of local ISC data. Geophys. Jour. Intern. 164, 218–235.
Larimer, J.L., 1968. An experimental investigation of oldhamite, CaS; and the petrologic significance of oldhamite in meteorites. Geochim. Cosmochim. Acta 32, 965–982.
Laws, E.D., Wilson, M., 1997. Tectonics and magmatism associated with Mesozoic passive continental margin development in the Middle East. Jour. Geol. Soc. 154, 459–464.
Leung, I., 1990. Silicon carbide cluster entrapped in a diamond from Fuxian. China. Amer. Mineral. 7, 1110–1119.
Leung, I., Taylor, G.L., Tsao, C., Han, Z., 1996. SiC in diamond and kimberlites: Implications for nucleation and growth of diamond. Inter. Geol. Rev. 38, 595–606.
Li, Y. et al., 2021. Seismic constraint from Vp/Vs ratios on the structure and composition across the continent-ocean transition zone, South China Sea. Geophys. Res. Lett. 48. e2021GL094656.
Litasov, K.D. et al., 2019c. Cuboctahedral type Ib diamonds in ophiolitic chromitites and peridotites: the evidence for anthropogenic contamination. High Pres. Res. 39, 480–488.
Litasov, K.D. et al., 2019d. Comparison of enigmatic diamonds from the Tolbachik arc volcano (Kamchatka) and Tibetan ophiolites: Assessing the role of contamination by synthetic materials. Gond. Res. 75, 16–27.
LItasov et al., 2020a. "Kamchatite" diamond aggregate from northern Kamchatka, Russia: New find of diamond formed by gas phase condensation or chemical vapor deposition—Discussion. Amer. Mineral. 105, 141–143.
Litasov, K.D., Bekker, T.B., Kagi, H., 2019a. Reply to the discussion of "Enigmatic super-reduced phases in corundum from natural rocks: Possible contamination from artificial abrasive materials or metallurgical slags" by Litasov et al. (Lithos, v.340–341, p.181–190) by W.L. Griffin, V. Toledo and S.Y. O'Reilly. Lithos, 348-349: 105170.
Litasov, K.D., Bekker, T.B., Kagi, H., Ohfuji, H., 2020b. Reply to the comment on "Comparison of enigmatic diamonds from the Tolbachik arc volcano (Kamchatka) and Tibetan ophiolites: Assessing the role of contamination by synthetic materials" by Litasov et al. (2019) (Gondwana Research, 75, 16–27) by Yang et al. Gond. Res., 79: 304–307.
Litasov, K.D., Kagi, H., Bekker, T.B., 2019b. Enigmatic super-reduced phases in corundum from natural rocks: Possible contamination from artificial abrasive materials or metallurgical slags. Lithos 340–341, 181–190.
Lorand, J.-P., Gregoire, M., 2010. Petrogenesis of Fe–Ti oxides in amphibole-rich veins from the Lherz orogenic peridotite (Northeastern Pyrénées, France). Contrib. Mineral. Petrol. 160, 99–113.
Loucks, R.R., Fiorentini, M.L., Henríquez, G.J., 2020. New magmatic oxybarometer using trace elements in zircon. Jour. Petrology 61, egaa034.
Lu, J.-G. et al., 2022. Structure and composition of the lithosphere beneath Mount Carmel. North Israel. Contrib. Mineral. Petrol. 177, 29.
Lustrino, M., Dallai, L., 2003. On the origin of EM-I end-member. Neues Jahrb. Mineral.-Abh, 85–100.
Luth, R., Stachel, T., 2014. The buffering capacity of lithospheric mantle: implications for diamond formation. Contrib. Mineral. Petrol. 168, 1–12.
Ma, C., Beckett, J.R., 2021. Kaitianite, Ti3+2Ti4+ O5, a new titanium oxide mineral from Allende. Meteor. Planet. Sci. 56, 96–107.
Ma, C., Cámara, F., Toledo, V., Bindi, L., 2023b. Griffinite, Al_2TiO_5: A new oxide mineral from inclusions in corundum xenocrysts from the Mount Carmel Area. Israel. Crystals 13, 1427.
Ma, C., Cámara, F., Bindi, L., Toledo, V., Griffin, W.L., 2024. New minerals from inclusions in corundum xenocrysts from the Mount Carmel Area, Israel: Magnéliite, ziroite, sassite, mizraite-(Ce) and yeite. Materials (in press).
Ma, C., Rossman, G.R., 2009. Grossmanite, CaTi3+AlSiO6, a new pyroxene from Allende meteorite. Amer. Mineral. 94, 1491–1494.
Ma, C., Cámara, F., Bindi, L., Toledo, V., Griffin, W.L., 2023a. First terrestrial occurrence of kaitianite (Ti3+2Ti4+O5) from the upper mantle beneath Mount Carmel. Israel. Minerals 13, 1097.
Maas, R. et al., 2005. Sr, Nd, and Pb isotope evidence for a mantle origin of alkali chlorides and carbonates in the Udachnaya kimberlite, Siberia. Geology 33, 549–552.
Macris, C.A. et al., 2018. Evaporation induced isotope fractionation in tektites: an experimental study. GSA Annual Meeting 2018, 139–1119.
Macris, C.A., Young, E.D., Kohl, I.E., zur Loye, T.E., 2017. Evaporation induced oxygen isotope fractionation in impact ejecta, AGU Fall Meeting Abstracts, pp. V14B-01.
Mao, H., Hillert, M., Selleby, M., Sundman, B., 2006. Thermodynamic assessment of the CaO–Al2O3–SiO2 System. Jour. Amer. Ceram. Soc. 89, 298–308.
Matjuschkin, V., Woodland, A.B., Frost, D.J., Yaxley, G.M., 2020. Reduced methane-bearing fluids as a source for diamond. Sci. Repts. 10, 6961.
Matmon, A., Wdowinski, S., Hall, J., 2003. Morphological and structural relations in the Galilee extensional domain, northern Israel. Tectonophysics 371, 223–241.
Matveev, S. et al., 1997. Volatiles in the Earth's mantle: I. Synthesis of CHO fluids at 1273 K and 2.4 GPa. Geochim. Cosmochim. Acta 61, 3081–3088.
McBirney, A.R., 1996. The Skaergaard Intrusion. In R.G. Cawthorn. Layered Intrusions. Develop. Petrol. 15, 147–180.
McBirney, A.R., Nakamura, Y., 1974. Immiscibility in late-stage magmas of the Skaergaard intrusion. Carnegie Inst. Wash. Yearbk 73, 348–352.
McGowan, N.M. et al., 2015. Tibetan chromitites: Excavating the slab graveyard. Geology 43, 179–182.
Meredith, C.H. et al., 2020. Predator–prey interactions between droplets driven by non-reciprocal oil exchange. Nature Chem. 12, 1136–1142.
Meyer, H.O.A., McCallum, M.E., 1986. Mineral inclusions in diamonds from the Sloan kimberlites. Colorado. Jour. Geol. 94, 600–612.
Moe, K.S., Yang, J.-S., Johnson, P., Xu, X., Wang, W., 2017. Spectroscopic analysis of microdiamonds in ophiolitic chromitite and peridotite. Lithosphere 10, 133–141.
Moore, R., Gurney, J., 1989. Mineral inclusions in diamond from the Monastery kimberlite, South Africa, in Ross, J. et al., eds Kimberlites and related rocks Volume 2, Their mantle/crust setting, diamonds and diamond exploration, Geol. Soc. Australia Spec. Publ., 14: 1029-1041.
Mysen, B., 2018. Solution mechanisms of COHN fluids in melts to upper mantle temperature, pressure, and redox conditions. American Mineralogist: Jour. Earth Planet. Mat. 103, 1780–1788.
Nakamura-Messenger, K. et al., 2012. Wassonite: A new titanium monosulfide mineral in the Yamato 691 enstatite chondrite. Amer. Mineral. 97, 807–815.
Naslund, H.R., 1983. The effect of oxygen fugacity on liquid immiscibility in iron-bearing silicate melts. Amer. Jour. Sci. 283, 1034–1059.
Nazzareni, S. et al., 2019. Discovery of moissanite in a peralkaline syenite from the Azores Islands. Lithos 324–325, 68–73.
Oliveira, B. et al., 2021. Ti3+ in corundum traces crystal growth in a highly reduced magma. Sci. Repts 11, 2439.
O'Reilly, S.Y., Griffin, W.L., Segalstad, T.V. 1990. The nature and role of fluids in the upper mantle: Evidence in xenoliths from Victoria, *Australia. in:Herbert, H.K. and Ho, E.H.,eds, "Stable* Isotopes and Fluid Processes in Mineralisation", Geology Department and University Extension, Univ. W. Australia Publ.,23: 315-323.
O'Reilly, S.Y., Griffin, W.L., 1985. A xenolith-derived geotherm for southeastern Australia and its geophysical implications. Tectonophysics 111, 41–63.
O'Reilly, S.Y., Griffin, W.L., 2010. Rates of Magma Ascent: Constraints from mantle-derived xenoliths. In: Dosseto, A., Turner, S., van Orman, J. (Eds.), Timescales of Magmatic Processes: from Core to Atmosphere. Blackwell Publishing Ltd, pp. 116–124.
Otter, M., Gurney, J., 1989. Mineral inclusions in diamonds from the Sloan diatremes, Colorado-Wyoming State Line kimberlite district, North America, in Ross, J. et al., eds Kimberlites and related rocks Volume 2, Their mantle/crust setting, diamonds and diamond exploration, Geol. Soc. Australia Spec. Pub.,14: 1042-1053.
Ottonello, G. et al., 2013. Thermodynamic investigation of the CaO–Al_2O_3–SiO_2 system at high P and T through polymer chemistry and convex-hull techniques. Chem. Geol. 346, 81–92.
Pedersen, A.K., 1979. Basaltic glass with high-temperature equilibrated immiscible sulphide bodies with native iron from Disko, central West Greenland. Contrib. Mineral. Petrol. 69, 397–407.
Pedersen, A.K., 1981. Armalcolite-bearing Fe-Ti oxide assemblages in graphite-equilibrated salic volcanic rocks with native iron from Disko, central West Greenland. Contrib. Mineral. Petrol. 77, 307–324.
Peucat, J.-J. et al., 2007. Ga/Mg ratio as a new geochemical tool to differentiate magmatic from metamorphic blue sapphires. Lithos 98, 261–274.
Podlesskii, K.K., 2010. Stability of sapphirine-bearing mineral assemblages in the system FeO-MgO-Al2O3-SiO2 and metamorphic P-T parameters of aluminous granulites. Petrologty 18, 350–368.
Rappenglück, M.A., 2022. Natural Iron Silicides: A Systematic Review. Minerals 12, 188.
Rees, K. et al., 2018. Combining single source chemical vapour deposition precursors to explore the phase space of titanium oxynitride thin films. Dalton Trans. https://doi.org/10.1039/c7dt04694d.
Reutsky, V.N., Bordov, Y.M., Bataleva, Y.V., Palynov, Y.N., 2023. Carbon isotope fractionation during metal-carbonate interaction at the mantle pressures and temperatures. Russian Geol. Geophys. 64, 1–9.

Rohrbach, A. et al., 2007. Metal saturation in the upper mantle. Nature 449, 456.
Roup, A., Kalmanovitch, E., Baykov, Y., Toledo, V., 2009. Shefa Yamim moissanite discovery in Israel, Abstracts, Israel Geol. Soc. Meet., pp. 111.
Rozenbaum, A. et al., 2016. 40Ar/39Ar chronostratigraphy of late Miocene–early Pliocene continental aquatic basins in SE Galilee. Israel. Geol. Soc. Amer. Bull. 128, 1383–1402.
Sass, E., 1980. Late Cretaceous volcanism in Mount Carmel. Israel. Israel Jour. of Earth Sci. 29, 8–24.
Satsukawa, T., Griffin, W.L., Piazolo, S., O'Reilly, S.Y., 2015. Messengers from the deep: Fossil wadsleyite-chromite microstructures from the Mantle Transition Zone. Sci. Repts 5, 16484.
Segev, A., Rybakov, M., 2011. History of faulting and magmatism in the Galilee (Israel) and across the Levant continental margin inferred from potential field data. Jour. Geodyn. 51, 264–284.
Segev, A., 2005. Phanerozoic Magmatic Activity Associated with Vertical Motions in Israel and the Adjacent Countries. In: Hall, J.K. et al. (Eds.), Geological Framework of the Levant Vol II. The Levantine Basin and Israel, pp. 553-574.
Shiryaev, A.A., Griffin, W.L., Stoyanov, E., 2011. Moissanite (SiC) from kimberlites: Polytypes, trace elements, inclusions and speculations on origin. Lithos 122, 152–164.
Smit, K.V. et al., 2016. Diamond growth from C-H–N–O recycled fluids in the lithosphere: Evidence from CH4 micro-inclusions and δ13C–δ15N–N content in Marange mixed-habit diamonds. Lithos 265, 68–81.
Smith, E.M. et al., 2016. Large gem diamonds from metallic liquid in Earth's deep mantle. Science 354, 1403–1405.
Smith, E.M. et al., 2018. Blue boron-bearing diamonds from Earth's lower mantle. Nature 560, 84–87.
Sobolev, N., 1981. Native iron in Yakutian diamonds, its paragenesis. Geol Geofiz 22, 25–29.
Sokol, A.G. et al., 2017. Stability of methane in reduced C-O–H fluid at 6.3 GPa and 1300–1400°C. Dokl. Earth Sci. 474, 680–683.
Song, Y., Hu, W., 2009. Carbonates and sulfates-bearing melt inclusions in corundum megacrysts from Changle basalts of Shandong province and their implications. Acta Petrol. Mineral. 28, 349–363.
Srithai, B., Rankin, A., 1999. Fluid inclusion characteristics of sapphires from Thailand, Mineral Deposits: Processes to Processing, SGA Meeting 1999 Proceedings. Balkema, Rotterdam, pp. 107–110.
Stachel, T., Harris, J.W., 2009. Formation of diamond in the Earth's mantle. Jour. Phys. Cond. Matt. 21, (36) 364206.
Stachel, T., Harris, J.W., Brey, G.P., 1998. Rare and unusual mineral inclusions in diamonds from Mwadui, Tanzania. Contrib. Mineral. Petrol. 132, 34–47.
Stachel, T., Chacko, T., Luth, R.W., 2017. Carbon isotope fractionation during diamond growth in depleted peridotite: Counterintuitive insights from modelling water-maximum CHO fluids as multi-component systems. Earth Plan. Sc. Lett. 473 (Supplement C), 44–51.
Stagno, V., Ojwang, D.O., McCammon, C.A., Frost, D.J., 2013. The oxidation state of the mantle and the extraction of carbon from Earth's interior. Nature 493, 84–88.
Stein, M., Goldstein, S.L., 1996. From plume head to continental lithosphere in the Arabian-Nubian shield. Nature 382, 773–778.
Stein, M., Hofmann, A.W., 1992. Fossil plume head beneath the Arabian lithosphere? Earth Plan. Sci. Lett. 114, 193–209.
Stein, M., Hofmann, A.W., 1994. Mantle plumes and episodic crustal growth. Nature 372, 63–68.
Steinberg, J., Gvirtzman, Z., Folkman, Y., 2010. New age constraints on the evolution of the Mt Carmel structure and its implications on a Late Miocene extensional phase of the Levant continental margin. Jour. Geol. Soc. 167, 203–216.
Sverjensky, D.A., Stagno, V., Huang, F., 2014. Important role for organic carbon in subduction-zone fluids in the deep carbon cycle. Nature Geosci. 7, 909–913.
Tarr, W.A., Lonsdale, J.T., 1929. Pseudo-cubic quartz crystals from Artesia, New Mexico. Amer. Mineral. 14, 50–53.
Tatarintsev, V., Sandomirskaya, S., Tsymbal, S., 1987. First find of titanium nitride (osbornite) in terrestrial rocks. Dokl. Akad. Nauk SSSR 296, 1458–1461.
Thomassot, E. et al., 2007. Methane-related diamond crystallization in the Earth's mantle: Stable isotope evidences from a single diamond-bearing xenolith. Earth Plan. Sci. Lett. 257, 362–371.
Tomilenko, A. et al., 1997. Volatile components in the upper mantle (from data on fluid inclusions). Russ. Geol. Geophys. 38, 294–303.
Turner, S., Wilde, S., Wörner, G., Schaefer, B., Lai, Y.-J., 2020. An andesitic source for Jack Hills zircon supports onset of plate tectonics in the Hadean. Nature Comm. 11, 1241.
Ulff-Møller, F., 1990. Formation of native iron in sediment-contaminated magma: I. A case study of the Hanekammen Complex on Disko Island. West Greenland. Geochim. Cosmochim. Acta 54, 57–70.
Ulmer, G. et al., 1998. The redox stability of moissanite (SiC) compared with metal-metal oxide buffers at 1773 K and at pressures up to 90 kbar. Neues Jahrb. Mineral. Abh. 172, 279–307.
VanTongeren, J., Mathez, E., 2012. Large-scale liquid immiscibility at the top of the Bushveld Complex, South Africa. Geology 40, 491–494.
Veizer, J., 1989. Strontium isotopes in seawater through time. Ann. Rev. Earth Plan. Sci. 17, 141–167.
Veksler, I.V. et al., 2006. Immiscible silicate liquid partition coefficients: implications for crystal-melt element partitioning and basalt petrogenesis. Contrib. Mineral. Petrol. 152, 685–702.
Vu, D.T.A., Fanka, A., Salam, A., Sutthirat, C., 2021. Variety of iron oxide inclusions in sapphire from southern Vietnam: Indication of environmental change during Crystallization. Minerals 11,:241.
Wald, R., Toledo, V., 2016. Volcanic host rocks as sources of corundum recovered from Shefa Yamim's multi-commodity alluvial placer, northern Israel. Abstract 2016 Annual Meeting Israel Geological Society.
Watson, E.B., 1976. Two-liquid partition coefficients: experimental data and geochemical implications. Contrib. Mineral. Petrol. 56, 119–134.
Weinstein, Y., 2000. Spatial and temporal geochemical variability in basin-related volcanism, northern Israel. Jour. African Earth Sc. 30 (4), 865–886.
Weinstein, Y., 2012. Transform faults as lithospheric boundaries, an example from the Dead Sea Transform. Jour. Geodyn. 54, 21–28.
Weinstein, Y., Navon, O., Altherr, R., M., s.,, 2006. The role of lithospheric mantle heterogeneity in the generation of Plio-Pleistocene alkali basaltic suites from NW Harrat Ash Shaam (Israel). Jour. Petrology 47, 1017–1050.
Weitzer, F., Schuster, J.C., Naka, M., Stein, F., Palm, M., 2008. On the reaction scheme and liquidus surface in the ternary system Fe–Si–Ti. Intermetallics 16, 273–282.
Woodhead, J. et al., 2017. Tracking continental-scale modification of the Earth's mantle using zircon megacrysts. Geochem. Persp. Lett. 4, 1–6.
Woodland, A.B., Koch, M., 2003. Variation in oxygen fugacity with depth in the upper mantle beneath the Kaapvaal craton. Southern Africa. Earth Plan. Sci. Lett. 214, 295–310.
Wriedt, H.A., 1991. The Fe-O (Iron-Oxygen) system. Jour. of Phase Equil. 12, 170–199.
Wyatt, B.A., Baumgartner, M., Anckar, E., Grutter, H., 2004. Compositional classification of "kimberlitic" and "non-kimberlitic" ilmenite. Lithos 77, 819–840.
Xiong, F. et al., 2022. Jingsuiite, TiB_2, a new mineral from the Cr-11 podiform chromitite orebody, Luobusa ophiolite, Tibet, China: Implications for recycling of boron. Amer. Mineral. 107, 43–53.
Xiong, Q., Griffin, W.L., Huang, J-X., Gain, S.E.M., Toledo, V., Pearson, N.J., O'Reilly, S. Y., 2017. Super-reduced mineral assemblages in "ophiolitic" chromitites and peridotites: The view from Mt Carmel. European Journal of Mineralogy 29, 557–570.
Xu, X. et al., 2009. Unusual mantle mineral group from chromitite orebody Cr-11 in Luobusa ophiolite of Yarlung-Zangbo suture zone. Tibet. Jou. Earth Sc. 20, 284–302.
Xu, X. et al., 2015. Origin of ultrahigh pressure and highly reduced minerals in podiform chromitites and associated mantle peridotites of the Luobusa ophiolite. Tibet. Gond. Res. 27, 686–700.
Xu, X. et al., 2017. Fourier transform infrared spectroscopy data and carbon isotope characteristics of the ophiolite-hosted diamonds from the Luobusa ophiolite, Tibet, and Ray-Iz ophiolite, Polar Urals. Lithosphere 10, 156–169.
Xu, X. et al., 2021. Immiscible-melt inclusions in corundum megacrysts: Microanalyses and geological implications. Amer. Mineral. 106, 559–569.
Yang, J.-S. et al., 2007. Diamond- and coesite-bearing chromitites from the Luobusa ophiolite. Tibet. Geology 35, 875–878.
Yang, J. et al., 2015. Diamonds, native elements and metal alloys from chromitites of the Ray-Iz ophiolite of the Polar Urals. Gond. Res. 27, 459–485.
Yang, J.-S., Robinson, P.T., Dilek, Y., 2014. Diamonds in ophiolites. Elements 10, 127–130.
Yasuda, A., Aoki, J., Sakuma, T., 1998. Nanoporecipitation in Al_2O_3-3mol% Ti_2O_3 due to oxidation. Ceram. Intern. 24, 483–487.
Yatsenko, I.G. et al., 2020. Composition of spherules and lower mantle minerals, isotopic and geochemical characteristics of zircon from volcaniclastic facies of the Mriya lamproite pipe. Jour. Mining Inst. 242, 150–159.
Yatsenko, I.G., Stupka, O.O., Bilyk, N.T., 2018. Highly reduced mantle mineral association in volcaniclastic rocks of explosive structures: Essential features and classification. IV Int. Scientific-Practical Conference "Theory and Practice of Modern Science", Part I, 143-146. Odessa, Ukraine.
Yatsenko, I.G., Tymoschuk, V., Bilyk, N.T., Poberezhskyy, A.V., 2017. Mantle-derived native metals in explosive formation of Ukraine: Genetic, economic and ecological aspects. XI Int. Scientific Conference "monitoring of Geological Processes and Ecological Condition of the Environment". Kyiv, Ukraine.
Yatsenko, I.G., Galankina, O.L., Marin, Y.B., Skublovb, S.G., 2021a. Corundum with Inclusions of Extremely Reduced Minerals from Explosive Rocks of the Ukrainian Shield. Dokl. Earth Sci. 500, 833–837.
Yatsenko, I.G. et al. 2021b. Super reduced mineral phases in corundum aggregates from kimberlite. The discovery of terrestrial grossmanite. Abstracts of Conference "Geological Science in Independent Ukraine": 354-356.
Yaxley, G.M. et al., 2012. An oxygen fugacity profile through the Siberian Craton — Fe K-edge XANES determinations of Fe3+/∑Fe in garnets in peridotite xenoliths from the Udachnaya East kimberlite. Lithos 140–141, 142–151.
Yudalevich, Z., 2007. Petrographic description of rock samples. Ben-Gurion University of the Negev. Internal Report,.
Zhang, R.Y. et al., 2016. Discovery of in situ super-reducing, ultrahigh-pressure phases in the Luobusa ophiolitic chromitites, Tibet: New insights into the deep upper mantle and mantle transition zone. Amer. Mineral. 101, 1285–1294.
Zolotarev, A.A. et al., 2019. Dmisteinbergite, $CaAl_2Si_2O_8$, a metastable polymorph of anorthite: Crystal-structure and Raman spectroscopic study of the holotype specimen. Minerals 9, 570–582.

W.L. (Bill) Griffin is an isotopic geochemist and petrologist with major interests in mantle petrology and mineralogy, evolution of the subcontinental lithosphere, fluid fluxes in Earth, and diamond exploration. He is Professor Emeritus at Macquarie University, Sydney.

Luca Bindi is Full Professor of Mineralogy and Crystallography and is the Head of the Department of Earth Sciences of the University of Florence, Italy. His research activity has been devoted to mantle mineralogy, aperiodic structures in natural phases, structural complexity in minerals and the description of new mineral species.

Fernando Cámara studied the crystal-chemistry of eclogitic minerals for his Ph.D. at University of Granada (Spain; 1995) using X-ray diffraction and transmission electron microscopy. These techniques still support his research interests, focused on phase transitions in minerals at variable *T* and *P*, and the description of new minerals. He has built his career in the Italian C.N.R. and the Universities of Turin and Milan, where he is full professor.

Chi Ma is a mineralogist at California Institute of Technology, with research interests in nanomineralogy and the discovery of new minerals representing extreme conditions of formation. He is the discoverer and lead investigator of 59 IMA-approved new minerals. The refractory mineral machiite ($Al_2Ti_3O_9$) from the solar nebula was named in his honour.

Sarah Gain is a mineralogist and analytical geochemist; she generated most of the geochemical data used in this project. After working in the University of Western Australia and the Geological Survey of Western Australia, she is now a mineralogist with Fortescue Metals Group, Perth, and has turned her focus to iron ores.

Martin Saunders is an electron microscopy specialist in the Western Australian node of Microscopy Australia at The University of Western Australia. A physicist with a PhD in electron diffraction theory, he has spent more than 30 years developing and applying electron microscopy to problems across materials science, engineering, geoscience, physics, chemistry and the biosciences, including the investigation of early life on Earth.

Olivier Alard obtained his PhD at Macquarie University (Australia, 2002). He is Associate Professor at the Research School of Earth Sciences (ANU, Canberra) and a Research Director at CNRS (Géosciences Montpellier, France). His research focuses on the geochemistry of terrestrial and extra-terrestrial mafic and ultramafic rocks. His development of *in situ* analytical techniques has led to key contributions to the geochemistry of siderophile and chalcophile elements. He is currently studying the impact of oxygen fugacity and volatiles on the speciation of chalcophile elements.

Jin-Xiang Huang was an academic mantle geochemist for a decade, focused on mantle metasomatism and redox processes in xenoliths and xenocrysts using both radiogenic and stable isotopes. She joined the mining industry in 2021 to do exploration, especially for economic gold deposits.

Jeremy Shaw is platform leader for X-ray CT imaging at UWA's Centre for Microscopy, Characterisation and Analysis. A marine biologist by training, his interests focus on the application of X-ray and electron microscope techniques to study structure and function in biominerals (teeth, bone, shell), and the application of microscopy to study biological, geological and synthetic materials.

Caleb Meredith received his Ph.D. in Materials Science and Engineering from Penn State University in 2022 working with Dr. Lauren Zarzar to study the non-equilibrium and active behaviours of complex liquids. Caleb is currently the CEO and co-founder of Chromatir Technologies developing distinctive structurally coloured materials with tunable iridescent appearances for anticounterfeiting, optical signalling and detection.

Vered Toledo has worked in the diamond and jewellery industry since the beginning of her career. She designed and led the 14-year exploration program that discovered the placer gem deposits in the terraces of the paleo-Kishon river, and the laboratories that separated the minerals involved in this research project. She continues to pursue other interests in gems and gemmology.

Suzanne (Sue) Y. O'Reilly AM, FAA is a pioneer in the integration of geophysical, geochemical, petrological, petrophysical and tectonic data to construct realistic models of lithospheric structure and evolution. She was Director of two national research centres for over 25 years, while personally mentoring more than 100 postgraduate students and early-career researchers and enjoying fruitful collaborations with many wonderful colleagues worldwide. She is Professor Emerita at Macquarie University.